MINISTÉRIO DA CIÊNCIA, TECNOLOGIA, INOVAÇÕES E COMUNICAÇÕES
INSTITUTO NACIONAL DE PESQUISAS ESPACIAIS

sid.inpe.br/mtc-m21b/2017/05.22.17.16-TDI

CHARACTERISTICS AND ERROR MODELING OF GPM SATELLITE RAINFALL ESTIMATES DURING CHUVA CAMPAIGN IN BRAZIL

Rômulo Augusto Jucá Oliveira

Doctorate Thesis of the Graduate Course in Meteorology, guided by Dr. Daniel Alejandro Vila, approved in March 24, 2017.

URL of the original document:
<http://urlib.net/8JMKD3MGP3W34P/3NU3598>

INPE
São José dos Campos
2017

PUBLISHED BY:

Instituto Nacional de Pesquisas Espaciais - INPE
Gabinete do Diretor (GB)
Serviço de Informação e Documentação (SID)
Caixa Postal 515 - CEP 12.245-970
São José dos Campos - SP - Brasil
Tel.:(012) 3208-6923/6921
E-mail: pubtc@inpe.br

MINISTÉRIO DA CIÊNCIA, TECNOLOGIA, INOVAÇÕES E COMUNICAÇÕES
INSTITUTO NACIONAL DE PESQUISAS ESPACIAIS

sid.inpe.br/mtc-m21b/2017/05.22.17.16-TDI

CHARACTERISTICS AND ERROR MODELING OF GPM SATELLITE RAINFALL ESTIMATES DURING CHUVA CAMPAIGN IN BRAZIL

Rômulo Augusto Jucá Oliveira

Doctorate Thesis of the Graduate Course in Meteorology, guided by Dr. Daniel Alejandro Vila, approved in March 24, 2017.

URL of the original document:
<http://urlib.net/8JMKD3MGP3W34P/3NU3598>

INPE
São José dos Campos
2017

Cataloging in Publication Data

Oliveira, Rômulo Augusto Jucá.

Ol4c Characteristics and error modeling of GPM satellite rainfall estimates during chuva campaign in Brazil / Rômulo Augusto Jucá Oliveira. – São José dos Campos : INPE, 2017.

xxx + 129 p. ; (sid.inpe.br/mtc-m21b/2017/05.22.17.16-TDI)

Thesis (Doctorate in Meteorology) – Instituto Nacional de Pesquisas Espaciais, São José dos Campos, 2017.

Guiding : Dr. Daniel Alejandro Vila.

1. Satellite rainfall estimation. 2. Error modeling. 3. Uncertainty quantification. 4. Radar rainfall estimation. 5. Validation. I.Title.

CDU 556.12:551.507

Aluno (a): *Rômulo Augusto Jucá Oliveira*

"CHARACTERISTICS AND ERROR MODELING OF GPM SATELLITE RAINFALL ESTIMATES DURING CHUVA CAMPAIGN IN BRAZIL".

Aprovado (a) pela Banca Examinadora em cumprimento ao requisito exigido para obtenção do Título de *Doutor(a)* em *Meteorologia*

Dr. Dirceu Luis Herdies

Presidente / INPE / Cachoeira Paulista - SP

Dr. Daniel Alejandro Vila

Orientador(a) / INPE / Cachoeira Paulista - SP

Dr. Luiz Fernando Sapucci

Membro da Banca / INPE / Cachoeira Paulista - SP

Dra. Viviana Maggioni

Convidado(a) / GMU / Virginia - US

Dr. Carlos Augusto Morales Rodriguez

Convidado(a) / IAG/USP / São Paulo - SP

Este trabalho foi aprovado por:

( ) maioria simples

(x) unanimidade

São José dos Campos, 24 de março de 2017

To my parents, ***Medimar Olivera*** *and* ***Socorro Jucá****.*

ACKNOWLEDGEMENTS

I express my deep gratitude to my advisor, Daniel Vila, for believing in me in the realization of this work and for his constant motivation during my doctorate. It was really a pleasure to be guided by you. To my external advisor, Viviana Magginoi, for the amazing opportunity to work with you and your group at George Mason University (GMU) and for making your time available to discuss my research, always giving me nice orientation. To Carlos Morales, for being available to collaborate in my doctoral research and for the deep scientific discussions and past teaching. To Paul Kucera, for devoting part of his time to discussing my research and being open to host me at the National Center for Atmospheric Research (NCAR). To my committee members, Luiz Sapucci, Caio Coelho, and Dirceu Herdies for seeing it through and for the valuable contributions to my study. To Rachel Albrecht for the opportunity to contribute and learn in her discipline of Satellite Meteorology at IAG/USP during my teaching program. To Luiz Augusto Machado for the opportunity to participate in the CHUVA campaigns in Manaus and work with the CHUVA data set. To Thiago Biscaro and Aaron Funk for the radar data support.

I send my eternal gratitude to the family members, friends, and educators (it is a really extensive list) who directly and indirectly collaborated in the work in this Dissertation and provided me inspiration along the journey. Thanks also for the nice social life that you gave me. To Megan Bela for your steady love and for always being patient with me. I am sure that I have learned a lot being beside you!

I thank the CHUVA Project (FAPESP Grant 2009/15235-8), the Amazon Protection National System (SIPAM), Texas A & M University and the NASA/Goddard Space Flight Center's Mesoscale Atmospheric Processes Laboratory and PPS for the high quality data provided for this study. To the Satellite and Environmental Systems Division (DSA/CPTEC/INPE), the Civil, Environmental and Infrastructure Engineering Department at GMU, and the Research Applications Laboratory (RAL/NCAR) for the infrastructure required for the development of this research.

Finally, I thank the Brazilian government for the financial support of the National Council for Scientific and Technological Development (CNPq) (process 141230/2015-0) and the Coordination for the Improvement of Higher Education Personnel (CAPES) through my Ph.D. fellowship and the sponsorship of my program at the National Institute for Space Research (INPE), and also the CAPES Institutional Doctoral Overseas Sandwich Program (PDSE) (process 6836-15-1) for the internship opportunity.

ABSTRACT

Studies that investigate and evaluate the quality, limitations and uncertainties of satellite rainfall estimates are fundamental to assure the correct and successful use of these products in applications, such as climate studies, hydrological modeling and natural hazard monitoring. Over regions of the globe that lack in situ observations, such studies are only possible through intensive field measurement campaigns, which provide a range of high quality ground measurements, e.g., CHUVA (Cloud processes of tHe main precipitation systems in Brazil: A contribUtion to cloud resolVing modeling and to the GlobAl Precipitation Measurement) and GoAmazon (Observations and Modeling of the Green Ocean Amazon) over the Brazilian Amazon during 2014/2015. This study aims to assess the uncertainty of the Global Precipitation Measurement (GPM) satellite constellation in representing the main characteristics of precipitation over different regions of Brazil. The Integrated Multi-satellitE Retrievals for GPM (IMERG) (level-3) and the Goddard Profiling Algorithm (GPROF) (level-2) algorithms are evaluated against ground-based radar observations, specifically, the S-band weather radar from the Amazon Protection National System (SIPAM) and the X-band dual polarization weather radar (X-band CHUVA radar) as references. The space-based rainfall estimates, based on active microwave (e.g., TRMM-PR and GPM-DPR [at Ku-band] radars) are also used as references. The results for the CHUVA-Vale campaign suggest that GPROF has relatively good agreement (spatial distribution and accumulated rainfall), especially for convective rain cases, due the significant presence of ice scattering. However, the intensity and volume of light/moderate rains is overestimated and performance related to light/heavy rains (underestimated) are intrinsically linked to convective-stratiform rainfall occurrences over the study region. For the study over the Central Amazon Region (CHUVA-GoAmazon), results showed that during the wet season, IMERG, which uses the GPROF2014 rainfall retrieval from the GPM Microwave Imager (GMI) sensor, significantly overestimates the frequency of heavy rainfall volumes at around 00:00–04:00 UTC and 15:00–18:00 UTC. This overestimation is particularly evident over the Negro, Solimões and Amazon rivers due to the poorly-calibrated algorithm over water surfaces. On the other hand, during the dry season, the IMERG product underestimates mean precipitation in comparison to the S-band SIPAM radar, mainly due to the fact that isolated convective rain cells in the afternoon are not detected by the satellite precipitation algorithm. The study based on verification of GPM level 2 by traditional and object-based analysis shows that although volume and occurrence of heavy rainfall are underestimated, a good agreement of GPROF2014 for TMI and GMI versus TRMM PR and GPM DPR (Ku band) rainfall retrievals, respectively, was noted. Such most evident good performances were found through continuous and categorical analyses, especially during the wet season, where the number of objects and larger areas were observed. The larger object area seen by GPROF2014(GMI) compared to DPR (Ku band) was directly linked to the structure of vertical profiles of the precipitanting systems and the presence of bright band was the main source of uncertainty on the estimation

of precipitation area and intensity. The results via error modeling, through the Precipitation Uncertainties for Satellite Hydrology (PUSH) framework, demonstrated that the PUSH model was suitable for characterizing the error from the IMERG algorithm when applied to S-band SIPAM radar estimates. PUSH could efficiently predict the error distribution in terms of spatial and intensity distributions. However, an underestimation (overestimation) of light satellite rain rates was observed during the dry (wet) period, mainly over the river. Although the estimated error showed a lower standard deviation than the observed error, they exhibited good correlations to other, especially in capturing the systematic error along the Negro, Solimões and Amazon rivers, especially during the wet season.

Keywords: Satellite Rainfall Estimation. Error Modeling. Uncertainty Quantification. Radar Rainfall Estimation. Validation.

CARACTERÍSTICAS E MODELAGEM DE ERRO NAS ESTIMATIVAS DE PRECIPITAÇÃO DO SATÉLITE GPM DURANTE AS CAMPANHAS DO CHUVA NO BRASIL

RESUMO

Estudos que investigam e avaliam a qualidade, limitações e incertezas das estimativas de precipitação de satélites são fundamentais para assegurar o uso correto e bem-sucedido desses produtos em aplicações, como estudos climáticos, modelagem hidrológica e monitoramento de desastres naturais. Em regiões do globo que não possuem observações in situ, esses estudos apenas são possíveis através de campanhas intensivas de medição de campo, que oferecem uma gama de medições de superfície de alta qualidade, por exemplo, CHUVA (Cloudprocesses of tHe main precipitation systems in Brazil: A contribUtion to cloud re-solVing modeling and to the GlobAl Precipitation Measurement) e GoAmazon (Observations and Modeling of the Green Ocean Amazon) sobre a Amazônia Brasileira durante 2014/2015. Este estudo tem como objetivo avaliar as incertezas provenientes da constelação de satélites do Global Precipitation Measurement (GPM) em representar as principais características da precipitação em diferentes regiões do Brasil. Os algoritmos Integrated Multi-satellitE Retrievals for GPM (IMERG) (level-3) e Goddard Profiling Algorithm (GPROF) (level-2) são avaliados em contraste as observações de radares meteorológicos, especificamente, do Sistema Nacional de Proteção da Amazônia (SIPAM) e o radar meteorológico banda X de dupla polarização (X-band CHUVA radar) como referência. As estimativas de precipitação, baseadas em radares de microondas ativos (por exemplo, radares TRMM-PR e GPM-DPR [na banda Ku]) também são utilizadas como referência. Os resultados da campanha CHUVA-Vale sugerem que o GPROF possui uma boa concordância (distribuição espacial e precipitação acumulada), especialmente para casos de chuva convectiva, devido à presença significativa de espalhamento por gelo. No entanto, a intensidade e volume de chuvas leves/moderadas é superestimada e um desempenho (subestimado) relacionado às chuvas fracas/intensas diretamente ligado às ocorrências de chuvas convectivas-estratiformes na região do estudo. Para o estudo da região da Amazônia Central (CHUVA-GoAmazon), os resultados mostraram que, durante a estação chuvosa, o IMERG, que utiliza as estimativas de precipitação do GPROF2014 a partir do sensor GPM Microwave Imager (GMI), superestima significativamente a freqüência de chuvas intensas em torno de 00:00-04:00 UTC e 15:00-18:00 UTC. Essa superestimativa é particularmente evidente nos rios Negro, Solimões e Amazonas devido ao algoritmo apresentasse erroneamente calibrado sobre as superfícies de água. Por outro lado, durante a estação seca, o produto IMERG subestima a precipitação média em comparação com o radar banda-s do SIPAM, principalmente devido ao fato de que células convectivas isoladas à tarde não são detectadas por tal algoritmo. O estudo baseado na verificação das estimativas do GPM Level 2 por abordagens tradicional e baseada em objeto mostra que, embora a subestimiativa do volume e ocorrência de chuvas intensas, foi observada uma boa concordância do GPROF2014 (TMI e GMI) versus TRMM PR e GPM DPR (Ku band), Respectivamente. Tais evidentes melhores desempenhos foram encontrados através de análises contínua e categórica, especialmente durante a estação chuvosa, onde o maior número e maiores áreas de

objetos foram observados. As maiores áreas, observadas pelo GPROF2014 (GMI) comparada ao DPR (banda Ku) esteve diretamente ligada à estrutura de perfis verticais dos sistemas de precipitantes e a presença de banda brilhante foi a principal fonte de incerteza na estimativa da área e intensidade de precipitação. Os resultados referentes à modelagem do erro, através da ferramenta Precipitation Uncertainties for Satellite Hydrology (PUSH), as análises demonstraram que o modelo PUSH foi adequado para caracterizar o erro do algoritmo IMERG quando aplicado às estimativas de radar banda S do SIPAM. O modelo PUSH pôde prever eficientemente a distribuição de erro em termos espaciais e de intensidade. No entanto, observou-se uma subestimativa (superestimativa) das taxas de chuva fracas do satélite durante o período seco (chuvoso), especialmente ao longo do rio. Embora o erro estimado tenha apresentado menor desvio padrão do que o erro observado, eles apresentaram boas correlações entre si, especialmente na captura do erro sistemático ao longo dos rios Negro, Solimões e Amazonas, especialmente durante a estação chuvosa.

Palavras-chave: Estimativa de Precipitação por Satélite. Modelagem de Erro. Quantifição de Incertezas. Estimativa de Precipitação por Radar. Validação.

LIST OF FIGURES

Page

LIST OF TABLES

Page

LIST OF ABBREVIATIONS

AMSR-2	–	Advanced Microwave Scanning Radiometer 2
AMSR-E	–	Advanced Microwave Scanning Radiometer for EOS
BIAS	–	Bias score
bias	–	Mean error
CAPPI	–	Constant Altitude Plan Position Indicator
CFAD	–	Contoured Frequency by Altitude Diagram
CHUVA	–	Cloud processes of tHe main precipitation systems in Brazil: A contribUtion to cloud resolVing modeling and to the GPM (GlobAl Precipitation Measurement)
CHUVA-VALE	–	CHUVA Vale do Paraíba campaign
CMORPH-KF	–	CPC Morphing-Kalman Filter Lagrangian time interpolation scheme
CNES	–	Centre National d'Études Spatiales
COR	–	Correlation coefficient
CPC	–	Climate Prediction Center
CRM	–	Cloud resolving models
CSI	–	Critical success index
DMSP	–	Defense Meteorological Satellite Program
DPATC	–	Dual-Pol based Attenuation Correction
DPR	–	Dual Precipitation Radar
DPSRI	–	Dual Polarization Surface Rainfall Intensity
DSD	–	Drop size distribution
EOS	–	Earth Observing System
EUMETSAT	–	European Organization for the Exploitation of Meteorological Satellites
FAR	–	False alarm ratio
GCOMW1	–	Global Change Observation Mission Water 1
GMI	–	GPM Microwave Imager
GoAmazon	–	Observations and Modeling of the Green Ocean Amazon
GPCP	–	Global Precipitation Climatology Project
GPM	–	Global Precipitation Measurement
GPROF	–	Goddard Profiling Algorithm
GSMaP	–	Global Precipitation Satellite Mapping
HSS	–	Heidke skill score
IEAv	–	Institute for Advanced Studies
IMERG	–	Integrated Multi-satellitE Retrievals for GPM
IOP	–	Intensive Operating Period
IPWG	–	International Precipitation Working Group
IR	–	Infrared
ISRO	–	Indian Space Research Organization
JAXA	–	Japan Aerospace Exploration Agency

LUTs	–	Lookup tables
MCCs	–	Mesoscale Convective Complexes
MET	–	Model Evaluation Toolkit
METOP(A/B)	–	European Meteorological Operational A and B
MHS	–	Microwave Humidity Sounder
MODE	–	Method for Object-Based Diagnostic Evaluation
MT1	–	Megha-Tropiques 1
MW	–	Microwave
NASA	–	National Aeronautics and Space Administration
NCAR	–	National Center for Atmospheric Research
NOAA	–	National Oceanic and Atmospheric Administration
PCT	–	Polarization-corrected temperature
PDF	–	Probability density function
PDFc	–	PDF by occurrence
PDFv	–	PDF by volume
PEHRPP	–	Program to Evaluate High Resolution Precipitation Products
PERSIANN-CCS	–	Precipitation Estimation from Remotely Sensed Information using Artificial Neural Networks-Cloud Classification System re-calibration scheme
PhiDP	–	Total differential Phase
PMW	–	Passive microwave
POD	–	Probability of detection
PR	–	Precipitation Radar
PUSH	–	Precipitation Uncertainties for Radiométrie
RMSE	–	Root mean square error
RRx	–	Rain rate
SACZ	–	South Atlantic Convergence Zone
SAPHIR	–	Sondeur Atmosphérique du Profil d'Humidité Intertropicale par Satellite Hydrology
SD	–	Standard deviation
SIPAM	–	Sistema Nacional de Proteção da Amazônia
SR	–	Success ratio
SSM/I	–	Special Sensor Microwave/Imager
SSMI/S	–	Special Sensor Microwave Imager/Sounder
Tb	–	Brightness temperature
TMI	–	TRMM Microwave Imager
TMPA	–	TRMM Multi-satellite Precipitation Analysis
TRMM	–	Tropical Rainfall Measuring Missio
UNIVAP	–	Vale do Paraíba University
VIS	–	Visible
Z	–	Reflectivity

ZDR – Differential reflectivity
ZPHI – Rain Profiling Algorithm

CONTENTS

Page

1 INTRODUCTION

1.1 Introduction and context

The forecast and quantification of rain with the highest possible accuracy, especially for severe weather situations, over various temporal and spatial scales, are extremely important to society because they are directly linked to the economy through agriculture, natural resources, transportation, and the prediction and detection of natural disaster occurrences. However, it is known that precipitation varies both spatially and temporally, as well as in its intensities, thus making its accurate measurement difficult to perform with only the use of rain gauges, which provide point surface measurements, in many cases providing only daily records, and depending on the region, may present low density (for example over the Amazon, mountainous regions, ocean and others).

In this context, the remote sensing of precipitation has played a fundamental role in the improvement and complementarity of spatial and temporal characteristics. Technologically sophisticated instruments, located on the surface (such as radars [e.g., single and double polarizations]) and on-board orbital platforms (such as active and passive microwave sensors) have been expanding our temporal-spatial vision, providing detailed information on both precipitation and microphysical characteristics across the distinct regions of the globe.

Satellite rainfall estimates have been widely used for various purposes (e.g., real-time weather monitoring and forecasting, hydrological modeling and climate studies, among others). The quality of satellite rainfall products has improved significantly in recent decades, especially with the advent of satellites/missions such as the Tropical Rainfall Measuring Mission (TRMM) (KUMMEROW et al., 1998) and the Global Precipitation Measurement (GPM) (HOU et al., 2014), as reported by Levizzani et al. (2007). However, such algorithms require validation studies using observational rainfall data, preferably at high spatial-temporal resolution. In this context, the Program to Evaluate High Resolution Precipitation Products (PEHRPP), established within the International Precipitation Working Group (IPWG) (IPWG, 2017), was a collaborative effort to evaluate, intercompare and validate the several high-resolution precipitation algorithms (level-2 and level-3) currently available and operational, e.g., Ebert (2007), Turk F.J. (2008), Sapiano e Arkin (2009), Di Paola et al. (2012), Casella et al. (2012) and Mugnai et al. (2013a).

Analogous to this, various efforts to quantify the error characteristics and uncertain-

ties of satellite based precipitation estimation have emerged, for example, through the GPM field measurement campaigns in distinct regions of the globe. The CHUVA project (Cloud processes of tHe main precipitation systems in Brazil: The contribution to cloud resolving modeling and to the GPM [Global Precipitation Measurement]) is a research project that aims to study clouds and precipitation processes through six field experiments in different precipitation regimes in Brazil. One of the major goals of the CHUVA project is to evaluate and improve the quality of satellite-based precipitation estimates of the GPM constellation (MACHADO et al., 2014).

In general, validation studies have focused on the evaluation of the performance of certain products of satellite precipitation estimates, in general based on infrared (IR) or microwave observations and their combinations (MUGNAI et al., 2013b). Typically the comparisons are made using rain gauges (e.g., Vila et al. (2009) and Puca et al. (2014)). However, studies using other data sources have been widely used, e.g., active microwaves (AONASHI et al., 2009), dual polarization weather radars (e.g., Liao et al. (2001), Chandrasekar et al. (2008), Cimini et al. (2013), disdrometers (MORALES et al., 2013), among others. Extensive information on actual, ongoing and future activities/plans regarding precipitation measurement (observational, modeling and from satellites) and its performance and applications are given by Michaelides et al. (2009), Levizzani et al. (2007), Kidd e Levizzani (2011), Tapiador et al. (2011) and Kucera et al. (2013). Applications, as well as pros and cons, of various verification techniques and point to point (pixel-based) validation through traditional and spatial (e.g., object-oriented approaches) techniques are shown in Ebert (2007).

1.2 Problem description, motivation and scientific questions

Satellite rainfall estimation (microwave, infrared, hybrid, etc.) has been widely used in Brazil for various purposes, e.g. for monitoring natural disasters, hydrological purposes and climatic applications. Although the quality of satellite rainfall estimate products has improved significantly in recent decades, such algorithms require careful validation studies, which aim to provide information about their qualities, limitations and associated uncertainties.

The uncertainties in satellite rainfall estimates arise from different factors, including the sensor itself, retrieval error, and spatial and temporal sampling, among others (HONG et al., 2006; TANG et al., 2015). However, the definition and quantification of uncertainty are directly and indirectly based on the error model definition (TIAN et al., 2013). In general, two types of error models are commonly used for uncertain-

ties in precipitation measurements (satellite and radar estimates): *i*) the additive error model and *ii*) the multiplicative error model. However, according to Tian et al. (2013), the multiplicative error model better separates systematic and random errors, is applicable to the wide range of variability in daily precipitation and produces superior predictions of the error characteristics. Considering this, Maggioni et al. (2014) proposed an error model framework called Precipitation Uncertainties for Satellite Hydrology (PUSH) in order to provide an estimate of the error associated with high-resolution satellite precipitation products for each grid point and time step. The probability density function (PDF) of the actual rainfall is modeled differently, decomposing the error in satellite rainfall estimates in each of the following four steps (of rain and no-rain cases): *i*) correct no-precipitation detection, *ii*) missed precipitation, *iii*) false alarm and *iv*) hit. The resulting error estimates, provided by the PUSH framework, could be applied to any corresponding high-resolution satellite precipitation products and other regions of the globe, if it is well adapted and adjusted to the study region and local characteristics (i.e., surface type, seasonality factor, among others).

Thus, the understanding and quantification of errors are extremely important for successful applications of satellite rainfall estimate products in hydrological modeling, data assimilation systems, climate studies and water management policy. Such analyses also contribute by providing arguments for algorithm developers and assist in improving precipitation estimation over a given location and surface type. In parallel, they support better algorithm efficiency in detecting precipitation type and monitoring precipitation system life cycles over certain regions, which are among the main gaps to be filled by the GPM and CHUVA projects.

Given this background, the main question that motivated this research is: *How can the GPM constellation contribute to improve over-land precipitation characterization by understanding its associated uncertainties?* To support this general scientific question, this study seeks to answer the following specific questions:

- What are the main characteristics (performance) of GPROF (version 2004) over-land rainfall retrievals in representing different classes of instantaneous rain rates (from light to heavy rainfall) over the Southeast region of Brazil? (Chapter 3)
- What is the current performance of the two official GPM rainfall algorithms (GPROF and IMERG) in characterizing the diurnal cycle of precipitation over the central Amazon region? (Chapter 4)

- How well can GPM PMW rainfall retrievals (GPROF2014 for TMI and GMI) represent the main physical characteristics of precipitating systems (e.g. numbers, total area, position distributions, among others) over the Brazilian Amazon? (Chapter 5)

- What are the characteristics and distribution of uncertainties of GPM satellite rainfall estimates over the different regions of Brazil via error modeling? How those uncertainties can be minimized for correct applications? (Chapter 6)

1.3 Objectives

The main objective of this study is to evaluate the capability of the GPM constellation of satellites to reproduce the characteristics of over-land precipitation over different regions of Brazil. This study also investigates the error characteristics of the main GPM rainfall algorithms in order to minimize the associated uncertainties over different regions of Brazil. To achieve the main goal of this research, the follow specific objective are addressed:

- Evaluate the efficiency (strengths and limitations) of GPROF (version 2004) over-land rainfall retrievals in representing the different classes of instantaneous rain-rates (from light to heavy rainfall) over the Southeast region of Brazil.

- Evaluate the ability of two official GPM rainfall products (GPROF and IMERG) to reproduce the main characteristics and diurnal cycle of precipitation observed over the central Amazon region.

- Evaluate the performance of the actual GPM PMW rainfall retrievals in representing the main physical characteristics of precipitating systems over the Brazilian Amazon using distinct statistical approaches, such as traditional and object-based techniques.

- Investigate and characterize the uncertainties of GPM satellite rainfall estimates over the central Amazon region via error modeling.

1.4 Thesis structure

The thesis is structured in seven chapters. Figure 1.1 presents a general overview of the topics covered in each chapter and how they are linked to each other.

A brief introduction to the thesis theme is provided in **Chapter 1**. The main scientific questions that motivated this research are also shown in this chapter. **Chapter 2** presents a literature review, which provides a general overview of satellite precipitation estimation techniques, statistical verification/validation analysis, and error modeling methods applied to satellite precipitation products. This chapter serves as a theoretical basis for the methodology developed here. A brief description of the GPM and CHUVA Projects is also included in this chapter. The research developed

Figure 1.1 - Overview of the thesis and its main addressed points.

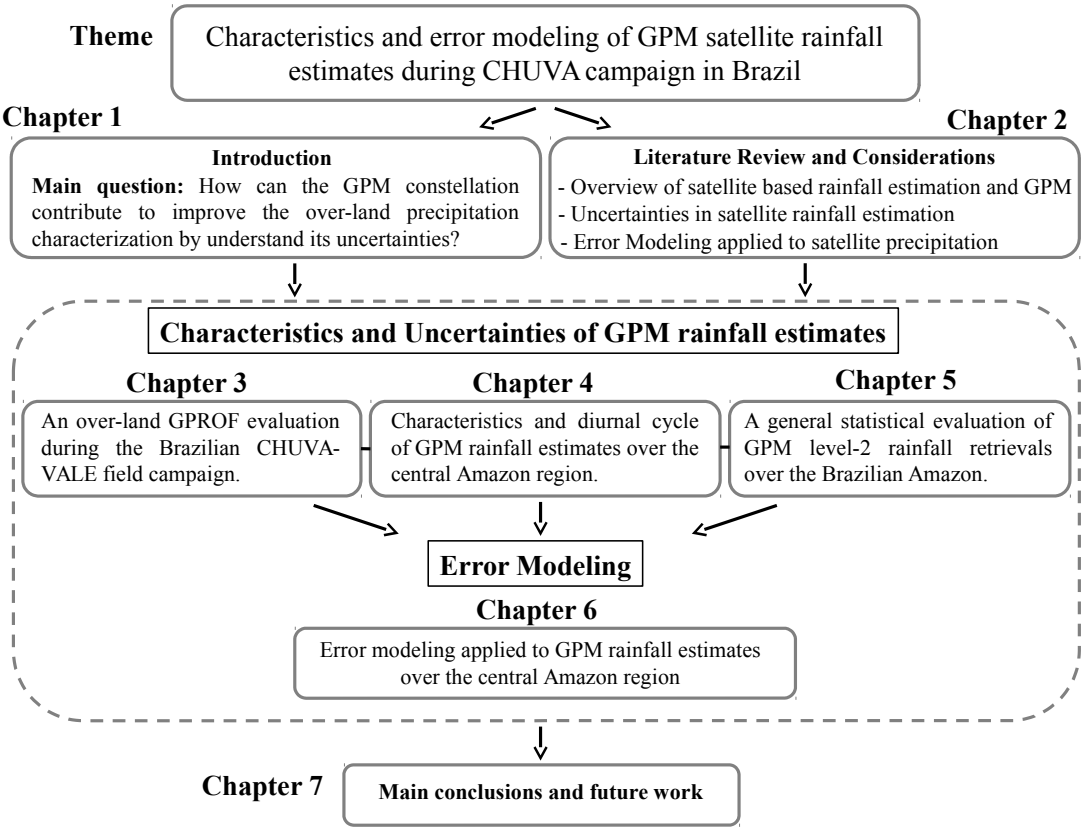

SOURCE: Author's production.

in this thesis is divided into 4 chapters. **Chapter 3**, **4** and **5** aim to better understand the uncertainties in satellite-based rainfall estimates over different regions of Brazil. **Chapter 3** statistically evaluates the performance of over-land GPROF rainfall retrievals over the Southeast region of Brazil during the CHUVA-VALE campaign (rainy season). **Chapter 4** analyzes the characteristics and the diurnal cycle of GPM rainfall estimates over the central Amazon region, making a perfor-

mance contrast between the dry and rainy seasons. In **Chapter 5**, the performance of GPM-Level 2 rainfall retrievals over the Brazilian Amazon are performed using three complementary methods (i.e., traditional, spatial and object-based verification approaches). Lastly, in order to improve the GPM-Level 3 rainfall estimates over the continent by understand and minimizing its associated uncertainties, **Chapter 6** is focused on the adjusted and validated error model for the central Amazon region, for a better precipitation characterization.

Finally, the main conclusions and the future works are given in **Chapter 7**.

Thus, in order to answer the thesis objectives, a series of studies have been developed that are presented in chapters 3 to 6 in the form of articles, written based on the following publications:

Chapter 3: OLIVEIRA, R. A.; BRAGA, R. C.; VILA, D. A.; MORALES, C. A. Evaluation of GPROF-SSMI/S rainfall estimates over land during the brazilian CHUVA-VALE campaign. **Atmospheric Research**, v. 163, p. 102 – 116, 2015. ISSN 0169-8095. Impact Factor: **3.377**.

Chapter 4: OLIVEIRA, R.; MAGGIONI, V.; VILA, D.; MORALES, C. Characteristics and diurnal cycle of GPM rainfall estimates over the central Amazon region. **Remote Sensing**, v. 8, n. 7, 2016. Impact Factor: **3.036**.

Chapter 5: OLIVEIRA, et al. Performance of GPM-Level 2 rainfall retrievals over the Brazilian Amazon using Traditional and object-based methods. *In preparation.*

Chapter 6: OLIVEIRA, et al. Error modeling applied to GPM-Level 3 rainfall estimates over the central Amazon region: characteristics and validation. *In preparation.*

2 LITERATURE REVIEW AND CONSIDERATIONS

2.1 Overview of satellite based rainfall estimation and GPM

Methods for precipitation estimates from satellite radiance measurements have evolved from methods based on visible (VIS) and infrared (IR) observations for active and passive (MW) microwave techniques and approaches considering a combination of IR and MW (blended techniques).

The Tropical Rainfall Measuring Mission (TRMM) satellite (lunched in November 1997) (KUMMEROW et al., 1998), has made a major contribution to the advancement of satellite precipitation estimation by providing simultaneous high resolution observations, through its microwave imager (TMI) and precipitation radar (PR) sensors. The TRMM PR version 7 (V7) precipitation estimates (2A25 product), described in Iguchi et al. (2000), provides 3D reflectivity and 2D rain rate fields at the ground for both land and ocean surfaces throughout the tropics.

As TRMM's successor, the Global Precipitation Measurement (GPM) mission (HOU et al., 2014; NASA, 2017), is an effort of the National Aeronautics and Space Administration (NASA) and the Japan Aerospace Exploration Agency (JAXA) and open to other meteorologic and space agencies, which includes the Centre National d'Études Spatiales (CNES), the Indian Space Research Organization (ISRO), the National Oceanic and Atmospheric Administration (NOAA), the European Organization for the Exploitation of Meteorological Satellites (EUMETSAT), among others). GPM aims to monitor and better understand the global precipitation through its constellation of satellites at high spatial and temporal resolutions based on its quasi-global high quality and fine resolution rainfall estimates, both at the sensor level (Level-2), in terms of active and passive microwave (PMW), and at the final gridded level (Level-3). This is possible thanks to several instruments on board the GPM core observatory, i.e., a dual-frequency precipitation radar (DPR; Ku-band at 13.6 GHz and Ka-band at 35.5 GHz) and a conical-scanning multichannel GPM Microwave Imager (GMI; frequencies range between 10 and 183 GHz), and to its other constellation satellites (e.g., the Defense Meteorological Satellite Program (DMSP) F16, F17 and F18 satellites; the National Oceanic and Atmospheric Administration (NOAA)-18 and 19 satellites; among others). The DPR has an improvement in the detection of weak rains, in the information on the distribution of particle size of precipitation and snow, as well as in the identification of vertical structure consistent to the particles in the mixed, ice and liquid phase (IGUCHI et al., 2002). The two official GPM era algorithms are the Level-2 Goddard Profiling Algorithm (GPROF2014) and the

Level-3 Integrated Multi-satellitE Retrievals for GPM (IMERG).

The monitoring of precipitation from the passive microwave (PMW) is made using the atmospheric transmittance windows below 20 GHz, from 30 to 40 GHz, and around 90 GHz (BARRETT; KNIVETON, 1995), although the high-frequency channels above 100 GHz have been shown to be very useful for this purpose (e.g., Ferraro et al. (2005)).

Below 20 GHz, rainfall absorption and emission are predominant and, over ocean surfaces, where emissivity, ε, is low (ε ∼0.4–0.5) and consstant, the PMW algorithms take advantage of the contrast between the raindrops and the ocean surface. Otherwise, land surfaces are characterized by presenting high emissivity values (ε ∼0.9). In addition, land surfaces present high emissivity variability (spatially and temporally), which is associated with the soil property and vegetation (the variability is dependent on the soil moisture and surface roughness). Thus, it becomes difficult to distinguish the emission by liquid water suspended aloft over land surfaces. Therefore, PMW algorithms must estimate rainfall above land surfaces from the scattering of high-frequency microwave radiation (>60 GHz) from the precipitation-sized ice crystals in convective clouds (EBERT, 2007). Between 20–60 GHz, a combination of absorption/emission and scattering processes are present. The absorption and scattering of ice and water particles are clearly dependent on their size relative to the microwave frequency. For frequencies in the region of 22 GHz to 31 GHz, ice crystal scattering is negligible, so that the ice clouds are transparent to these microwave frequencies. For example, at around 22.3 GHz and between 50-60 GHz, maximum attenuation is due to water vapor and oxygen absorptions, respectively. At 37 GHz (Ka band) a mixture of emission and scattering is depicted. Since this channel is more appropriate for ocean surface applications, on the continent it is necessary to jointly use the horizontal and vertical polarizations in order to reduce the effects of emissivity of non-uniform surfaces. An additional technique is to combine it with other channels (e.g., 85.5 GHz). An example of 37 and 85.5 GHz horizontal and vertical polarization applications is the polarization-corrected temperature (PCT) method, introduced by SPENCER (1986) and SPENCER et al. (1989). This method makes it possible to delineate areas of rainfall in convective systems and over varying surface types (KIDD, 1998).

The use of scattering methods for rainfall estimation have the advantage of being potentially applicable over both ocean and land surfaces, as well as coastal regions. The sensitivity to ice scattering occurs at 85.5 GHz, which is the most appropriate

channel for estimating precipitation over land (when there is ice present in the cloud). However, the measurement of precipitation through the high-frequency channels is an indirect approach, which is based on the implicit relationship between the presence of large particles (ice scattering) aloft and the precipitation below.

One of the most widely used techniques for rainfall retrieval using passive microwave radiometers on board low-orbiting satellites (e.g., through the TMI, Advanced Microwave Scanning Radiometer for EOS [AMSR-E], Special Sensor Microwave/Imager [SSM/I] and Special Sensor Microwave Imager/Sounder [SSMIS] sensors) is the Goddard Profiling Algorithm (GPROF), originally proposed by Kummerow et al. (1996) and OLSON et al. (1999). GPROF 2004 is a multichannel physical approach for retrieving both the instantaneous rainfall and rainfall vertical structure information by using a Bayesian approach to match the brightness temperatures to hydrometeor profiles derived from cloud resolving models (CRM). A radiative transfer model based on a onedimensional Eddington approximation (KUMMEROW, 1993) is used to compute brightness temperatures from the CRM hydrometeor profiles at the observed satellite frequencies (KUMMEROW et al., 1996; KUMMEROW et al., 2001; OLSON et al., 2007; VILA et al., 2010; VILA et al., 2013).

The GPROF 2004 algorithm, which was originally developed for SSM/I (Kummerow et al., 2001) was adapted for the Defense Meteorological Satellite Program (DMSP) SSMI/S (see Vila et al. (2013)) for use with the F-16, F-17, and F-18 satellites. The SSMI/S is a conically scanning passive microwave radiometer that combines and extends the imaging and sounding capabilities of SSM/I, using three separate DMSP microwave sensors (SSM/T, SSM/T2, and SSM/I), with a 53.1 ° Earth incidence angle, sensing upwelling microwave radiation in 24 channels from 19 - 183 GHz. The SSM/I operates in the frequency range from 19.3 to 85.5 GHz. The SSMI/S imaging channels maintain similar resolution and spectral frequency to the SSM/I, except 91.655 GHz on SSMI/S versus 85.5 GHz on SSM/I. Vila et al. (2013) showed a very good agreement of the SSMI/S version of GPROF2004 for all analyzed variables, such as over land rain rate, total precipitable water and liquid water path, when compared with the SSM/I version, during the period when both satellites were flying together. In its current version (2014, Version 1.4), GPROF is applicable to different PMW sensors (imagers and sounders) and scan types (conical and cross-track), such as SSMI/S sensor on the DMSP(F16/F17/F18) satellites; Advanced Microwave Scanning Radiometer 2 (AMSR2) on board the Global Change Observation Mission-Water 1 (GCOMW1) satellite; GMI on board the GPM core observatory; TMI on TRMM satellite; Sondeur Atmosphérique du Profil d'Humidité Intertropicale par

Radiométrie (SAPHIR) on Megha-Tropiques 1 (MT1); Microwave Humidity Sounder (MHS) on board the European Meteorological Operational A and B (METOP(A/B)) and the NOAA 18 and 19, as described by Kummerow et al. (2015) and Kidd et al. (2016).

On the other hand, given the pros and cons VIS/IR observations, as well as PMW and AMW (e.g., the limited temporal resolution of two overpasses per day over a specific location on globe), several algorithms have been elaborated over the years, based on the combination of VIS/IR and PMW (blended techniques), focused on global real time monitoring. As described in Levizzani et al. (2007) and Michaelides et al. (2009), the blended techniques can be divided into two main categories: *i*) methods that use auxiliary products from other PMW sensors to adjust as precipitation intensities derived from PMW (e.g., Huffman et al. (2007)), and *ii*) those using auxiliary data, such as VIS/IR observations, to advect rain maps from the PMW sensor overpasses to others (JOYCE et al., 2004). Among the several algorithms are: TRMM Multi-satellite Precipitation Analysis (TMPA) 3B42 (Version 7) and 3B42RT (Real Time) (HUFFMAN et al., 2007; HUFFMAN et al., 2010); The Climate Prediction Center (CPC) Morphing-Kalman Filter Lagrangian time interpolation scheme (CMORPH-KF) (JOYCE et al., 2004; JOYCE; XIE, 2011); The Precipitation Estimation from Remotely Sensed Information using Artificial Neural Networks-Cloud Classification System re-calibration scheme (PERSIANN-CCS) (HONG et al., 2004); the Global Precipitation Satellite Mapping (GSMaP) (KUBOTA et al., 2007), among others.

Currently, the IMERG (HUFFMAN et al., 2014), the GPM's official algorithm, takes into account its precipitation estimates from other products, at level 2 and 3, such as the GPROF2014 algorithm, as well as the TMPA, CMORPH-KF and PERSIANN-CCS algorithms, as well as rainfall observations from the Global Precipitation Climatology Project (GPCP). IMERG offers precipitation fields at spatial-temporal resolution of 0.1 degrees every 30 minutes. More about the IMERG algorithm are found along the chapters.

2.1.1 The CHUVA project

The CHUVA Project, as part of the GPM Project GPM-Brazil, is a research project to study cloud processes and precipitation through six field experiments in different precipitation regimes in Brazil, such as Alcântara-MA, Fortaleza-CE, Belém-PA, São José dos Campos-SP, Santa Maria-RS and Manaus-AM (Figure 2.1). The objective of the CHUVA field campaigns is to collect information about the cloud processes

of the main precipitating systems over Brazil (e.g., squall lines in the Amazon; Mesoscale Convective Complexes [MCCs], cold fronts, middle latitude squall lines and the South Atlantic Convergence Zone [SACZ] in the South region) in order to evaluate and improve quality satellite-based precipitation estimates and knowledge of cloud microphysical processes (MACHADO et al., 2014). In addition, the observations from these regions provide a representative set of cases to evaluate the performance of the algorithms for these types of events. The last CHUVA field experiment, held in Manaus (Amazon, Brazil) in 2014, was organized in cooperation with another research project named GoAmazon (Observations and Modeling of the Green Ocean Amazon). The GoAmazon experiment was motivated by the need for gaining a better understanding of aerosol-cloud-precipitation interactions and processes over the largest tropical rain forest on Earth (MARTIN et al., 2016; GOAMAZON, 2017). More about the CHUVA Project and its field campaign can be accessed at `http://chuvaproject.ctec.inpe.br/` (CHUVA, 2017).

Figure 2.1 - Schematic map describing the CHUVA field campaigns, illustrating the main precipitation regimes over different regions of Brazil and, the reference measurement strategy adopted during the field campaigns by distinct instruments.

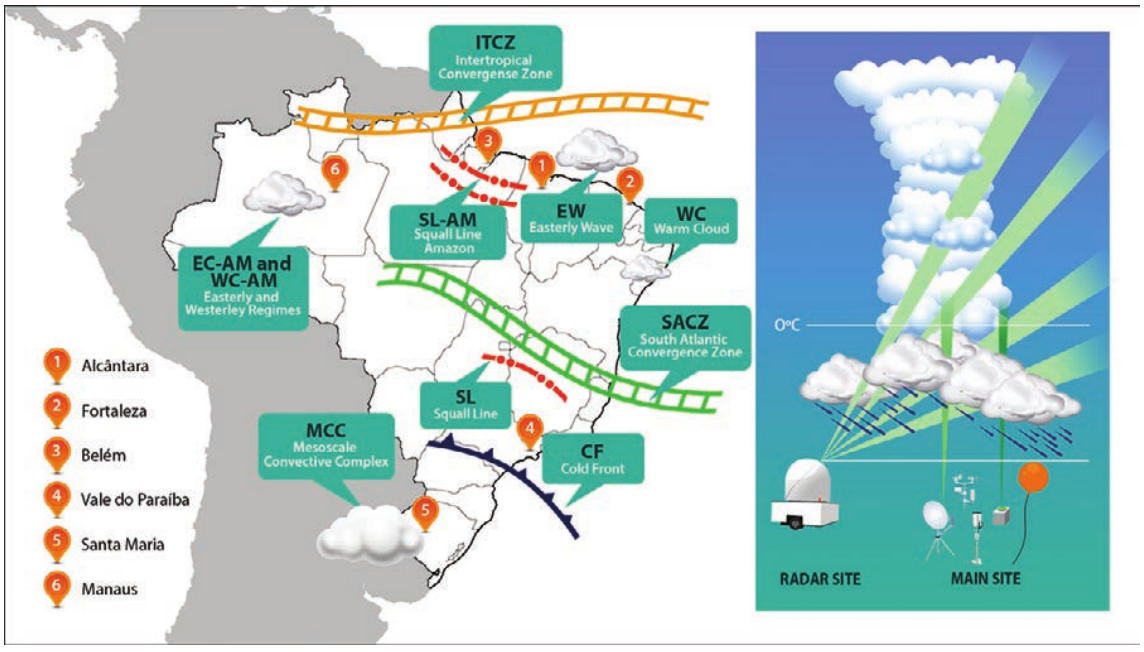

Location of the CHUVA field campaigns over the different regions of Brazil and its main precipitation regimes (left). The reference measurements during the field campaigns (right).

SOURCE: Machado et al. (2014).

As an example of the available satellite from GPM database, Figure 2.2 shows all the satellite/sensors overpasses from the GPM constellation over the central Amazon region (within a 60 km radius of the X-band CHUVA radar), during the CHUVA/GoAmazon (1st and 2nd Intensive Operating Periods [IOPs], March and September 2014, respectively). It is important to note that both the conical and cross-track PMW satellite sensors from GPM constellation have a quasi-total daily coverage, with certain preferential hour times by each satellite/sensor (up to two sampling overpasses per day) over the central Amazon region.

Figure 2.2 - Satellite/sensors overpasses from the GPM constellation database over the central Amazon region, during the CHUVA/GoAmazon (IOP1 and IOP2).

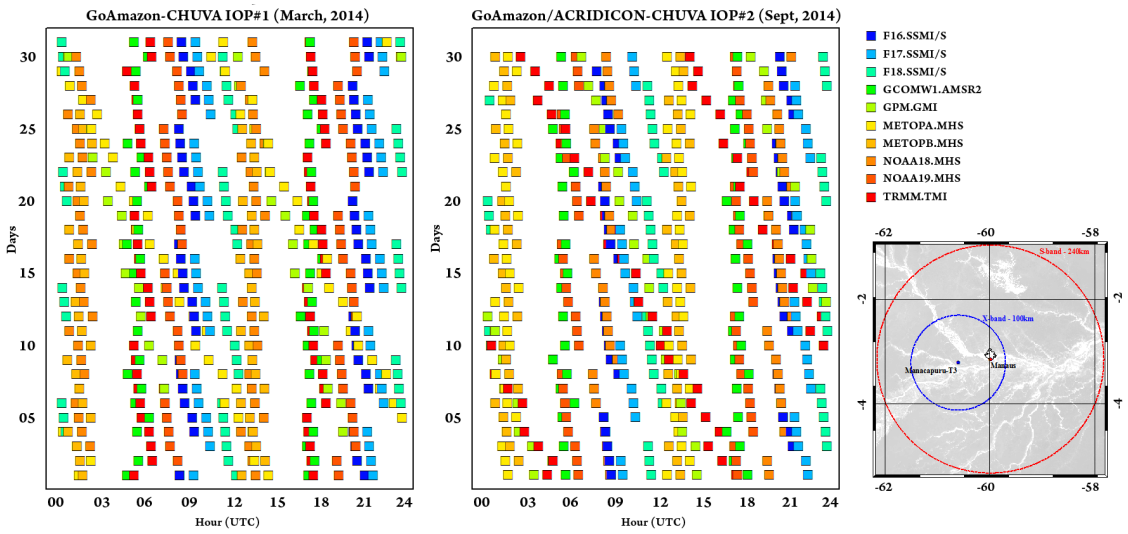

Overpasses within a 60 km radius of the X-band CHUVA radar (on right).

SOURCE: Author's production.

2.2 Uncertainties in satellite rainfall estimation

Many recent studies have evaluated the accuracy of satellite precipitation products, for example against ground-based radar rainfall estimates and/or rain gauges as a reference (PETKOVIĆ; KUMMEROW, 2015; GUO et al., 2015; TANG et al., 2015; AGHAKOUCHAK; MEHRAN, 2013; PRAKASH et al., 2016a; TANG et al., 2016; PRAKASH et al., 2016b). The performance of satellite based precipitation estimates is generally evaluated using traditional error metrics, based on continuous and/or categorical statistical metrics (HONG et al., 2004; AMITAI et al., 2009; SAPIANO; ARKIN, 2009;

JOYCE; XIE, 2011). To quantify the error between the estimate and the reference and their linear agreement, the following continuous verification statistics are usually adopted: correlation coefficient (COR), mean error (bias), root mean square error (RMSE), and standard deviation (SD). The categorical analyses are based on a 2x2 contingency table (Table 2.1) and defined for the estimate (A) and reference (B) pairs, for a total number of cases N, and considering a minimum threshold (e.g., thr = 0.2 mm h $^{-1}$).

Table 2.1 - Contingency table 2x2 for radar and satellite rainfall (A) evaluations under its rainfall references (B), considering a specific minimum threshold (thr).

	B $\geq$ thr	B <thr
A $\geq$ thr	H	F
A <thr	M	Z

The categorical statistical scores include: *i*) probability of detection (POD), which measures the fraction of precipitation events that are correctly detected by A; *ii*) false alarm ratio (FAR), which gives the fraction of events that were misinterpreted as events; *iii*) success ratio (SR), which is the ratio of hits to the total number of estimated events; *iv*) critical success index (CSI) that measures the fraction of all estimated events that were correctly diagnosed; *v*) and bias score (BIAS), which gives the ratio of the estimated/observed rain pixels (WILKS, 2006; EBERT, 2007). Equations and perfect values of these metrics are listed in Table 2.2.

Continuous and categorical analyses can also be graphically consolidated through the Taylor (TAYLOR, 2001) and Performance (ROEBBER, 2009) diagrams. The Taylor diagram provides a way to summarize how closely a set of patterns matches observations, using COR, RMSE, and SD. In Taylor diagram analysis interpretation, the SD increases with the radial distance from the origin and is normalized by the reference datasets, where 1.0 is the best reference value. Bias values are also included in the Taylor diagram. The performance diagram utilizes the geometric relationship between SR, POD, BIAS, and the CSI to display all four metrics simultaneously, with a perfect forecast lying in the upper right region of the diagram.

Table 2.2 - List of the statistical metrics by continuous and categorical analysis used for performance evaluations *.

Statistic metrics	Equation	Perfect value
Continuous verification statistics:		
Correlation Coefficient (COR)	$COR = \frac{\sum_{i=1}^{N}(A_i-\bar{A}).(B_i-\bar{B})}{\sqrt{\sum_{i=1}^{N}(A_i-\bar{A})^2}.\sqrt{\sum_{i=1}^{N}(B_i-\bar{B})^2}}$	1
Mean error (bias)	$bias = \frac{1}{N}\sum_{i=1}^{N}(A_i - B_i)$	0
Root mean squared error (RMSE)	$RMSE = \sqrt{\frac{1}{N}\sum_{i=1}^{N}(A_i - B_i)^2}$	0
Standard deviation (SD)	$SD = \sqrt{\frac{1}{N-1}\sum_{i=1}^{N}(A_i - B_i)^2}$	0
Categorical verification statistics:		
Probability of detection (POD)	$POD = \frac{H}{H+M}$	1
False alarm ratio (FAR)	$FAR = \frac{F}{H+F}$	0
Success ratio (SR)	$SR = 1 - FAR$	1
Critical success index (CSI)	$CSI = \frac{H}{H+F+M}$	1
Bias score (BIAS)	$BIAS = \frac{POD}{SR}$	1

* Notation: A means the rainfall product under evaluation and B means the reference dataset; N is the total numbers of cases. COR and the categorical scores are dimensionless, bias RMSE and SD are in mm h^{-1}.

In this context, recent studies have investigated the characteristics of satellite rainfall uncertainties and their high spatial and temporal variability for different precipitation rates and over distinct surface types. PetkoviĆ e Kummerow (2015) showed that the GPROF2014 PMW rainfall retrievals provide sufficient sampling and coverage to reproduce the rainfall rate and its accumulation over the central Balkan region during a flood event in 2014. Despite the good agreement between satellite estimates, ground radars and rain gauges, the PMW rainfall estimates significantly underestimate the accumulated rainfall, due the differences between the expected and observed ice-scattering signals. Tang et al. (2016) and Prakash et al. (2016a) evaluated IMERG over Mainland China and India, respectively, and found that its performance depends on the study region, precipitation regime and topography. Even though IMERG outperformed other satellite rainfall products, improvements are still recommended, particularly for regions at high altitudes.

In addition, probability distribution functions (PDFs) of rainfall have been largely used for satellite-based precipitation evaluation (AMITAI et al., 2012; KIRSTETTER et al., 2013; OLIVEIRA et al., 2015; OLIVEIRA et al., 2016). Specifically, PDFs of both occurrence (PDFc) and rain volume (PDFv) can be used to easily identify the occurrence and magnitude of extremes, i.e., light and heavy rain rates (WOLFF; FISHER, 2009). For instance, Kirstetter et al. (2013) investigated differences in various aspects between V7 and the previous version 6 (V6) of the PR 2A25 product, including rainfall rate distributions, systematic biases and random errors. They concluded that V7 is considered superior over land areas due to improvements in the attenuation correction of the radar signal and a recalibrated Z-R equation for use over land areas, as well as a correction for non-uniform beam filling effects. However, despite the improvement in the estimated rainfall rates, especially for the underestimated over land rainfall, V7 still showed an underestimation for high rain rates seen by PDF analysis (SETO et al., 2013; KIRSTETTER et al., 2013; RASMUSSEN et al., 2013), which is associated with non-uniform beam filling effects (IGUCHI et al., 2009).

Recognizing the limitations of pixel-versus-pixel evaluation methods, analogously, various sophisticated methods of verification have been developed over the years, as well as described in Casati et al. (2008). Such methods considering the spatial structure (objects) and the presence of features in forecast fields, and that are specifically designed for high-resolution forecasts (e.g., high-resolution numerical models, radars and satellites).

In this context, several object-based verification methods have recently appeared

in the literature (GILLELAND et al., 2009). Through the method proposed by Davis et al. (2006), Davis et al. (2009), now called Method for Object-Based Diagnostic Evaluation (MODE), it becomes possible to evaluate with more detail the errors and performance of weather forecast models and satellite rainfall estimates, as well as characteristics and evolution of clouds and precipitation, through a three-dimensional grid to point and/or grid to grid, with high spatial and temporal resolutions, by identifying objects in a given field/time. In summary, the MODE tool as part of the Model Evaluation Toolkit (MET) program, from the National Center for Atmospheric Research (NCAR), associates an identification characteristic not only with an intensity threshold application to the field, but also through a convolution procedure, initially through the spatially smoothed fields and then along a defined threshold, also removing certain types of errors that will contaminate the low rainfall values. Once the non-zero contiguous pixels (i.e., characteristics) are identified, they are merged and followed by a fuzzy logic algorithm, using various attributes information (e.g., centroid position, total area, overlapping area, intensity distribution, orientation angle, among others).

Given all those verification approaches (i.e., via traditional, spatial, among others techniques), other studies have been directed to estimate and characterize satellite precipitation uncertainties via error modeling (e.g., Maggioni et al. (2014).

2.3 Error Modeling applied to satellite precipitation

As previously mentioned, the uncertainties in satellite rainfall estimates arise from different factors including the sensor itself, retrieval error, and spatial and temporal sampling, among others (HONG et al., 2006; TANG et al., 2015). However, the uncertainty definition and quantification are directly and indirectly linked to the error model definition (TIAN et al., 2013). An error model is a mathematical description of a truth measure (reference) deviation. The performance and error model parameters can be defined by validation studies and then the model can be used to predict measurements and their associated uncertainties only when surface observations are available as a reference or vice versa, namely inverse calibration (TIAN et al., 2009; TIAN et al., 2013).

In general, two types of error models are commonly used for uncertainties in precipitation measurements (satellite and radar estimates): *i*) the additive error model (e.g., (EBERT et al., 2007; AGHAKOUCHAK et al., 2012) and *ii*) the multiplicative error model (e.g., (HOSSAIN; ANAGNOSTOU, 2006; VILLARINI et al., 2009). However, according to Tian et al. (2013) the multiplicative error model is a much better choice

for better separate the systematic and random errors; applicability to wide range of variability in daily precipitation and to produce superior predictions of the error characteristics.

Therefore, to understand the nature of the error in satellite precipitation products, a technique to decompose the total bias into hit, miss-rain, and false-rain biases can be applied (TIAN et al., 2009). The hit error is then further analyzed based on a multiplicative error model (TANG et al., 2015). Considering this, Maggioni et al. (2014) proposed an error model framework called Precipitation Uncertainties for Satellite Hydrology (PUSH) in order to provide an estimate of the error associated with the high-resolution satellite precipitation products for each grid point and time step. The probability density function (PDF) of the actual rainfall is modeled differently decomposing the error in satellite rainfall estimates in each of the following four steps (of rain and no-rain cases): *i*) correct no-precipitation detection (bothe the satellite and the observation are less than a previously defined minimum threshold), *ii*) missed precipitation (the satellite records a zero, but the reference detects precipitation), *iii*) false alarm (the satellite incorrectly detects precipitation, as the reference observes no rain), and *iv*) hit (both satellite and reference detect precipitation, but they disagree on the amount). The satellite error can be computed by the difference or ratio between the satellite x and the expected value of the estimated precipitation distribution. Thus, the PDF of the actual precipitation y is modeled differently in each of the following four steps depicts in Figure 2.3.

Figure 2.3 - Schematic of the PUSH satellite precipitation error scheme.

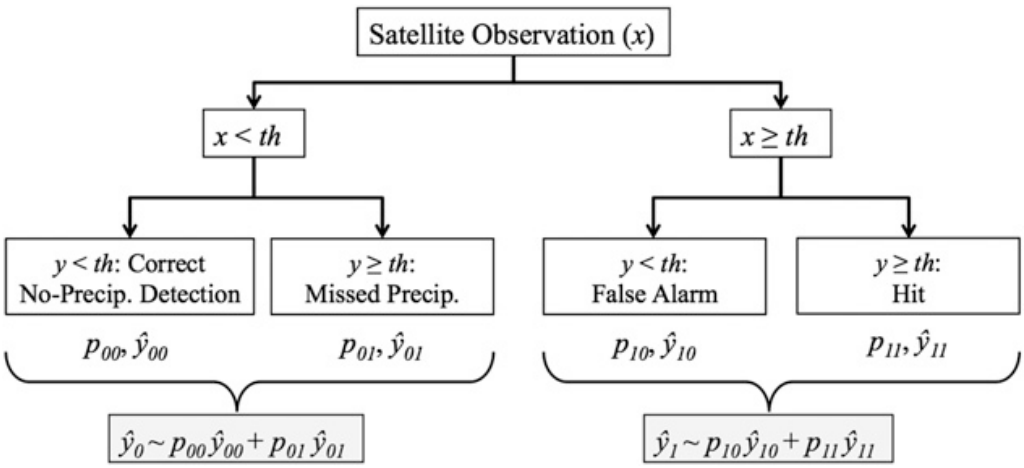

SOURCE: Maggioni et al. (2014)

.

3 EVALUATION OF GPROF-SSMI/S RAINFALL ESTIMATES OVER LAND DURING THE BRAZILIAN CHUVA-VALE CAMPAIGN

3.1 Introduction

The main objective of this chapter is to evaluate the performance of the GPROF algorithm applied to SSMI/S (F16, F17 and F18 satellites) observations for instantaneous rain rates over land. The analyses were performed by comparing with other remote sensing based estimates such as the 2A25-V7 algorithm from TRMM and the X-band CHUVA radar, in the region of the CHUVA-VALE field campaign, in particular in an area within a radius of 60 km and another limited by a 10 ° x 10 ° box from the X-band CHUVA radar location, which is centered at São José dos Campos, SP–Brazil (Southeast Region of Brazil).

The main scientific question that this work seeks to answer is: What are the main characteristics (performance) of GPROF (version 2004) over land rainfall retrievals in representing the different classes of instantaneous rain rates (from light to heavy rainfall) over the Southeast Region of Brazil?

This chapter is organized as follows. In Section 3.2, I briefly describe the study area. Section 3.3 describes the data and methodology used in this study. In Section 3.4, I present the results of the GPROF evaluation obtained for the X-band CHUVA radar and extended areas by comparing with the X-band radar and the PR 2A25-V7 algorithm as reference. Finally, a summary of the main results is presented in the conclusion (Section 5).

3.2 Region of study

The first part of this work is focused on an area covered by the X-band CHUVA radar. This region covers a circle of 60 km radius centered at São José dos Campos (SJC, 23.2 °S, 45.95 °W), specifically at Vale do Paraíba University (UNIVAP). An extended region, delimited by 41 °W–51 °W and 18 °S–28 °S (10 ° x 10 ° box), beyond the X-band CHUVA radar range, was selected in order to obtain the largest number of over land coincident overpasses between the TRMM and F16/F17/F18 satellites. The study period is November 2011 - March 2012 (rainy season) during the CHUVA-VALE campaign. Figure 3.1 shows both regions considered in the present study and the in situ rain gauge network providing, originally, 1 minute rainfall measurements within the X-band CHUVA radar range.

The precipitation over the region is associated with a range of spatiotemporal scales,

ranging from the local to synoptic scale. Local factors such as the sea breeze and topography (such as the Atlantic Ocean and the Mantiqueira and Serra do Mar Mountains) are important local factors capable of intensifying severe weather in this region. Synoptic scale weather systems associated with rainfall such as the South Atlantic Convergence Zone (SACZ), low level jets, and frontal systems, are also responsible for large scale rainfall patterns in this region (HERDIES et al., 2002; CAVALCANTI; KOUSKY, 2003; SATYAMURTY et al., 2008; NASCIMENTO et al., 2016).

Figure 3.1 - Location of the study areas: a) Extended CHUVA-VALE region and b) X-band CHUVA radar area.

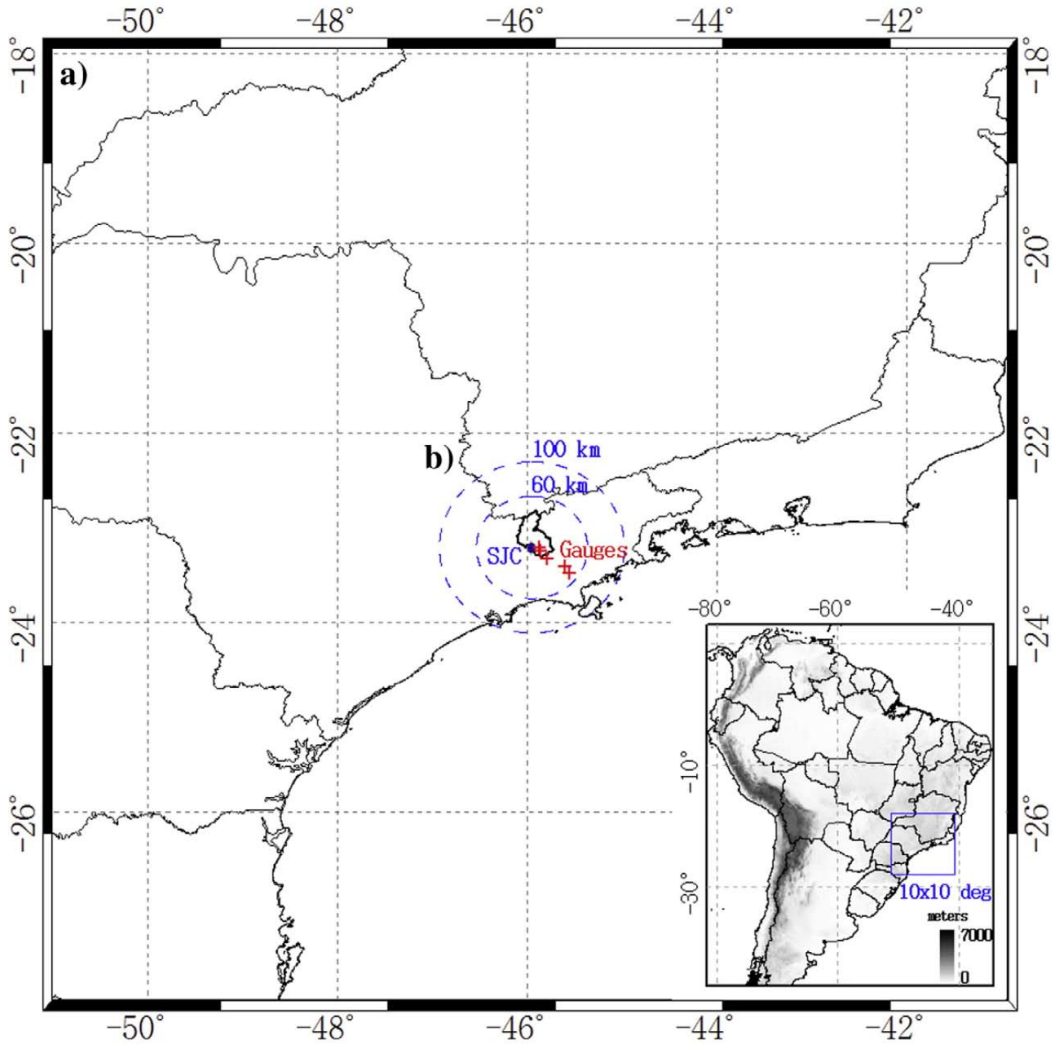

SOURCE: Author's production.

.

3.3 Data and methodology

3.3.1 Data sources

To evaluate the rain rate estimates by GPROF 2004 (SSMI/S version) algorithm over land, two sets of data were used in this study: *i)* rainfall rates from the X-band dual polarization radar from the CHUVA project, named here the X-band CHUVA radar, and *ii)* the near surface TRMM-PR 2A25 version 7 radar rainfall rate product (2A25-V7). A brief description of the datasets used in this study is given as follows:

a) GPROF data

The over land instantaneous rain rates from the Goddard Profiling Algorithm (GPROF) version 2004 (named here GPROF) developed as described by Kummerow et al. (1996) and adapted for SSMI/S (for the F-16, F-17, and F-18 satellites) by Vila et al. (2013) were used in this work. Nevertheless, GPROF version 2004 was originally developed for SSM/I and it was first described by Kummerow et al. (1996). GPROF aims to retrieve the instantaneous rainfall rate and the rainfall vertical structure by using the response functions for different channels peaking at different depths within the raining column. In summary, considering Bayes's theorem, in the present retrieval method the probability of a particular profile R given Tb can be written as:

$$Pr(\mathbf{R}|\mathbf{Tb}) = Pr(\mathbf{R}) \quad x \quad Pr(\mathbf{Tb}|\mathbf{R}) \tag{3.1}$$

where Pr(R) is the probability with which a certain profile R will be observed and is derived using cloud-resolving models (CRM). The second term on the right-hand side of Eq. (1), Pr(Tb | R) is the probability of observing the brightness temperature vector, Tb, given a particular rain profile R. Pr(Tb | R) is obtained using radiative transfer schemes to compute the brightness temperatures corresponding to the CRM output. Together, the radiative transfer and the convolution of these temperatures to the appropriate sensor resolution scheme comprise the forward modeling portion of the retrieval algorithm. Detailed descriptions and information about the retrieval algorithm is available in Kummerow et al. (1996), Kummerow et al. (2001).

It is important to mention that GPROF2004 for SSMI/S uses a histogram matching technique to simulate the brightness temperature (Tb) from seven channels. The approach considers the SSM/I dataset as reference in order to take advantage of the 91 GHz-SSMI/S through the 85 GHz-SSM/I behavior (see Vila et al. (2013)). In the histogram matching process by Vila et al. (2013), the cumulative histogram is computed for each dataset (channel and sensor). For any particular Tbi value

in the data that has to be adjusted, there is a cumulative histogram Tbj value as reference. The input data value of Tbi is then replaced by its corresponding Tbj, running operationally through lookup tables (LUTs).

b) X-band CHUVA radar

In particular, the reflectivity (Z) and rain rate (RRx) variables from the X-band dual polarization weather radar of the CHUVA project (named here the X-band CHUVA radar) for the CHUVA-VALE field campaign were used in this study. X-band radars have been widely used for rainfall estimate purposes. However, the attenuation is larger than for S- and C-band radars (GORGUCCI et al., 2002). To reduce these limitations, the specific differential propagation phase (Kdp) was used instead of the Z-R relation in order to attain more accurate retrievals (GORGUCCI et al., 2002). Moreover, the reflectivity is heavily affected by attenuation of the radome and the rain medium itself (SCHNEEBELI et al., 2012). In order to eliminate cases with wet radome attenuation, data from the radar were only considered when no precipitation was detected by the UNIVAP rain gauge (close to the radar location) within about 3 minutes from the radar scan. In addition, in order to eliminate spurious data (e.g., noise, ground clutter) the horizontal reflectivity and polarimetric variable information was used. In this case, precipitation occurrences were only considered if the reflectivity in the pixel was greater than or equal to 17 dBZ, in order to equalize the minimum reflectivity threshold detectable by the TRMM PR.

As in Braga e Vila (2014), the Constant Altitude Plan Position Indicator (CAPPI) at 2 km, which has a spatial/temporal resolution of 200 meters/6 minutes, was used for the precipitation retrieval. The radar range was limited to 60 km for the X-band radar. To take advantage of the X-band radar polarimetric variables for rainfall estimates for the CHUVA-VALE field campaign, the Dual Polarization Surface Rainfall Intensity (DPSRI) algorithm from Bringi et al. (2007) was used. The DPSRI algorithm, which was originally proposed by Park et al. (2004), uses a combined Z-KDP-R relation for X-band radars, considering the following equations:

$$for \quad Z \geq 35 \quad and \quad Kdp > 0.3 \quad uses \quad RRx = 19.63|Kdp|^{\,0.823} \tag{3.2}$$

otherwise, the follow relation is used (MARSHALL; PALMER, 1948):

$$Z = 200RRx^{\,1.6} \tag{3.3}$$

Here, Z is the horizontal reflectivity (in dBZ), RRx is the radar rain rate (in mm h^{-1}), and Kdp is the specific differential phase (in deg km^{-1}). Large Kdp values (Kdp $>$ 2 deg km^{-1}) suggest the presence of large amounts of liquid water and/or highly oriented (i.e., oblate) shapes. Moreover, Kdp is not impacted by attenuation (unless the signal is completely attenuated) and therefore is an attractive variable to use for attenuation correction and then quantitative precipitation estimation (BRINGI et al., 2007).

The attenuation correction was performed using the Dual-Pol based Attenuation Correction (DPATC) algorithm described in Bringi et al. (2007). The DPATC algorithm performs a reflectivity (dBZ) correction and, if available, another correction on the differential reflectivity (ZDR) data. For dBZ attenuation correction the so-called Rain Profiling Algorithm "ZPHI" (TESTUD et al., 2000) was used. ZPHI (HITSCHFELD; BORDAN, 1954) is an attenuation correction method which basically considers as a constraint the total attenuation through the reflectivity profile Z, deriving it from the total differential Phase data (PhiDP). For the ZDR-Correction the Linear PhiDP method was used. For this latter, the amount of the ZDR correction along the radar range r is proportional to PhiDP:

$$ZDR_{cor}(r) = ZDR(r) + \beta.PhiDP(r) \tag{3.4}$$

where the proportionality factor β is considered equal to 0.035 dB deg^{-1} for X-Band radars (BRINGI et al., 2007).

The performance of the X-band CHUVA radar in quantitatively detecting precipitation, through the DPSRI algorithm, was evaluated by comparing with rain gauge observations. The comparison consists of using the radar pixel values and a mean of the pixels within a radius of 500 meters at the rain gauge locations. Five rain gauge platforms (seen in Figure 3.1) located within the radar coverage area (within a 60 km radius of the X-band CHUVA radar) were considered for this analysis. Given the different measurement methods and distinct temporal resolutions between the X-band CHUVA radar and the rain gauges (i.e., rain gauge: 1 minute and X-band CHUVA radar: 6 minutes), the datasets were integrated hourly (e.g., 00, 01, ..., 23).

Figure 3.2 shows the scatterplots and PDFs of the X-band CHUVA radar hourly rainfall rate estimates versus rainfall rates measured by all five rain gauges within a 60 km radius of the radar location. In general, similar distribution patterns were noted in the X-band CHUVA radar and rain gauges. The X-band CHUVA radar

showed a slight underestimation of precipitation, as we can see in Figure 3.2a. It is important to note that lower frequencies were registered by the radar than by the rain gauges, especially for heavy rains (around 30 mm h^{-1}).

The analysis of the rain gauge station situated at IEAv (Institute for Advanced Studies) (Figure 3.3), which has a more complete time series (from November 1, 2011 to March 31, 2012), produces better results, mainly due to its location (about 10 km from the radar), that falls within the Beam-spreading concept, where the outer bin is much larger than the inner (high-resolution) bin. This directly impacts the CAPPI calculations and consequently the efficiency of rain rate estimates. Fig. 3.3 shows the scatterplot, PDFs, and time series of the instantaneous rain rate from the Xband CHUVA radar versus the IEAv rain gauge. The X-band CHUVA radar tends to slightly overestimate the intensity/frequency of light rains (less than 1.0 mm h^{-1}) and underestimate light to moderate rains (between 1 and 5 mm h^{-1}). The frequency of rains of around 30 mm h^{-1} was correctly captured by the Xband CHUVA radar (Figure 3.3a and b). Good values of COR, RMSE and BIAS of 0.926, 0.399, and 0.006, respectively, were found. It is important to note in Fig. 3c that the X-band CHUVA radar (lower) correctly captured the precipitation occurrence observed by the IEAv rain gauge (upper). The radar also captured in some cases the observed intensities. This can be seen in the highlight box, which shows an example of rain values of around 20 mm h^{-1} observed by both datasets.

c) PR-2A25 (V7) data

The TRMM PR is the first spaceborne rain radar and the only instrument on TRMM that can directly observe vertical distributions of rain, providing 3D reflectivity and 2D rain-rate fields at the ground (over land as well as ocean). The frequency of the TRMM PR is 13.8 GHz (Ku band), which provides high spatial resolution with approximately 4.5 km horizontal and 0.25 km vertical resolution, ranging between 35 °N and 35 °S and with up to two sampling overpasses per day in a given region. On the other hand, PR has a minimum reflectivity threshold of ∼17 dBZ, which limits its ability to detect light rains (e.g., <0.4 mm h^{-1}) (KUMMEROW et al., 1998; IGUCHI et al., 2000).

In general, the rainfall estimates R from the 2A25 algorithm are calculated from the estimated true effective reflectivity factor Ze (calculated using the Ze-R relation), in which the parameters a and b are functions of the both the rain type and the heights of the 0 °C isotherm and storm top. Moreover, the initial values of a and b are modified according to the adjustment in a so that the k–Ze (where k denotes

Figure 3.2 - (a) Scatterplots and quantitative statistics and (b) PDFs of the instantaneous rain rate from X-band CHUVA radar versus rain gauges for CHUVA-VALE field campaign, from Nov 2011–Mar 2012.

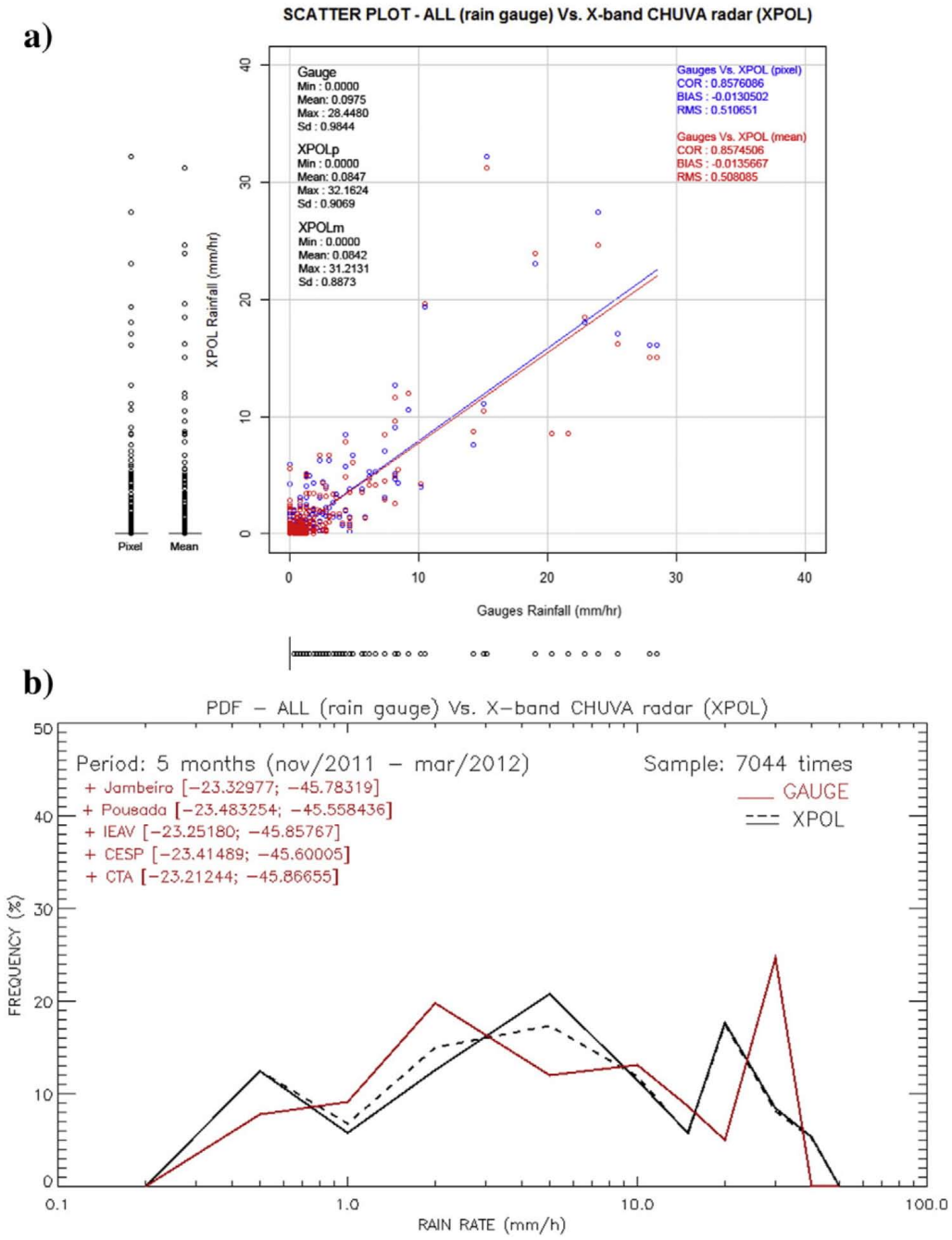

SOURCE: Author's production.

.

Figure 3.3 - (a) Scatterplot, (b) PDFs, and (c) time series of the instantaneous rain rate from the X-band CHUVA radar versus the IEAv rain gauge for the CHUVA-VALE field campaign, from Nov 2011–Mar 2012.

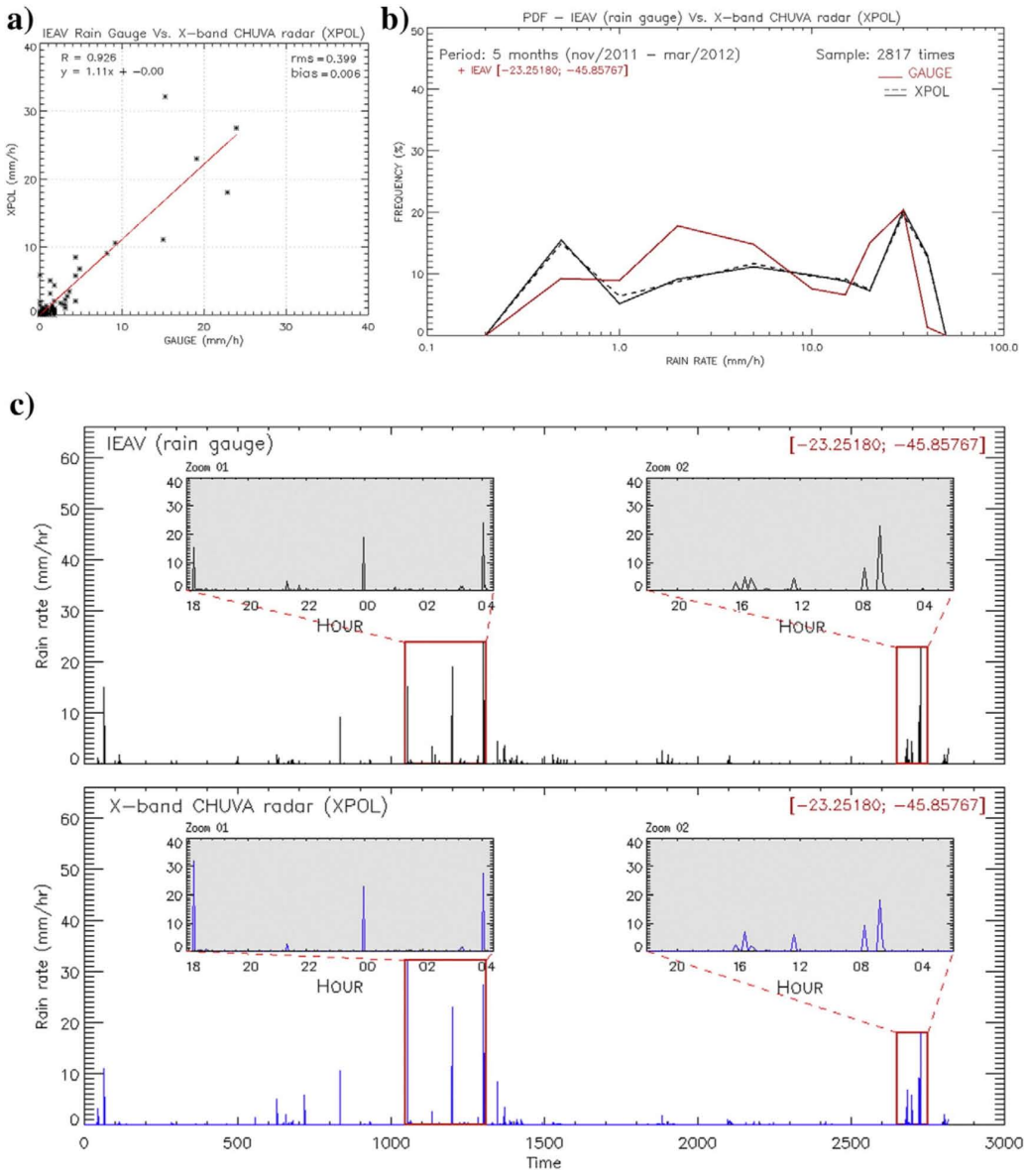

SOURCE: Author's production.

.

the specific attenuation) and Ze–R relations are consistent with the assumed drop size distribution (DSD) model.

Considering the range of variables within the TRMM PR 2A25 algorithm (e.g., *Rain Type*, *Near-Surface Rain* and *Near-Surface Z*, among others), the instantaneous pre-

cipitation is analyzed utilizing the high-spatial-resolution Near-Surface Rain data. The Near-Surface Rain Rate is the rain intensity estimated utilizing the near surface reflectivity assuming a rain drop size distribution (see Iguchi et al. (2000)).

Version 7 (V7) of the PR 2A25 algorithm was used in this work. According to Kirstetter et al. (2013), the major changes between V6 and V7 address the quantitative estimation of rainfall in 2A25 products rather than the detection of rainfall itself. V7 includes improvements in the attenuation correction of the radar signal and a recalibrated Z–R equation for use over land areas, as well as a correction for non-uniform beam-filling effects, reintroduced in the new V7 product. A detailed description of the 2A25 algorithm can be found in Iguchi et al. (2000), Meneghini et al. (2000) and IGUCHI et al. (2009).

3.3.2 Evaluation methods

In order to assess the instantaneous-based rainfall estimation over land, comparisons were made between the X-band CHUVA radar, GPROF rain rate algorithm, and 2A25-V7 near surface precipitation. Two different analyses were performed. The first one evaluates the performance of GPROF over the X-band radar domain (GPROF vs. X-band CHUVA radar). The second analysis is done over the extended region described in the previous paragraph. In this case, GPROF is compared against 2A25-V7 (GPROF vs. 2A25-V7). In order to compare both to ground truth estimates (X-Band radar in the radar domain region and 2A25-V7 for the larger one), it is important to compare the retrieval from the X-band CHUVA radar and 2A25-V7 to assure that the satellite-based radar retrieval accurately represents the instantaneous rain pattern observed by the ground radar. This comparison is done in the X-band radar domain region.

In general, the analysis considers coincident overpasses/timesteps over the same domain, specifically for cases with significant rain occurrence, during the CHUVA-VALE campaign period (Nov. 2011 to Mar. 2012). Given the different temporal-spatial resolutions of the products under study, such as the X-band CHUVA radar with 6 minutes for each 200 meters and the GPROF and 2A25-V7 orbital datasets with up to two sampling overpasses per day in a given region of 12.5 km and $\sim$5 km, respectively, the following procedures were used:

1 For comparisons considering the X-band CHUVA radar as reference, a maximum time interval of 2 minutes was considered and for comparisons considering the 2A25-V7 as reference (GPROF versus 2A25-V7), 5 minutes

was used;

2 The data were resampled to similar spatial resolutions as follows:

i satellite projection: 12.5 and 5 km for GPROF and 2A25-V7 evaluations, respectively, considering the X-band CHUVA radar as reference. A mean of the X-band CHUVA radar pixels inside the satellite (GPROF and 2A25-V7) pixels were calculated. For this, a minimum of 80% of the number of radar pixels with reflectivity greater than or equal to 17 dBz (minimum reflectivity threshold detectable by the TRMM PR, as mentioned before), inside the GPROF and 2A25-V7 pixels, was considered as condition and;

ii regular grid (through bi-linear interpolation): 12.5 km, for GPROF evaluations considering the 2A25-V7 as reference. As in Rozante et al. (2010) for using surface observations and satellite estimates, in this step both the GPROF and 2A25-V7 precipitation estimates were interpolated onto a regular grid using the Barnes objective analysis method, which can be applicable for satellite and conventional data (BARNES, 1973; KOCH et al., 1983). The total numbers of cases and samples are shown in Table 3.1.

Table 3.1 - Number of coincident cases or overpasses and total number of pixels or samples considered in this study for the combination of comparisons between GPROF, X-band CHUVA radar, and 2A25-V7 rainfall products, during the period of the CHUVA-VALE campaign (from Nov. 2011 to Mar. 2012).

	GPROF		2A25-V7	
	No. of cases	Sample	No. of cases	Sample
X-band CHUVA radar	65	1635	17	495
2A25-V7	8	9872		

The ability of GPROF and 2A25-V7 to reproduce the spatial pattern of precipitation was performed using Box & Whisker plot, Probability density function (PDF), scatter plot, and Taylor diagram (TAYLOR, 2001) analyses. The evaluations were made by comparing coincident estimates and reference datasets. In the Taylor diagram analysis, the standard deviation (STD), which increases with the radial distance from the origin, was normalized by the reference datasets (X-band CHUVA radar and/or 2A25-V7), where 1.0 is the proper reference value. Analogous to this, the

quantitative analysis of the algorithms were also conducted from discrete evaluation, through the following statistical parameters: linear correlation (COR), BIAS, probability of detection (POD), false alarm (FAR), Heidke skill score (HSS), and root-mean-square error (RMSE). Equations for the above scores are taken from Wilks (2006), Ebert (2007), Sapiano e Arkin (2009) and Cimini et al. (2013).

Figures 3.4 and 3.5 are examples of cases among those studied with the methodologies employed in the X-band CHUVA radar and extended region domains, respectively. The precipitation products under study in their native spatial resolution (Figs. 4 and 5a–b) and after the interpolation process (Figs. 3.4 and 3.5c–d) are also shown.

Figure 3.4 - Example of instantaneous rain rate (mm h^{-1}) from the X-band CHUVA radar (CAPPI-2km) and its (a) original and (b) satellite projections, and (c) GPROF – satellite projection, for the X-band CHUVA-VALE radar area.

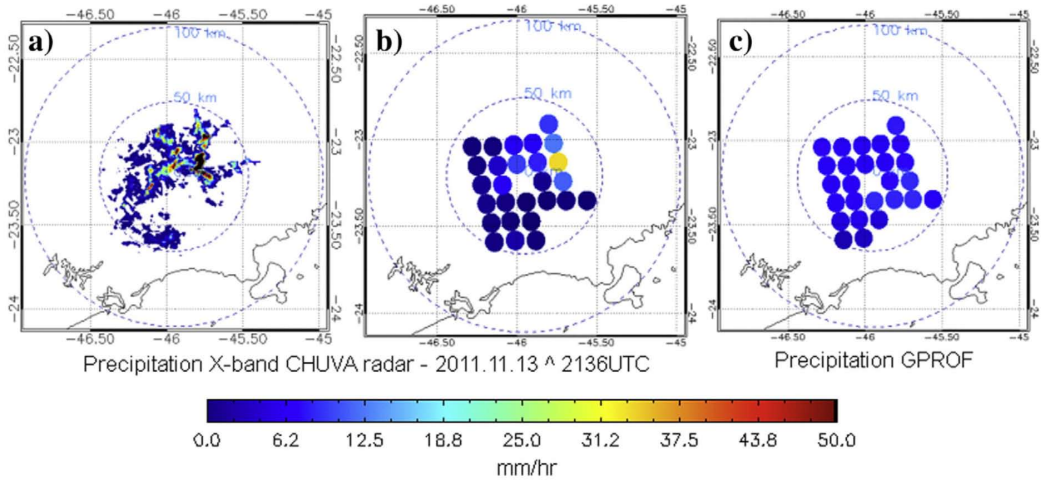

SOURCE: Author's production.

.

3.4 Results

Figure 3.6 shows the scatter plots (mm h^{-1}), box plots (mm h^{-1}), and PDFs (in %) of instantaneous rain rate for the coincident GPROF measurements versus the X-band CHUVA radar reference database. GPROF shows an intensity pattern (Fig. 3.6-a) with a prominent overestimation of weak and moderate rains and underestimation of rainfall above 10 mm h^{-1} compared to X-band CHUVA radar

Figure 3.5 - Example of instantaneous rain rate (mm h^{-1}) from 2A25-V7 (left) and GPROF (right) and its original (a–b) and regular grid interpolated (c–d) data, for the extended CHUVA-VALE campaign region at 0014 UTC on 17 January 2014.

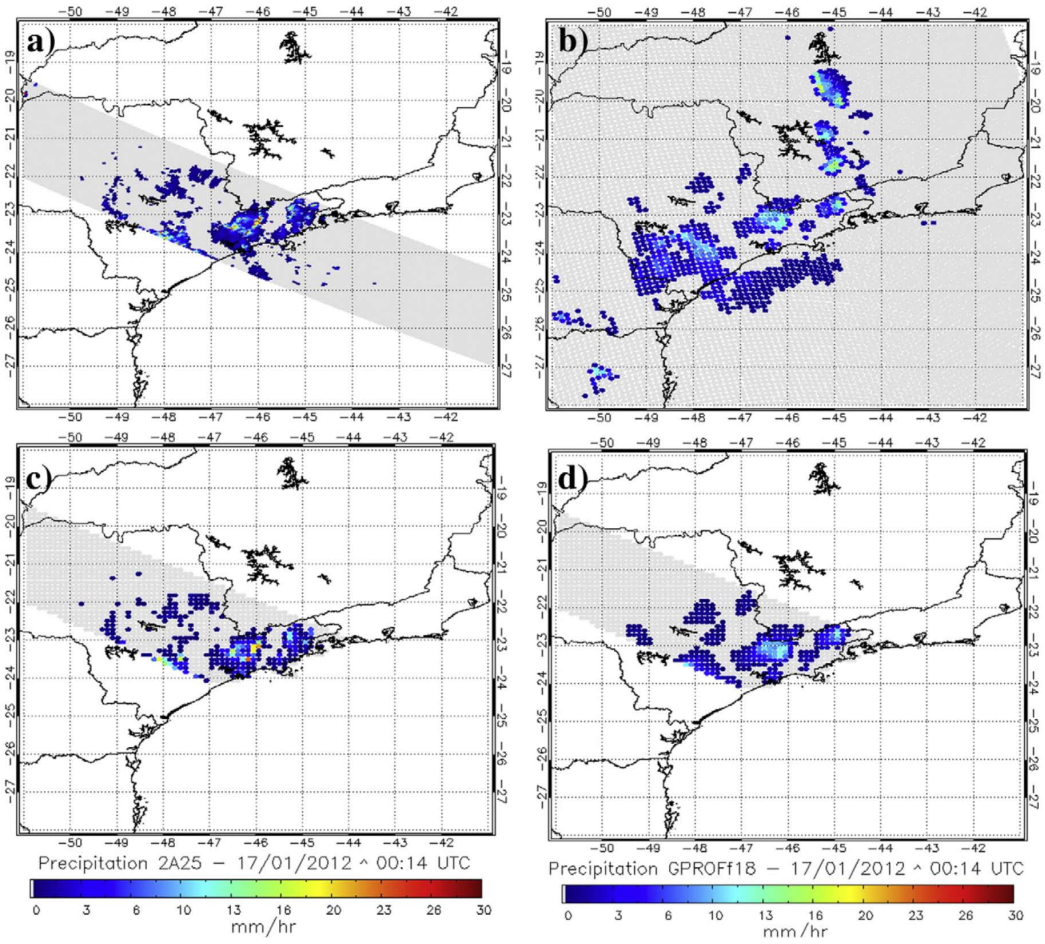

SOURCE: Author's production.

measurements. Through the box plots of rain rate from X-band CHUVA radar in comparison with GPROF (Fig. 3.6-b) measurements, note that the X-band CHUVA radar shows substantially lower 25th, 50th, 75th percentiles, and upper adjacent values than those found in GPROF. The GPROF 25th percentile, median, 75th percentile, and upper adjacent values were around 0.1, 2., 3.5, and 8.4 mm h^{-1}, respectively, whereas the X-band CHUVA radar presented values of approximately 0.5, 1.0, 1.8, and 3.0 mm h^{-1}, respectively. Through the PDF analysis (Fig. 3.6-c), a bimodal distribution was found for the X-band CHUVA radar measurements, similar to Morales et al. (2013), who used DSD measurements from the same study area, which implies significant frequencies of stratiform and convective precipita-

tion. GPROF can not represent very well the frequency of stratiform and convective rains, underestimating precipitation around 1 mm h^{-1} and above 20 mm h^{-1}. On the other hand, the rain frequency was overestimated between 2 to 10 mm h^{-1}, with the maximum difference being 15% around 5 mm h^{-1}.

Table 3.2 presents the statistical parameter (COR, BIAS, POD, FAR, HSS, and RMSE) results of the GPROF validation analysis, considering the X-band CHUVA radar as reference. The COR between both products is 0.4. As a result of the overestimation of light rains, mainly around 5 mm h^{-1} (seen in Fig. 3.6), the BIAS and RMSE presented positive results, with values of approximately 0.7 and 3.5, respectively. The results of GPROF POD, FAR, and HSS, with values of around 0.85, 0.5, and 0.28, respectively, indicate a slight efficiency in detecting the occurrence/non-occurrence of rain events.

Table 3.2 - Statistical evaluation summary for validating the GPROF precipitation measurements considering the X-band CHUVA radar as reference. Here, COR is the linear correlation, the BIAS, POD is the probability of detection, FAR is the false alarm ratio, and RMSE is the root-mean-square error.

Sample: 1635 pixels	COR	BIAS	POD	FAR	HSS	RMSE
GPROF vs. X-band	0.40701	0.70090	0.84628	0.49812	0.28239	3.49177

As in Figure 3.6, Figure 3.7 shows scatter plots, box plots, and PDFs of instantaneous rain rate from the GPROF algorithm considering the 2A25-V7 product as the reference database for an extended region beyond the X-band CHUVA radar range (10 ° x 10 ° box), as previously mentioned. Fig. 3.6-a shows the scatter plot of instantaneous rain rate from the GPROF rainfall estimate versus the 2A25-V7 reference. In general, there is good agreement between both products. Although there is a pattern of general overestimation by GPROF compared with 2A25-V7 (mainly between 0.5 and 8 mm h^{-1}), the GPROF underestimated heavy rains ($>$ 30 mm h^{-1}) relative to 2A25-V7.

Through the box plots of the rain rate between the GPROF and 2A25-V7 time series (Fig. 3.7-b), it is possible to observe that PR 2A25 has a pattern with higher concentrations of light rains, with a 25th, median, and 75th percentiles values of around 0.3, 1.5, and 2.2 mm h^{-1}, respectively. On the other hand, GPROF showed an overestimated distribution pattern of the rain rate over all overpasses in comparison with the 2A25-V7 reference. The GPROF 25th, 50th, and 75th percentiles

Figure 3.6 - Instantaneous rain rate (mm h^{-1}) comparisons between GPROF and the X-band CHUVA radar as reference. a) Scatter plot of X-band CHUVA radar (x-axis) vs. GPROF (y-axis); b) Box & Whisker Plots of X-band CHUVA radar (left) and GPROF (right); here each box represents the 25th, 50th (median), and 75th percentiles, the upper adjacent values (farthest outlying rain rate values that are no more than 1.5 times the interquartile range away from the median), and the outliers (greater than upper adjacent values) of the rain rate measurements and; c) PDF (in %) of the X-band CHUVA radar (red line) and GPROF (black line).

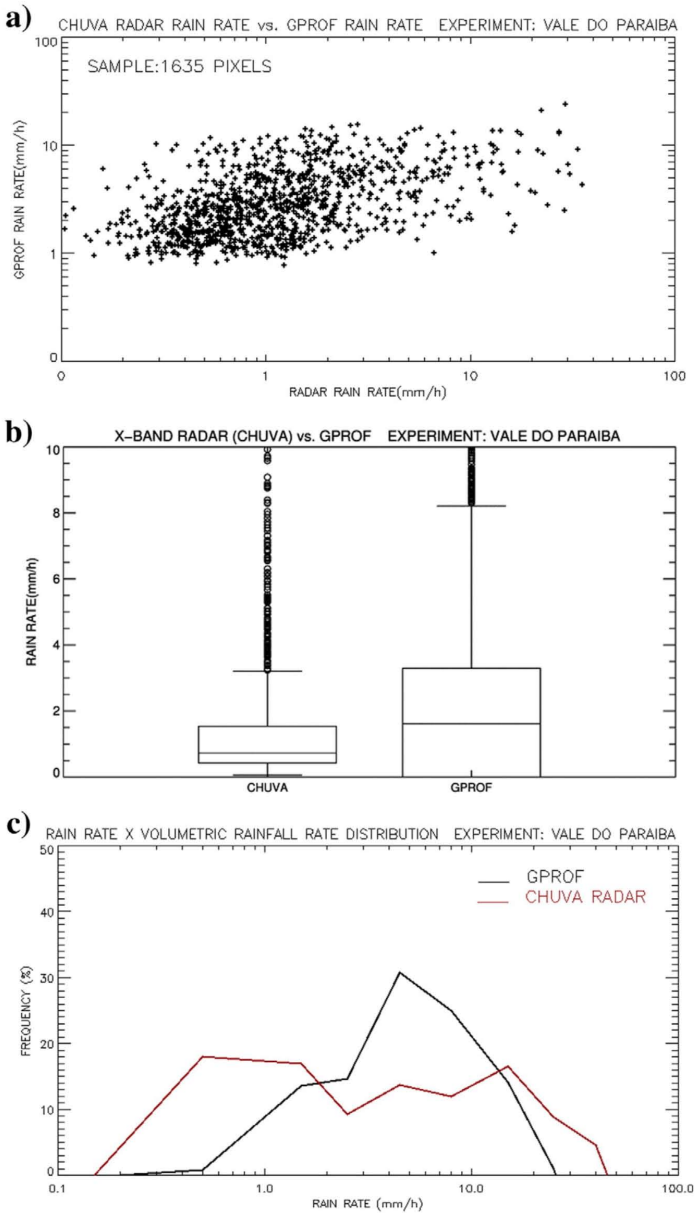

SOURCE: Author's production.

were 0.9, 1.8, and 3.8 mm h^{-1}, respectively. The upper adjacent values ranged from 5 to 8.4 mm h^{-1} from 2A25-V7 and GPROF, respectively.

Fig. 3.7-c shows the PDF (in %) for GPROF and 2A25-V7 over land. When we compared the two rainfall estimate techniques over a larger area, it can be seen that both PDFs have a very similar shape of rainfall distributions, with higher frequencies in the range from 2-8 mm h^{-1}. While GPROF has shown a slight overestimation of moderate rainfall frequencies (between 2 and 10 mm h^{-1}), as well as through the GPROF vs. X-band CHUVA radar PDF comparison (seen in Fig. 3.6-c), an underestimation of stratiform (less than 1.0 mm h^{-1}) and convective (greater than 15 mm h^{-1}) rain frequencies was observed compared to 2A25-V7.

Tables 3.3 and 3.4 summarize the analysis validation results of the GPROF evaluation, considering 2A25-V7 as reference. These statistics reveal a strong spatial variation when considering a larger area. The GPROF BIAS, RMSE, and POD parameters decreased, while FAR and HSS increased. The COR parameter still maintained results around 0.4.

Table 3.3 - Same as Table 3.1, but for GPROF rainfall estimates versus 2A25-V7 precipitation measurements as reference, and for the extended CHUVA-VALE region.

Sample: 9872 pixels	COR	BIAS	POD	FAR	HSS	RMSE
GPROF vs. 2A25-V7	0.41643	0.21676	0.72625	0.54857	0.49501	2.01018

Table 3.4 - Same as Table 3.1, but for 2A25-V7 rainfall estimates versus X-band CHUVA radar as reference.

Sample: 495 pixels	COR	BIAS	POD	FAR	HSS	RMSE
2A25-V7 vs. X-band	0.44244	1.19624	0.92935	0.22273	0.19364	9.50375

In view of the GPROF performance in the comparisons with both 2A25-V7 and X-band CHUVA radar as reference (seen in Figs. 3.6 and 3.7), an evaluation of both databases was performed. The analysis was made in order to assess the performance of the TRMM radar-based retrieval against high-quality ground radar data. Fig. 3.8 shows the comparison between 2A25-V7 and the X-band CHUVA radar ground reference. 2A25-V7 also shows a pattern with overestimation of weak and moderate rains and underestimation of rainfall above 10 mm h^{-1}, compared to X-band CHUVA radar measurements (Fig. 3.8-a). Through the box plot analysis

Figure 3.7 - Same as Figure 3.6, but for GPROF considering 2A25-V7 as reference, and for the extended CHUVA-VALE region over land.

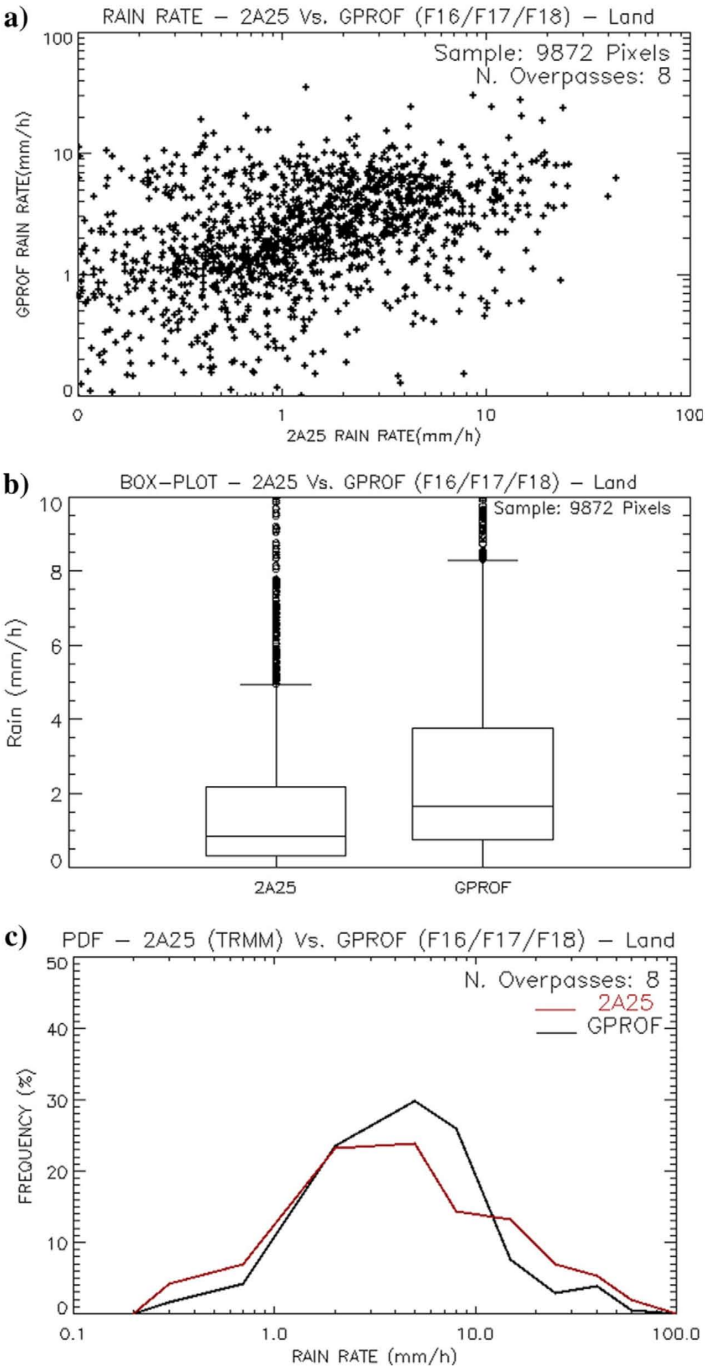

SOURCE: Author's production.

(Fig. 3.8-b), note that 2A25-V7 presented substantially higher 25th, 50th, and 75th percentiles, and upper adjacent values (∼2.0, 3.0, 7.5, and 15.8 mm h^{-1}, respec-

tively), than those computed by X-band CHUVA radar (∼1.0, 1.8, 4.0, and 7.8 mm h^{-1}). Despite the bimodal distribution and with the predominant moderate and heavy rains found by X-band CHUVA radar measurements, an approximate pattern was observed by 2A25-V7 (Fig. 3.8-c). High frequencies of rainfall around 10-20 mm h^{-1} of around 26% and 17% was observed by both 2A25-V7 and the X-band CHUVA radar, respectively. However, the X-band CHUVA radar also showed high frequencies of rainfall around 60 mm h^{-1} (∼18%).

Table 3.4 presents the results of the analysis validation of 2A25-V7, considering the X-band CHUVA radar as reference. The COR between 2A25-V7 and X-band CHUVA radar is 0.44. Good results of 2A25-V7 POD and FAR, with values of 0.93 and 0.22, respectively, were found. On the other hand, the 2A25-V7 BIAS and RMSE presented higher positive results, greater than from GPROF, with values of 1.2 and 9.5, respectively, and a low value of HSS (0.19) was observed.

Figure 3.9 is the Taylor diagram of GPROF estimates versus both the X-band CHUVA radar measurements and 2A25-V7 as reference databases and finally for 2A25-V7 versus the X-band CHUVA radar ground truth. Figure 3.9 summarizes the performances of the different overpasses relative to a reference, by using the linear correlation (COR) and standard deviation (STD) statistical parameters. The presence of two groups with different performance is clearly evident. The first group, with good performance, is clustered close to the reference point, with relatively low RMSE (around 0.75) and showing COR (normalized STD) values ranging from 0.6 to 0.75 (close to 1.0). The second group shows poor performance, with high and scattered values of RMS (greater than 1.25). The COR and normalized STD ranged from 0.2 to 0.5 and 1.5 to 2.0, respectively. Table 5 presents the results of POD and FAR obtained from certain cases with good and poor performance, shown in the Taylor diagram. Mostly, the cases with good performance in the Taylor diagram also showed higher (lower) values of POD (FAR) than the cases with poor performance.

These differences may be associated with the type of precipitation (stratiform and/or convective) that occurred in each analyzed case, and the efficiency of the GPROF algorithm in detecting and quantifying these types of precipitation and/or hydrometeors, which results in larger random errors. The low rain rate values, produced by stratiform rain, justify the good performance of GPROF seen in Taylor diagram (through the COR, normalized STD, and RMSE analyses). On the other hand, through the contingency information in terms of POD and FAR, GPROF fails to

Figure 3.8 - Same as Figure 3.6, but for 2A25-V7 with the X-band CHUVA radar as reference.

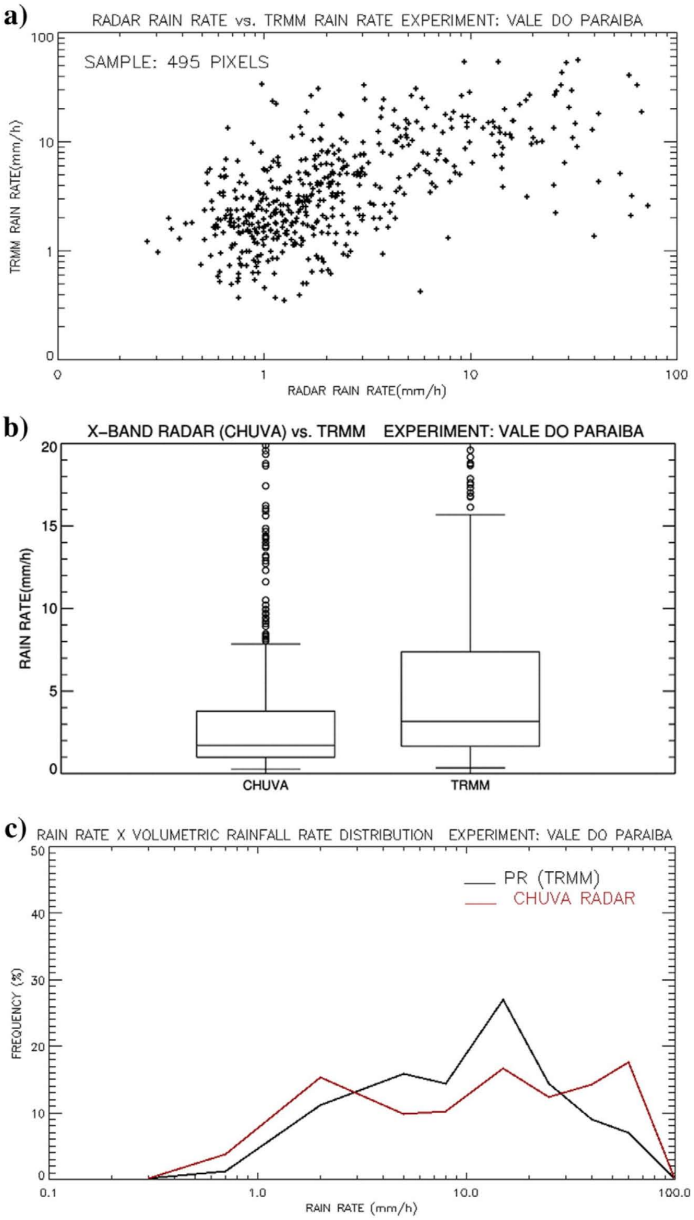

SOURCE: Author's production.

spatially detect such light rains, with relatively low POD and high FAR. This result is consistent with information revealed by the PDFs shown in Figures 3.6 and 3.7, by comparing with both X-band CHUVA radar and 2A25-V7 references, respectively.

It is important to mention that the GPROF approach considers the presence of rain based on ice scattering signatures (e.g., through the 85.5 and 91.6 GHz scattering

Figure 3.9 - Taylor diagram of GPROF (green) and 2A25-V7 (blue) estimates normalized by X-band CHUVA radar as reference and of GPROF (red) considering 2A25-V7 as reference in the extended CHUVA-VALE region.

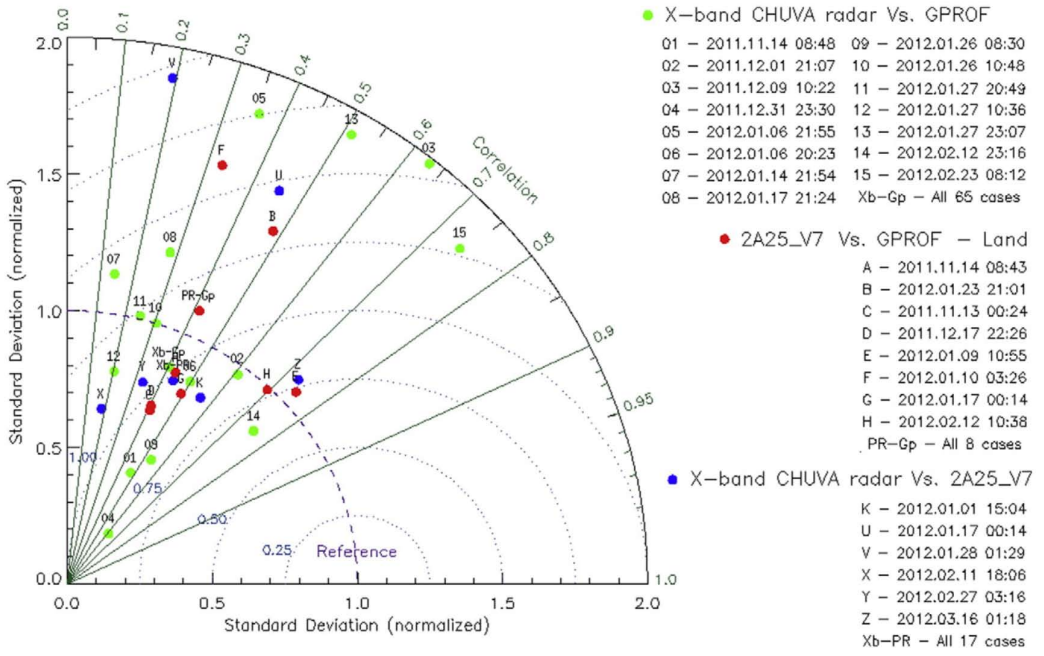

SOURCE: Author's production.

channels), which is dependent on the size/intensity/type of the precipitation system (e.g., mesoscale convective systems) (MOHR; ZIPSER, 1996). In this context, an example for the case H (GPROF vs. 2A25-V7), which showed good performance with high values of COR and low STD and RMSE (seen in Figure 3.9), also had low POD and high FAR (seen in Table 3.5). These results can be analyzed in parallel with Figure 3.10, which shows the spatial distributions of instantaneous rain rate from GPROF and 2A25-V7, brightness temperature from GOES-12 Channel 4 and the cloud classification, such as Warm Rain Cloud, Stratiform, and Convective (AWAKA et al., 1997; SCHUMACHER; JR., 2003), from the 2A25-V7 product over the extended CHUVA-VALE region at 1030 UTC on February 12, 2012. In general, over the entire domain, low rainfall rates (around 1 mm h^{-1}) were observed from both GPROF and 2A25-V7, which were associated with the type of precipitation (stratiform and warm rain clouds) prevailing over the region, with warm brightness temperature (around 240 K).

Table 3.5 - Results of POD and FAR for example cases with good and poor performance as shown in Figure 3.9 (Taylor diagram).

Good cases	POD	FAR
Xb-Gp - 02	1.000	0.111
Xb-Gp - 14	1.000	0.353
PR-Gp - E	0.763	0.491
PR-Gp - H	0.607	0.724
Xb-PR - Z	1.000	0.148

POOR cases	POD	FAR
Xb-Gp - 05	1.000	0.592
Xb-Gp - 13	1.000	0.667
PR-Gp - B	0.710	0.545
PR-Gp - F	0.631	0.473
Xb-PR - U	1.000	0.231

3.5 Conclusions

This chapter evaluates the performance of the GPROF algorithm through the SSMI/S (F16, F17 and F18 satellites) datasets for instantaneous rain rates over land. The analyses were performed by comparing with other remote sensing based estimates such as the 2A25-V7 algorithm from TRMM and the X-band CHUVA radar, in the region of CHUVA-VALE field campaign, in particular in an area within a radius of 60 km and another limited by a 10 ° x 10 ° box from the X-band CHUVA radar location, which is centered at São José dos Campos, SP –Brazil.

The analyses demonstrated that GPROF showed similar rainfall behavior patterns through the comparison with different datasets as reference, in this case, for the X-band CHUVA radar and 2A25-V7. GPROF presented overestimated frequency values, mainly for moderate rainfall (between 2 and 10 mm h^{-1}) and an underestimation of light (weaker than 1 mm h^{-1}) and heavy (heavier than 15 mm h^{-1}) rain frequencies, although not very pronounced when compared to the 2A25-V7 rain reference. It was found that GPROF underestimates mainly the intensity of heavy rains and overestimates the intensities of light and moderate rains, considering both 2A25-V7 and X-band CHUVA radar data references. However, GPROF is slightly better correlated when compared with 2A25-V7 for an extended region than with the X-band CHUVA radar, which may be due the greater coverage area, with more rain no-rain situations in each case. On the other hand, for this reason, the GPROF POD and FAR from the X-band CHUVA radar comparison shows better results

Figure 3.10 - Case example of stratiform rain for the extended CHUVA-VALE region 1030 UTC on February 12, 2012. Instantaneous rain rate (mm h^{-1}) from (a) GPROF and (b) 2A25-V7, (c) brightness temperature (K) from GOES-12 Channel 4, and (d) cloud classification (Warm Rain Cloud, Stratiform, and Convective) from 2A25-V7.

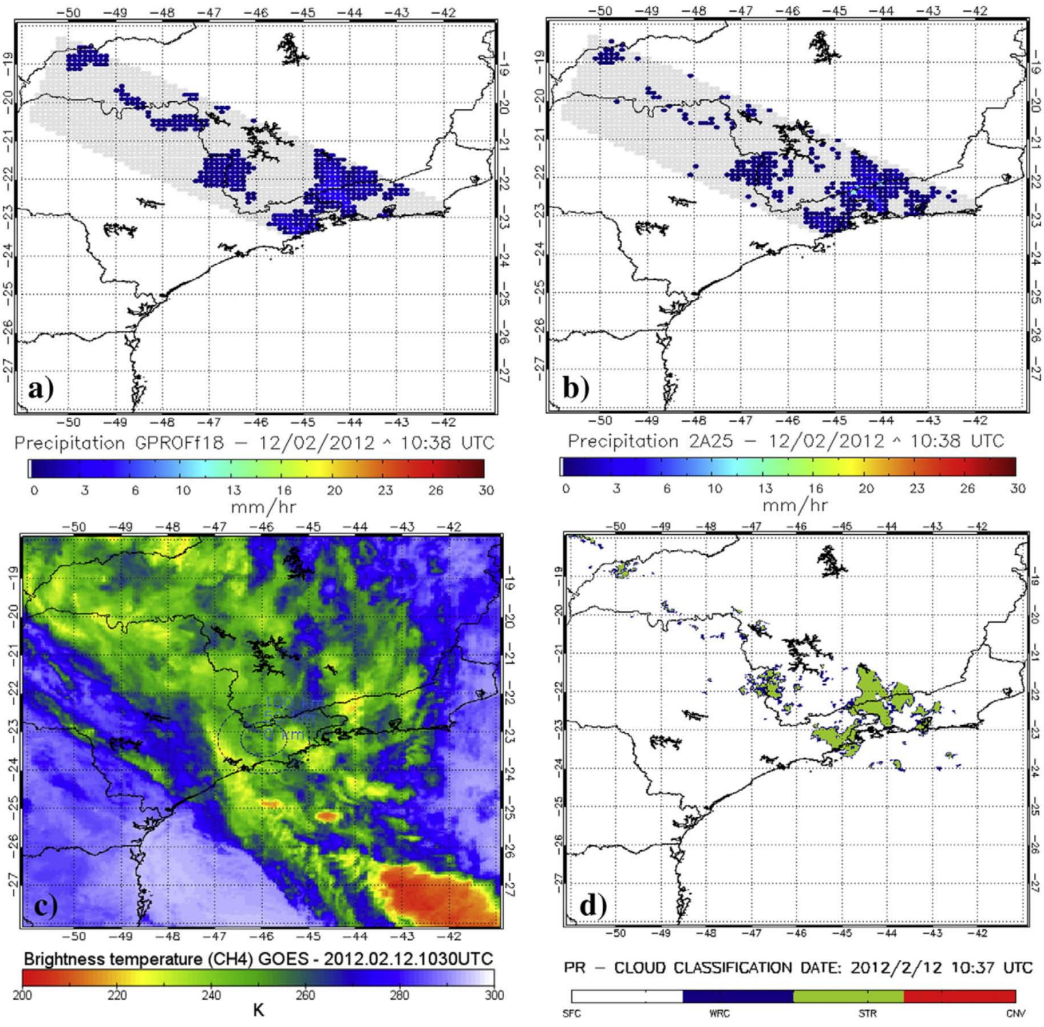

SOURCE: Author's production.

than the GPROF versus 2A25-V7 comparison.

The GPROF2004 algorithm failed to detect some precipitation areas weaker than 2 mm h^{-1}, mainly by comparing with 2A25-V7 over the extended region. In most cases the precipitation was associated with warm rain and stratiform clouds, classified by 2A25-V7. Two groups of performance in Taylor diagram were found: the first (good performance) with low RMSE (∼0.75), high COR (∼0.7), and normalized STD close to 1 and the second (poor performance) showed high RMSE (∼1.5), low COR (∼0.4),

and high values of SDT (normalized). The cases with good performance also showed better POD and FAR results than the cases with poor performance.

This study focused on the GPROF2004 passive microwave (SSMI/S) rainfall retrieval algorithm for land surfaces. Since fewer channels contribute to rainfall retrieval over land (e.g., the 85.5 and 91.6 GHz scattering channels), more careful analysis is needed for these cases, considering with more detail the surface types and their characteristics (e.g., emissivity), in order to minimize error sources of the rainfall retrieved by a passive microwave technique.

4 CHARACTERISTICS AND DIURNAL CYCLE OF GPM RAINFALL ESTIMATES OVER THE CENTRAL AMAZON REGION

4.1 Introduction

The key goal of this chapter is to assess the characteristics of GPM satellite-based precipitation estimates in representing the diurnal cycle over the Brazilian Amazon. The IMERG (V03D, "final" run) precipitation product is evaluated against the S-band SIPAM radar in the proximity of Manaus city, located in the Brazilian Amazon region. The analysis is performed during two seasons (wet and dry) from March–September 2014. Special attention is given to the March and September months (i.e., IOP1 and IOP2), when the GoAmazon and the CHUVA-ACRIDICON field campaigns took place. To better assess the limitations of IMERG, the GPROF2014 PMW rainfall estimates are also analyzed.

The main scientific questions that this work seeks to answer are: (1) How good is the ground-based reference for evaluating satellite precipitation products? (2) How well are the main precipitation patterns over the Manaus region captured by ground-based radars and satellite rainfall products? (3) Is the final IMERG product able to reproduce the diurnal cycle of precipitation over the Manaus region?

This chapter is organized as follows. In Section 4.2, I describe the study region and its precipitation regimes and atmospheric conditions. The datasets and the methodology are also presented in section 4.2. In Section 4.3, I assess the performance of the S-band SIPAM radar, subsequently used as a reference, against the X-band CHUVA radar. In the same section, I present results of the satellite algorithms' (IMERG and GPROF2014) validation, through statistical and diurnal cycle analyses, by focusing on two distinct seasons (wet and dry), using the S-band SIPAM radar as a reference. Finally, a summary of the main results is presented in the Conclusion Section (Section 4.4).

4.2 Study Area, Data and Methodology

4.2.1 Study Area

This work focuses on an area in the middle of the Amazon basin, around the city of Manaus in the state of Amazonas, Brazil. The area covers a circle of 110 km in radius centered at 3.15 °S and 59.99 °W, where the S-band weather radar from the Amazon Protection National System (SIPAM) is located (Figure 4.1). The study period goes from March–September 2014, which includes part of the two GoAmazon/CHUVA

Intensive Operating Periods (IOPs): IOP1 (wet season) from February 1 to March 31, 2014 and IOP2 (dry season) from August 15 to October 15, 2014 (MARTIN et al., 2016). The Aerosol, Cloud, Precipitation, and Radiation Interactions and Dynamics of Convective Cloud Systems (ACRIDICON) campaign was also held during I0P2.

The precipitation pattern over the study region is closely linked to the South American monsoon system (SAMS) (ZHOU; LAU, 1998; VERA et al., 2006; RAIA; CAVALCANTI, 2008), which is related to several factors ranging from the local to the synoptic scale. The first factor is local convection, triggered by forest-pasture contrast, river breezes, topography, and the urban heat island effect (SOUZA; ALVALÁ, 2014; DOSSANTOS et al., 2014; TANAKA et al., 2014). Secondly, mesoscale factors, such as squall lines (COHEN et al., 1995; ALCÂNTARA et al., 2011), although most frequent in the eastern portion of the Amazon basin, penetrate and propagate from the northeastern region to the center of the basin and produce synoptic convective events, which are most common and intense during wet-to-dry and dry-to-wet transitions. Thirdly, the synoptic scale Intertropical Convergence Zone (ITCZ) and the influence of biomass aerosol (GONÇALVES et al., 2015) are the major weather systems/conditions responsible for affecting the rainfall frequencies and intensities and cloud cover (lowest in July and August and highest in February and March). Thus, several precipitation systems and local factors are responsible for modulating the diurnal cycle of precipitation (often leading to late night or early morning precipitation in Manaus) and for controlling the wet-dry seasons in the region around Manaus (MACHADO et al., 2004; ANGELIS et al., 2004).

According to Martin et al. (2016), who used TRMM rainfall estimates (3B42-V7 product) from 2000-2014 over the Amazon basin, the 2014 wet season (IOP1) presented rainfall amounts greater than the fifteen-year mean (∼200 mm) around Manaus, except over the southern region, which presented values between 100 and 150 mm less than the mean accumulated precipitation. On the other hand, spatially-distributed positive and negative anomalies of accumulated precipitation were observed around Manaus during the 2014 dry season (IOP2), when precipitation patterns are mainly associated with local characteristics.

4.2.2 Data Sources

Two GPM rainfall products, Level-3 IMERG and Level-2 GPROF2014, are evaluated over the central Brazilian Amazon, considering the S-band SIPAM weather radar in the city of Manaus as a reference. The S-band SIPAM is evaluated with respect to the X-band dual polarization weather radar from the CHUVA project (X-band

Figure 4.1 - Study area: (a) location and (b) radius of the S-band SIPAM (red) and X-band CHUVA (blue) radars located near the cities of Manaus and Manacapuru. Solid lines represent the radar original coverage. The dashed lines correspond to the areas investigated in the present study.

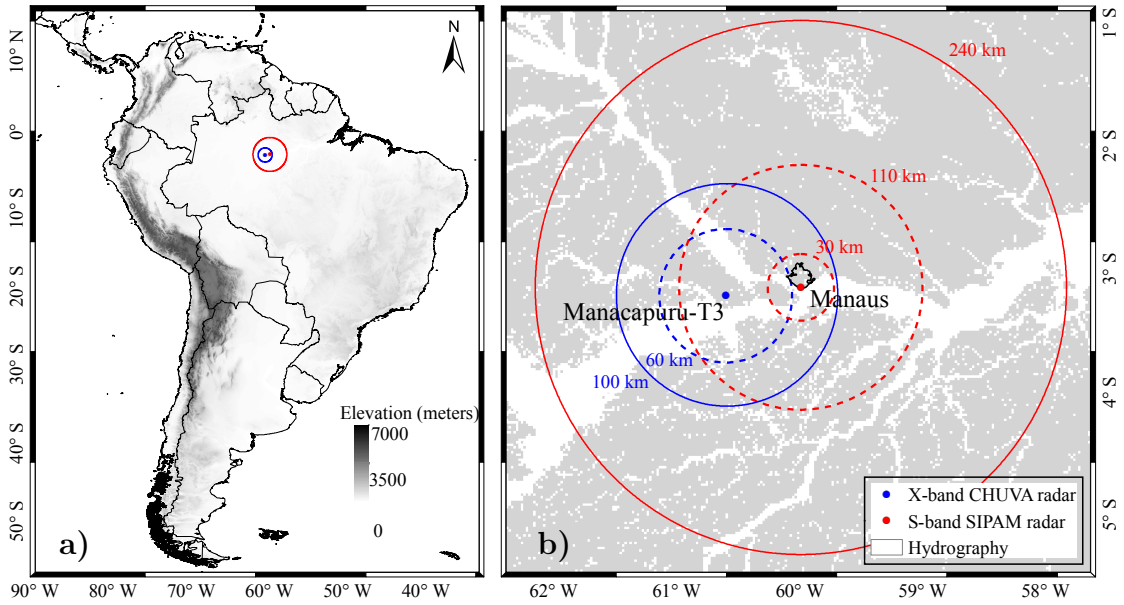

SOURCE: Author's production.

CHUVA radar). A brief description of the datasets used in this study is provided next.

4.2.2.1 Radar Rainfall Estimates

The X-band CHUVA radar takes advantage of polarimetric variables for rainfall estimates based on the Dual Polarization Surface Rainfall Intensity (DPSRI) algorithm (PARK et al., 2004). The DPSRI algorithm uses a combination of reflectivity (Z), specific differential propagation phase (Kdp), and rain rate (R) variables (a Z-Kdp-R relation), for X-band radars at a specific Constant Altitude Plan Position Indicator (CAPPI) level. A detailed description of the precipitation retrievals technique used by the X-band CHUVA radar and its performance in representing surface precipitation compared to rain gauges can be found in Bringi et al. (2007) and Oliveira et al. (2015).

The rainfall estimates from the SIPAM Manaus radar used in this study are processed by Texas A & M University. The rainfall estimates are obtained through the

CAPPI product, based on the 240-km radial dataset. CAPPI products are available for 0.5–20 km of vertical level. The vertical and horizontal resolutions are 500 m and 2 km, respectively. In order to eliminate spurious data (e.g., noise, ground clutter) and improve the quality of the CAPPI products, a correction of the reflectivity field is performed. A calibration constant is applied to the CAPPI files during the following periods: from 9 February 2014 to 27 August 2014 (+2.0 dB), from 28 August 2014 to 16 October 2014 (-3.0 dB) and from 17 October 2014 to 17 August 2015 (-6.0 dB). The calibration constants are derived based on a comparison with TRMM PR data (SCHUMACHER; JR., 2000), providing the 56 dBZ baseline for IOP1, and a study of ground clutter pixels to determine the stability of the radar dataset (SILBERSTEIN et al., 2008). Calibration is determined using base scan information from gridded Plan Position Indicator (PPI) scans.

The rainfall estimates are generated using the radar corrected reflectivity data at the 2.5-km CAPPI level within a radius of 160 km of coverage. A power law relation (Mismo relationship), which was found to be the most appropriate relation for GoAmazon based on comparisons with rain gauge measurements, is used for the conversion of radar reflectivity values to rain rates (Equation 4.1):

$$Z = 178RRx^{1.44} \tag{4.1}$$

where Z is the horizontal reflectivity (in dBZ) and RR is the radar rain rate (in mm h^{-1}). A final radar rainfall product with a spatial/temporal resolution of 2 km/10 min is then provided.

4.2.2.2 Goddard Profiling Algorithm

GPROF is a multichannel physical approach for retrieving both the instantaneous rain rate and the vertical structure information using PMW radiometers on board low-orbiting satellites. GPROF uses a Bayesian statistical approach to retrieve the vertical structure of precipitation over land and ocean and has been developed and enhanced for GPM. GPROF was originally developed for Special Sensor Microwave/Imager (SSM/I), but also applied to the TRMM Microwave Imager (TMI) using the 2A12 algorithm (KUMMEROW et al., 1996; KUMMEROW et al., 2001) and adapted for the Special Sensor Microwave Imager/Sounder (SSMI/S) for the F16, F17, and F18 satellites (VILA et al., 2013).

GPROF aims to retrieve the instantaneous rainfall rate and the rainfall vertical structure by using the response functions in different channels peaking at different

depths within the raining column. According to Bayes' theorem, the probability of a particular rain profile (R) given the brightness temperature vector (Tb) is defined as Equation 4.2:

$$Pr(\mathbf{R}|\mathbf{Tb}) = Pr(\mathbf{R}) \quad x \quad Pr(\mathbf{Tb}|\mathbf{R}) \tag{4.2}$$

where Pr(R) is the probability with which a certain profile R is observed and derived using cloud-resolving models (CRM). The second term on the right-hand side of Equation (2), Pr(Tb | R), is the probability of observing Tb, given a particular rain profile R. This conditional probability is obtained using radiative transfer schemes to compute the brightness temperatures corresponding to the CRM output. Together, the radiative transfer and the convolution of these temperatures to the appropriate sensor resolution scheme comprise the forward modeling portion of the retrieval algorithm. In its current version (2014, Version 1.4), GPROF is applicable to different PMW sensors (imagers and sounders) and scan types (conical and cross-track), such as the SSMI/S sensor on the DMSP(F16/F17/F18) satellites; Advanced Microwave Scanning Radiometer 2 (AMSR2) on board the Global Change Observation Mission-Water 1 (GCOMW1) satellite; GMI on board the GPM core observatory; TMI on board the TRMM satellite; Sondeur Atmosphérique du Profil d'Humidité Intertropicale par Radiométrie (SAPHIR) on board Megha-Tropiques 1 (MT1); the Microwave Humidity Sounder (MHS) on board the European Meteorological Operational A and B (METOP(A/B)) and the NOAA 18 and 19 satellites, as described by Kummerow et al. (2015) and Kidd et al. (2016). The GPROF2014 algorithm Version 1.4, applied to the GPM database (GPM, 2016), is analyzed in this work. Table 4.1 lists some of the basic characteristics of the GPM constellation PMW sensors and the respective satellites that carry them.

Table 4.1 - Characteristics of the passive microwave (PMW) sensors used for the GPROF2014 (Version 1.4) rainfall retrievals *.

Satellite.Sensor	No. of Channels	Frequency (GHz)	Scanning	Sampling (km)
DMSP(F16/F17/F18).SSMI/S	24	19.35 - 183.31	Conical	12.5 x 12.5
GCOMW1.AMSR2	14	7 - 89 V/H	Conical	10 x 7
GPM.GMI	13	10.65V/H, 18.7V/H, 23.8V, 36.5V/H, 89V/H, 165.5V/H, 183.3±3V, 183±7V	Conical	13.4 x 8
TRMM.TMI	9	10.65V/H, 19.35V/H, 21.3V, 37V/H, 85V/H	Conical	13.7 x 6
MT1.SAPHIR	6	183.31±0.2H, 183.31±1.1H, 183.31±2.7H, 183.31±4H, 183.31±6.6H, 183.31±11H	Cross-track	10 x variable
METOP(A/B).MHS	5	89V, 157V, 183.3±1H, 183.3±3H, 190.3V	Cross-track	15.88 x variable
NOAA(18/19).MHS	5	89V, 157V, 183.3±1H, 183.3±3H, 190.3V	Cross-track	15.88 x variable

∗ Acronyms are defined in the text

4.2.2.3 Integrated Multi-SatellitE Retrievals for GPM

IMERG is a Level-3 algorithm that is intended to intercalibrate, merge and interpolate all available PMW estimates of the GPM constellation (e.g., GMI, TMI, SSMIS, AMSR2, and MHS), with PMW-calibrated IR estimates and gauge observations, to produce a quasi-global (60 °N–S) 0.1 ° x 0.1 ° and 30 min dataset, from 1998 to the present (HUFFMAN et al., 2014; HUFFMAN et al., 2015).

Rainfall estimates, initially retrieved by the PMW sensors through the GPROF2014 algorithm, are combined and inter-calibrated with three prior multi-satellite algorithms: (*i*) TRMM Multi-satellite Precipitation Analysis (TMPA) (HUFFMAN et al., 2007; HUFFMAN et al., 2010; HUFFMAN; BOLVIN, 2015), (*ii*) Climate Prediction Center (CPC) Morphing-Kalman Filter Lagrangian time interpolation scheme (CMORPH-KF) (JOYCE et al., 2004; JOYCE; XIE, 2011), and (*iii*) the Precipitation Estimation from Remotely Sensed Information using Artificial Neural Networks-Cloud Classification System re-calibration scheme (PERSIANN-CCS) (HONG et al., 2004). In parallel, CPC assembles the zenith-angle-corrected, intercalibrated "even-odd" geo-IR fields and forwards them to the Precipitation Processing System (PPS) for use in the CMORPH-KF Lagrangian time interpolation scheme and the PERSIANN-CCS computation routines. The PERSIANN-CCS estimates are computed (supported by an asynchronous re-calibration cycle) and sent to the CMORPH-KF Lagrangian time interpolation scheme.

The CMORPH-KF Lagrangian time interpolation (supported by an asynchronous KF weights updating cycle) uses the PMW and IR estimates to create half-hourly estimates. Then, the IMERG "Final" run combines the interpolated observational precipitation data from the Global Precipitation Climatology Center (GPCC) Monitoring Product (currently Version 4) at 1.0 ° spatial resolution. The Level-3 IMERG Final Run (research) product at 0.1 ° x 0.1 ° and half-hourly resolutions, from March to September 2014, is adopted in this study.

4.2.3 Evaluation Methods

4.2.3.1 Radar Rainfall Estimates as Reference

A validation analysis during March 2014 (CHUVA-GoAmazon, IOP1) is performed to assure that those S-band SIPAM radar retrievals accurately represent the instantaneous rain pattern observed over the region and can be used further for satellite evaluations. The S-band SIPAM radar evaluation is performed spatially (pixel-

by-pixel), by comparison with the more accurate radar-based rainfall estimates by the X-band CHUVA radar. The comparison between X-band CHUVA and S-band SIPAM is performed over the X-band CHUVA radar coverage area (60 km radius).

Given the different spatial-temporal resolutions, the X-band CHUVA radar data are resampled from their native 200-m resolution to the S-band SIPAM 2-km spatial resolution. X-band CHUVA radar pixels are averaged within the S-band CHUVA radar pixel. A maximum time interval of 2 minutes between both datasets is considered. A minimum threshold is set to 0.2 mm h^{-1}, and 804 coincident time steps (cases) are analyzed, with a total of 2,173,212 grid points. The S-band SIPAM radar is chosen over the X-band CHUVA radar because of its longer record and larger area. The S-band SIPAM radar is an operational weather radar, which provides real-time monitoring. X-band CHUVA radar is only available during the specific IOPs, and it is limited to 60 km due the attenuation effects.

4.2.3.2 Satellite-Radar Comparison

In order to evaluate the GPM satellite rainfall estimates over Manaus, IMERG and GPROF2014 are compared to the S-band SIPAM radar rainfall estimates, for coincident (spatial and temporal) points during the period from March–September 2014. A radar coverage area of 30–110 km in radius is adopted because of radar physical limitations in detecting signals directly above it ("cone of silence") and far at the constant altitude of 2.5 km. A minimum threshold of 0.2 mm h^{-1} for radar and satellite datasets is used. Considering that IMERG is a half-hourly precipitation product, with the precipitation being an average of all observations in the 30 min range, the S-band SIPAM radar estimates are integrated to the same temporal resolution. Such an integration criterion considers a minimum of 3 time steps of S-band SIPAM radar for a 30 min radar final product. For the GPROF2014-radar comparisons, the native (instantaneous) radar-rainfall estimates are used as a reference, and a maximum time interval of 5 minutes between those datasets is considered. Matching in space is performed by converting the S-band SIPAM radar to the satellite product grid. Given that the total rain amount, the rain area, and/or the PDF shape can be affected by the resampling technique (AMITAI et al., 2009), the mean of the S-band SIPAM radar pixels inside the IMERG and GPROF2014 pixels is computed. Thereby, the original satellite rainfall estimates are preserved in their native spatial/temporal resolutions: (*i*) the IMERG regular grid at 0.1 ° x 0.1 ° half-hourly and (*ii*) the GPROF2014 satellite projection (conical and cross-track) with a spatial resolution varying depending on the sensor (Table 1) and up

to two sampling overpasses per day in a given region. The total number of cases and samples for each product are shown in Table 2.

Table 4.2 - Number of coincident time steps considered for the IMERG and GPROF2014 evaluations against the S-band SIPAM radar over the Manaus region during Intensive Operating Period 1 (IOP1) and IOP2.

		S-Band SIPAM radar					
		IOP1		IOP2		All seven months	
Product		Cases	Sample	Cases	Sample	Cases	Sample
IMERG		826	185850	1324	297900	8578	1930050
GPROF2014	GMI	12(24)	5583	9(30)	3048		
	TMI	13(39)	6479	17(43)	8587		
	F16	***(36)	***	16(42)	3461		
	F17	***(37)	***	***(42)	***		
	F18	9(40)	2600	***(40)	***		
	NOAA18	***(42)	***	22(46)	1740		
	NOAA19	24(44)	1986	23(46)	1803		
	METOPA	19(35)	1648	18(43)	1638		
	METOPB	20(42)	1601	20(45)	1803		
	SAPHIR	38(93)	13445	32(107)	10787		
	GCOMW1	20(38)	18500	21(40)	18954		

*** No satellite sensor overpasses over the study region during the investigated hour intervals; ( ) Total numbers of GPROF2014 overpasses per satellite over the S-band SIPAM radar coverage.

4.2.3.3 Probability Distributions by Rainfall Volumes and Occurrences

In order to study the satellite precipitation error distributions, we looked at volumetric (PDFv) and occurrence (PDFc) probability density function analyses (AMITAI et al., 2009; WOLFF; FISHER, 2009; AMITAI et al., 2012; KIRSTETTER et al., 2013; OLIVEIRA et al., 2015). The PDFv represents the relative contribution of each rain rate bin to the total rainfall volume. Similarly, the PDFc provides the frequency occurrences of each rain rate bin to the total number of occurrences. PDFc normally tends to emphasize lighter rainfall rates, due its high frequency of occurrence. We consider the following precipitation classes: 0.2–0.4, 0.4–0.8, 0.8–1.2, 1.2–1.6, 1.6–2, 2–5, 5–10, 10–20, 20–30, and $\geq$30 (in mm h^{-1}). The analysis is performed monthly from March to September and hourly for both wet (IOP1) and dry (IOP2) seasons over the S-band SIPAM radar coverage.

4.2.3.4 Statistical Analysis

The performance of satellite-based precipitation estimates is evaluated based on continuous and categorical statistical metrics (SAPIANO; ARKIN, 2009; CIMINI et al., 2013). To quantify the error between the estimate (A) and the reference (B) and their linear agreement, the following continuous verification statistics are investigated: correlation coefficient (COR), mean error (bias), root mean square error (RMSE), and standard deviation (SD). On the other hand, the categorical statistical scores include: (*i*) the probability of detection (POD), which measures the fraction of precipitation events that are correctly detected by A; (*ii*) the false alarm ratio (FAR), which gives the fraction of events that were misinterpreted as events; (*iii*) the success ratio (SR), which is the ratio of hits to the total number of estimated events; (*iv*) the critical success index (CSI) that measures the fraction of all estimated events that were correctly diagnosed; and (*v*) the bias score (BIAS), which gives the ratio of the estimated/observed rain pixels (WILKS, 2006; EBERT, 2007). For both the continuous and categorical analyses, a minimum threshold of 0.2 mm h^{-1} for A-B pairs is considered.

Continuous and categorical analyses can be graphically consolidated into the (TAYLOR, 2001) and performance (ROEBBER, 2009) diagrams. The Taylor diagram provides a way to summarize how closely a set of patterns matches observations, using COR, RMSE and SD. In Taylor diagrams, the SD increases with the radial distance from the origin and is normalized by the reference datasets, where 1.0 is the best reference value. In this performance analysis, bias values are also included in the Taylor diagram. The performance diagram utilizes the geometric relationship between SR, POD, BIAS and the CSI to display all four metrics simultaneously, with a perfect forecast lying in the upper right region of the diagram.

4.3 Results and Discussion

In this section, we present and discuss the performance of IMERG and GPROF2014 rainfall algorithms over the Manaus region in the Brazilian Amazon, using the S-band SIPAM radar as a reference. To ensure that the S-band SIPAM radar retrievals accurately represent the instantaneous rain pattern observed over the region, a comparison with the X-band CHUVA radar is performed in Section 4.3.1. The abilities of GPM IMERG and GPROF2014 to reproduce general precipitation characteristics and rainfall diurnal cycles are both analyzed with respect to the S-band SIPAM radar from March–September 2014.

4.3.1 How Good Is Our Reference for Evaluating Satellite Precipitation Products?

Figure 4.2 depicts a density scatterplot of the rain rate for S-band SIPAM radar against the X-band CHUVA radar (coincident area within a 60 km radius of the X-band CHUVA radar location). The corresponding PDFs and cumulative density function (CDFs), both in terms of volumes and occurrences, are also shown for March 2014. X-band CHUVA and S-band SIPAM radars show similar distribution patterns. COR, BIAS, RMS, POD, and FAR recorded values of 0.7, 0.03 mm h $^{-1}$, 0.71 mm h $^{-1}$, 0.75, and 0.38, respectively.

Figure 4.2 - Comparative analysis between S-band SIPAM and X-band CHUVA radars: (a) density scatterplot and (b) probability and cumulative density functions of rainfall volume and occurrences. Note that the x-axis is in log scale.

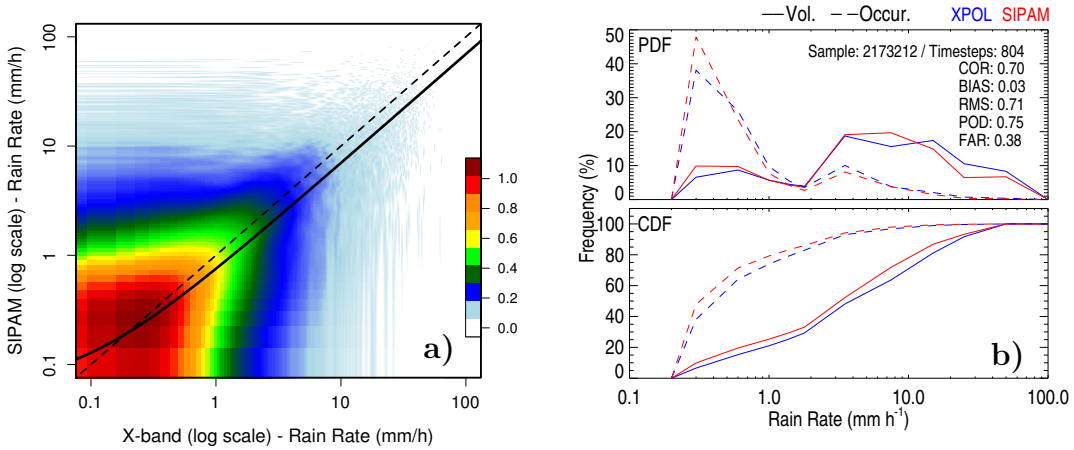

SOURCE: Author's production.

The S-band SIPAM radar presents a slight overestimation of precipitation, mainly for light intensities (between 0.2 and 1 mm h $^{-1}$), which are the most frequent, i.e., high occurrence density (∼45%). On the other hand, an underestimation of heavy rainfall volumes (greater than 10 mm h $^{-1}$) is observed. In terms of CDF distributions, about 76% and 80% of CHUVA and SIPAM rainfall occurrences are from rain intensity <1.0 mm h $^{-1}$ and 96% and 98% from rain intensity <10 mm h $^{-1}$. In terms of volumes, about 20% and 25% (70% and 78%) for rain intensity <1 mm h $^{-1}$ (<10 mm h $^{-1}$) are observed by CHUVA and SIPAM radars. These results demonstrate a good agreement between S-band SIPAM and X-band CHUVA radars, especially for

the more frequent light events. The maximum differences in cumulative frequency between SIPAM and CHUVA occurrence and volume distributions are about 4% from light rain (<5 mm h^{-1}).

In summary, the S-band SIPAM radar shows similar rainfall patterns when compared to the X-band CHUVA radar in terms of PDF/CDF of rain occurrence and volume and is therefore considered suitable to use as a reference for evaluating satellite precipitation products. Specifically, light to heavy rainfall volumes and occurrences are well represented by S-band SIPAM, even though a slight overestimation in the frequency of light rainfall volume/occurrence and an underestimation of heavy rainfall volumes are observed. Such behavior might be related to the fact that S-band SIPAM radar retrieval assumes a constant particle size distribution (see Equation (1)), which may cause a misinterpretation of the correct drop size distribution (DSD) and, consequently, a better quantification of instantaneous rain rate. However, the general pattern of rainfall distribution proved to be consistent in representing the maximum frequencies of occurrence and volume over distinct rainfall classes. A good alternative to investigate this effect is the assumption of more appropriate Z-R relationships for SIPAM rainfall retrievals. Although the X-band CHUVA radar is resampled to the same resolution of S-band SIPAM radar (2 km x 2 km), the accurate physical capability of the X-band radar in capturing smaller and more intense rain cells is limited over distances where attenuation is not major (BRINGI; CHANDRASEKAR, 2001).

4.3.2 Assessment of GPM-Based Products

Figure 4.3 summarizes the monthly performances of IMERG relative to the S-band SIPAM radar, through continuous and categorical analyses using Taylor and performance diagrams over the Manaus region for March–September 2014. Both Taylor and performance diagrams show a seasonal dependence, which is strongly linked to the precipitation regime in the region. The Taylor diagram, which uses a combination of COR, SD, RMSE, and bias parameters to represent the performance of the product compared to the reference, shows an under-performance of IMERG during all months (Fig. 4.3a). A slight wet-to-dry influence in monthly COR is noted, with values ranging from 0.1 (dry) to 0.4 (wet). This wet-to-dry dependence is even more evident in the RMSE, SD and bias, which vary from 1.0 to 2.0, 0.0–2.0, and -0.18–0.15 mm h^{-1}, respectively, going from the wet to the dry season. The wetter (drier) months show higher (lower) RMSE and SD and positive (negative) bias. In the performance diagram, optimal values of SR, POD, BIAS, and CSI score com-

binations lie in the upper right region (Fig. 4.3b). The wetter months present the highest CSI and the lowest FAR compared to drier months, which implies better categorical performance during the wet months, compared to the drier months.

Figure 4.3 - (a) Taylor diagram and (b) performance diagram showing monthly metrics of IMERG (satellite) versus S-band SIPAM radar (reference) from March–September 2014. Color dots indicate different months. On the Taylor diagram, angular axes show COR, whereas radial axes show IMERG SD (the centered RMS difference (solid gray line)) normalized against the reference. The triangle symbol and its direction (up/down) indicate the percent bias (positive/negative). On the performance diagram, dashed lines represent bias scores with labels on the outward extension of the line, while labeled solid contours correspond to critical success index (CSI); the x- and y-axis represent the success ratio (SR) and POD, respectively; and sampling uncertainty is given by the crosshairs.

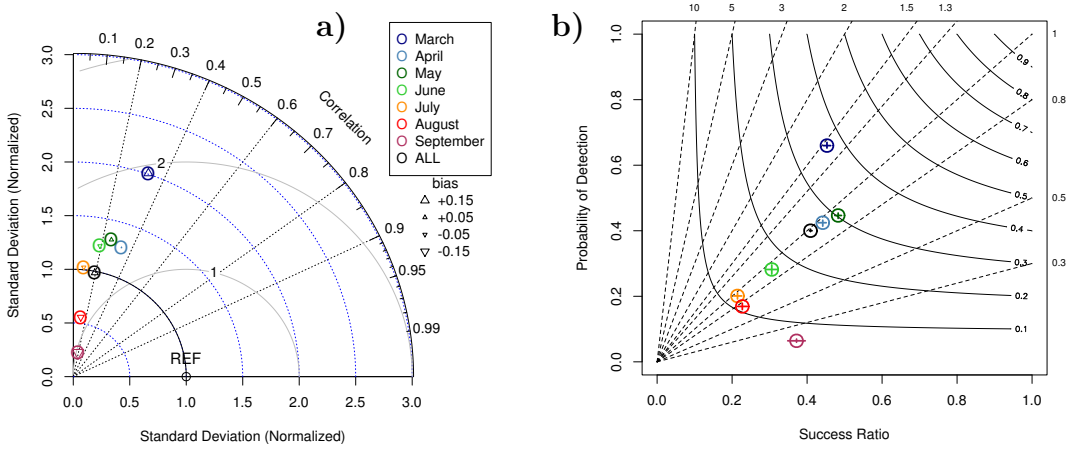

SOURCE: Author's production.

Figure 4.4 depicts monthly PDFs (both PDFv and PDFc) analysis for S-band SIPAM radar and IMERG during March–September 2014. Overall, for both rainfall products, volumes between 5 and 20 mm h $^{-1}$ largely contribute to the total rainfall accumulated during the study period, representing about 20%–35% of the total monthly rainfall. In terms of precipitation occurrences, the largest relative contribution is provided by light rains (<1 mm h $^{-1}$) at around 35%, with events between 2 and 5 mm h $^{-1}$ also largely contributing (∼20%) to the total number of events. Distinct seasonal characteristics are also observed over the Manaus region, especially in the heavy rainfall classes (i.e., >20 mm h $^{-1}$). Drier months are mainly characterized

by volumes of rains above 20 mm h $^{-1}$, whereas wetter months are characterized mainly by events between 5 and 10 mm h-1. The frequency of light (0.2–0.4 mm h $^{-1}$) and heavy (i.e., >20 mm h $^{-1}$) rainfall increases from March–September, while an opposite behavior is observed for moderate rainfall (2–5 mm h $^{-1}$) occurrences.

The shift in heavy rain frequency from wet to dry periods can be explained by the increasing thermodynamic forcing, such as a reduction in the inversion layer and an increase in the convective available potential energy (CAPE) and moisture (MACHADO et al., 2004), which characterizes local and intense convective rain cells in the region. During the wet season, besides higher rainfall amounts influenced by the SAMS life cycle (RAIA; CAVALCANTI, 2008), rain volumes and occurrences are also linked to synoptic/large-scale and mesoscale precipitating systems, e.g., squall lines (COHEN et al., 1995). Thus, the interaction of systems from local to large scales and from wet to dry periods strongly influences the amounts and occurrences of rainfall, through the modulation of the diurnal cycle of precipitation.

Figure 4.4 - Monthly probability density functions of (a) S-band SIPAM radar, (b) IMERG (V03D), and (c) their differences (IMERG-SIPAM) over the Manaus region from March–September 2014 (wet to dry). Upper and lower panels indicate the PDFv and the PDFc distributions, respectively.

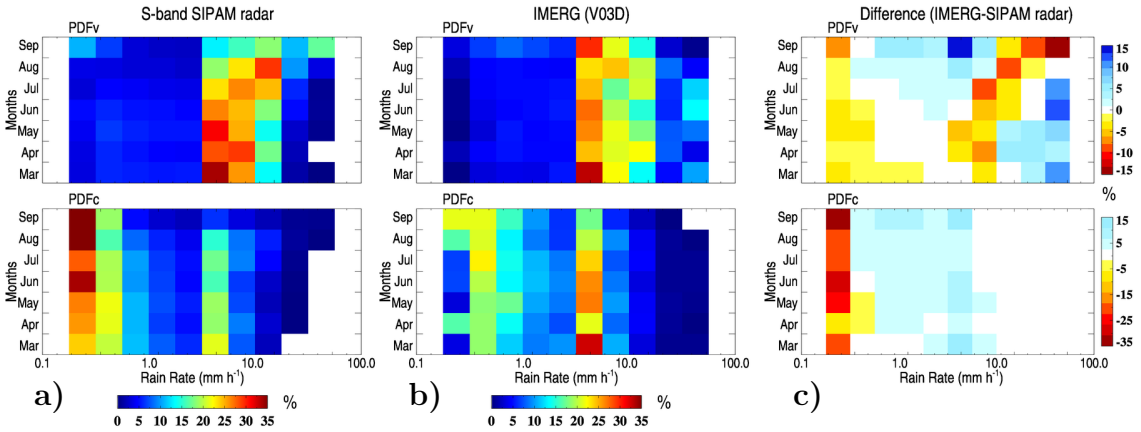

SOURCE: Author's production.

As shown in Figure 4.4, IMERG presents an opposite pattern in PDFv and PDFc distributions compared to S-band SIPAM radar, mainly at moderate and heavy rain rates. During the wet season, IMERG tends to overestimate volumes of moderate and heavy rain rates (>10 mm h $^{-1}$). On the other hand, an underestimation in

the volume frequency of moderate and heavy rainfall classes is observed during the dry period, which is compensated by an overestimation in the frequency of light to moderate rainfall (1–10 mm h^{-1}) volumes. Moreover, IMERG tends to sample less light rain rates than the radar (<1 mm h^{-1} for the wet season and 0.2–0.4 mm h^{-1} for the dry season), showing poor detection of light rain rates (<0.4 mm h^{-1}) and overestimating the 0.4–10 mm h^{-1} rainfall occurrences.

The wet-dry divergence in the IMERG ability of quantifying (PDFv) and detecting (PDFc) heavy rainfall events may be attributed to: (*i*) PMW rainfall incursions through the GPROF2014 algorithm; (*ii*) physical principles associated with the rainfall inference through the IR channel, which relates the cloud top brightness temperatures to the surface rain rate; (*iii*) errors in the integration among the different retrieval algorithms (i.e., TMPA, CMORPH-KF and PERSIANN-CCS) that generate the IMERG dataset; and/or (*iv*) bias adjustment with the GPCC observational data usage.

4.3.3 Precipitation Diurnal and Seasonal Cycles

In this section, we evaluate IMERG's ability to reproduce the diurnal cycle against the S-band SIPAM radar. Figure 4.5a investigates the rain diurnal cycle by looking at the mean and standard deviation (SD) of rain rates for the IOP1 (wet) and IOP2 (dry) periods by the S-band SIPAM radar. Both periods present high rain rates during daytime, which is related to the thermodynamic conditions in the region. During the wet period, the S-band SIPAM radar mean rainfall presents a primary peak of 0.6 mm h^{-1} around 10:00–13:00 UTC, where maximum values of SD (2 mm h^{-1}) are also observed. A secondary SD peak (1.6 mm h^{-1}) at around 00:00 UTC is observed, which might be related to organized mesoscale convective systems over the region.

In the dry period, the S-band SIPAM radar presents peaks of rain rate mean and SD between 15:00 and 21:00 UTC, with values around 1 and 4.5 mm h^{-1}, respectively. Secondary rainfall mean (∼0.4 mm h^{-1}) and SD (∼1.8 mm h^{-1}) peaks are found in the first hours of the day (from 00:00–08:00 UTC). The dry period is also characterized by higher SD than the wet period, which suggests a larger spatial variability of rainy events. During the dry period, local characteristics are more evident, and preferential occurrence locations of convective rain cells are driven by local surface types and thermodynamic conditions (GONÇALVES et al., 2015), which explain the reason for the high mean and SD differences between IOP2 and IOP1.

Figure 4.5 - (a) Diurnal cycles of the hourly mean and standard deviation (in mm h $^{-1}$) of rainfall measured by the S-band SIPAM radar; and (b) box plots of hourly rainfall differences between IMERG (V03D) and S-Band SIPAM radar over the Manaus region during IOP1 (upper panel) and IOP2 (lower panel). The box plots show the median (horizontal bar), 25th and 75th percentiles (lower and upper box bounds), and the maximum and minimum values (horizontal upper and lower lines).

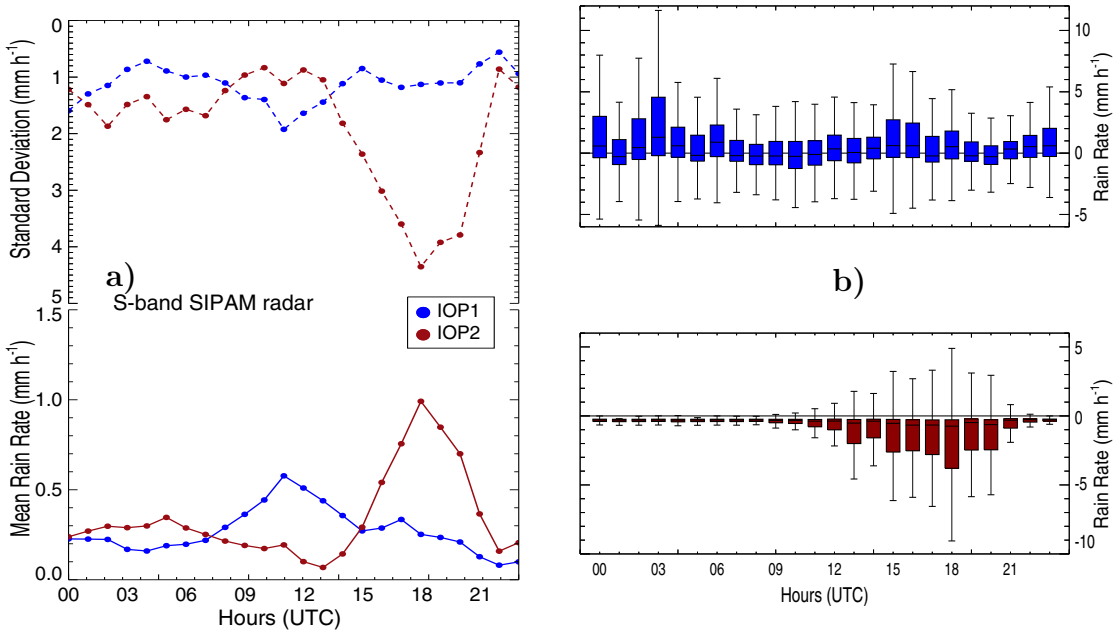

SOURCE: Author's production.

The S-band SIPAM radar mean values and peak hours during the wet (dry) period at 10:00–13:00 UTC (15:00–21:00 UTC) over the Manaus region corroborate the results by Tota et al. (2000), Angelis et al. (2004), Machado et al. (2004), Tanaka et al. (2014). Tota et al. (2000) attributed the maximum frequency around 19:00 UTC (15:00 Local Time) during the dry season to isolated convective activity and the secondary (around 08:00 UTC) to organized mesoscale convective systems. Angelis et al. (2004), Machado et al. (2004), Tanaka et al. (2014) showed that rainfall frequencies and intensities vary over the study region and that primary peaks may change according to surface type (forest, city, among others).

Figure 4.5b shows box plots of rain rate differences (in mm h $^{-1}$) between IMERG and S-band SIPAM radar observations. During the wet season, IMERG presents reasonable agreement with the reference, especially during the peak hour times (between 10:00 and 13:00 UTC), with the median differences close to 0 mm h $^{-1}$, 25th,

and 75th varying from -1 and 1 mm h $^{-1}$ and minimum and maximum values varying from -4 and 4 mm h $^{-1}$. IMERG shows an overestimation between 00:00–04:00 UTC and 15:00–18:00 UTC, especially at 03:00 UTC, which presents the highest values of SD (12 mm h $^{-1}$). On the other hand, IMERG fails to reproduce the diurnal cycle structure during the dry season, showing an underestimation of hourly rainfall and a poor representation of hourly peaks between 13:00 and 21:00 UTC. The IMERG-SIPAM maximum negative differences during the dry period are observed at 18:00 UTC. At this time, which corresponds to the maximum values of rainfall mean and SD observed by the SIPAM radar, large error bounds are observed, which suggests that IMERG is not able to detect the large spatial variability of rainy events in the region.

Figures 4.6 and 4.7, similarly to Figure 4.4, show the PDFv and PDFc distributions, but at the hourly scale and focused on IOP1 and IOP2, respectively. The diurnal cycle main pattern observed by the S-band SIPAM radar reveals distinct PDFv and PDFc distributions between the two periods. During the wet period (Figure 4.6), the rainfall between 5 and 20 mm h $^{-1}$ shows high frequency ($\sim$40% of the total volume). A slight contribution of heavy rainfall (>20 mm h $^{-1}$) around 00:00 and 12:00 UTC in terms of both volumes and occurrences is also observed. During the dry period (Figure 4.7), the contribution of moderate and heavy rainfall (>5 mm h $^{-1}$) volumes/occurrences is more homogeneous than during the wet period. The occurrence of light rain rates is more frequent (>50%) in the dry period than in the wet period, except for 15:00–21:00 UTC, when the occurrence of heavy rain shows high frequencies.

IMERG and the S-band SIPAM radar present similar distribution patterns, with high frequencies (around 40%) of rainfall volumes between 5 and 20 mm h $^{-1}$. However, IMERG tends to underestimate hourly light precipitation intensities and frequencies (between 0.2 and 0.4 mm h $^{-1}$). This corroborates what was observed by Tang et al. (2016) over five distinct regions of mainland China. The positive (negative) biases during the wet (dry) period are mainly due to the overestimation (underestimation) of heavy rainfall volumes. In the wet period, overestimation ($\sim$20%) of heavy rainfall (>20 mm h $^{-1}$) volumes (PDFv) is observed, especially at 00:00–03:00 and 15:00–21:00 UTC, clearly not related to the peak hours observed by the S-band SIPAM radar. In the dry period, the underestimation of rain volume ($\sim$40%) of rainfall greater than 10 mm h $^{-1}$ is recorded during the peak hours, between 13:00 and 21:00 UTC.

Figure 4.6 - Hourly probability density functions of (a) S-band SIPAM radar, (b) IMERG (V03D) and (c) their differences (IMERG-SIPAM radar) during the GoAmazon-CHUVA IOP1 (wet season).

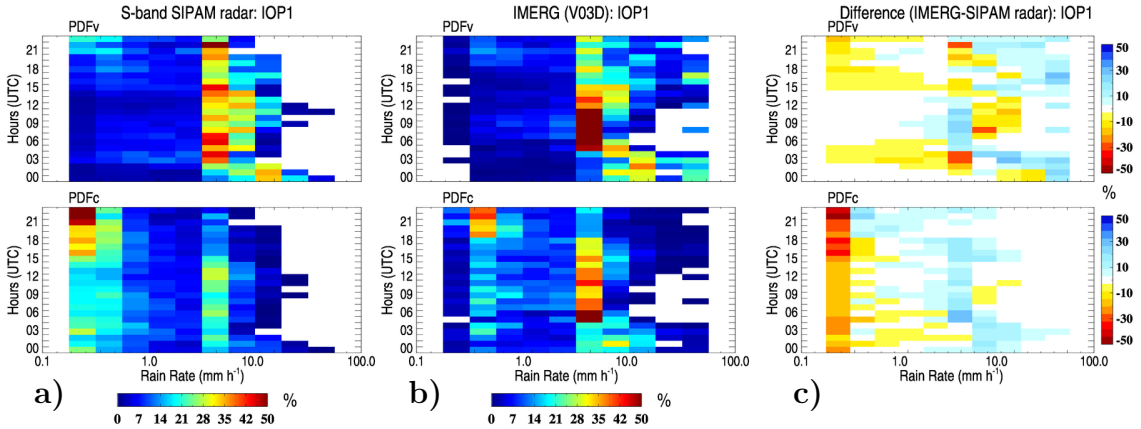

SOURCE: Author's production.

Figure 4.7 - Hourly probability density functions of (a) S-band SIPAM radar, (b) IMERG (V03D), and (c) their differences (IMERG-SIPAM radar) during the GoAmazon/CHUVA-ACRIDICON IOP2 (dry season).

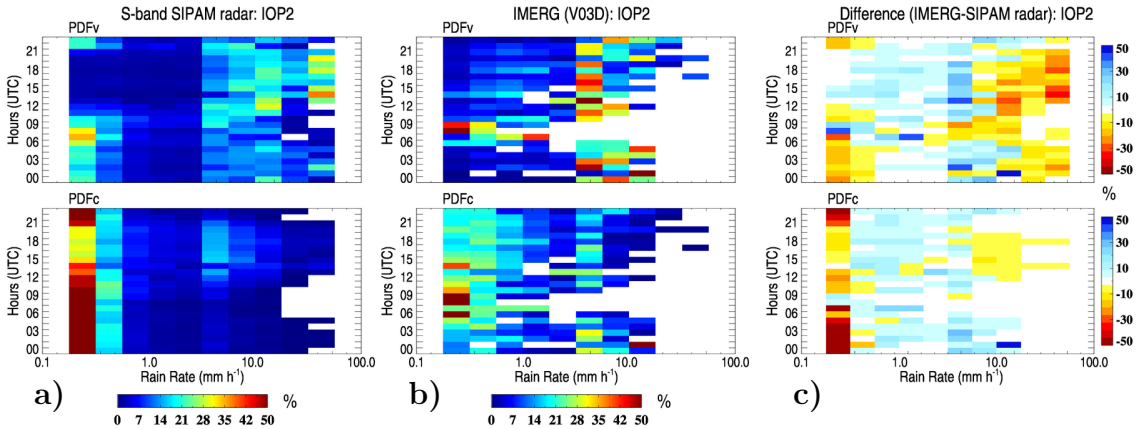

SOURCE: Author's production.

IMERG performance dependence on seasonal and diurnal cycles is particularly evident when the contribution from different rainfall classes is analyzed. During the wet season, precipitation in the Central Amazon is mainly dominated by large-scale systems (e.g., ITCZ and squall lines) and contributes with a high frequency of relatively moderate rainfall ($\sim$5 mm h^{-1}) at any time of the day. IMERG shows a frequency

overestimation during the non-peak hours, which suggests a systematic error. On the other hand, in the dry period, which presents more convective patterns that are concentrated around 18:00 UTC, IMERG shows an underestimation. This may be due to the satellite capability (e.g., spatial resolution) in detecting the presence of intense and localized convective rain cells.

4.3.4 Investigation of Possible Sources of Inaccuracy

In order to investigate the source of IMERG inconsistencies in reproducing the rainfall diurnal cycle, an evaluation of GPROF2014 over the Manaus region is performed. Figure 4.8 shows the hourly overpasses of eleven satellite/sensors (conically and cross-track scanning) in the GPM constellation and used in the GPROF2014 rainfall retrievals over the S-band SIPAM radar coverage during IOP1 and IOP2. Figure 4.8 also shows the times at which IMERG overestimates and underestimates the reference rain rates (shown in Figures 4.5-4.7). Conical and cross-track PMW satellite sensors have a quasi-total daily coverage, with certain preferential hour times by each satellite/sensor at specific times. For example, during the IOP1 and IOP2 (shaded areas), the retrievals are based on the following sensors: SSMI/S from F16 (for IOP2) and F18 (IOP1) satellites; AMSR2 (GCOMW1 satellite); MHS from the METOPA, METOPB, NOAA18 (only in IOP2) and NOAA19 satellites; SAPHIR (MT1); and TMI and GMI from the TRMM and GPM satellites.

Figure 4.8 - GPM satellite/sensors constellation overpasses by GPROF 2014 (Version 1.4) over the Manaus region during the (a) GoAmazon/CHUVA IOP1 and (b) GoAmazon/CHUVA-ACRIDICON IOP2.

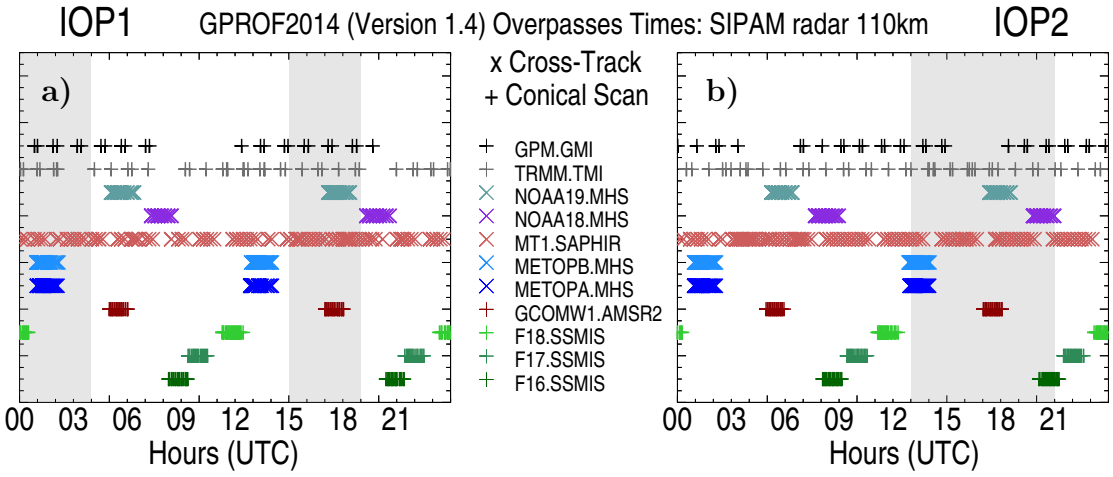

SOURCE: Author's production.

Figure 4.9 depicts the mean characteristics observed through PDFv and PDFc analysis from all of the GPROF2014 sensor/satellite overpasses against its coincident S-band SIPAM radar time steps at 00:00–04:00 and 15:00–19:00 UTC during IOP1 and 13:00–21:00 UTC (IOP2). Overall, GPROF2014 has a good performance in terms of PDFv and PDFc when compared to S-band SIPAM radar measurements. However, GPROF2014 slightly overestimates the volume and occurrence of light (<1 mm h^{-1}) and heavy (>30 mm h^{-1}) rainfall and underestimates moderate rain (around 2 and 10 mm h^{-1}) at 00:00–04:00 and 15:00–19:00 UTC during IOP1. During IOP2 (13:00–21:00 UTC), when a convective PDFv distribution pattern is expected, GPROF2014 strongly underestimates the frequency of heavy rainfall (>20 mm h^{-1}) volumes, up to 20% less than those observed by S-band SIPAM radar. For light rainfall (<1 mm h^{-1}), GPROF2014 shows an overestimation in terms of volume (∼10%), but good agreement with S-band SIPAM radar in terms of occurrences (i.e., PDFc distribution).

Figure 4.9 - Probability density function of rainfall volume (PDFv) and occurrences (PDFc) from GPROF2014 (Version 1.4) over the Manaus region during (a) the GoAmazon/CHUVA IOP1 (during 00–04 UTC and 15–19 UTC) and (b) the GoAmazon/CHUVA-ACRIDICON IOP2 (during 13–21 UTC). The black and gray lines represent the distributions from the S-band SIPAM radar and GPROF2014 algorithm, respectively, while the solid and dashed lines represent the PDFv and PDFc distributions, respectively. The x-axis is in log scale.

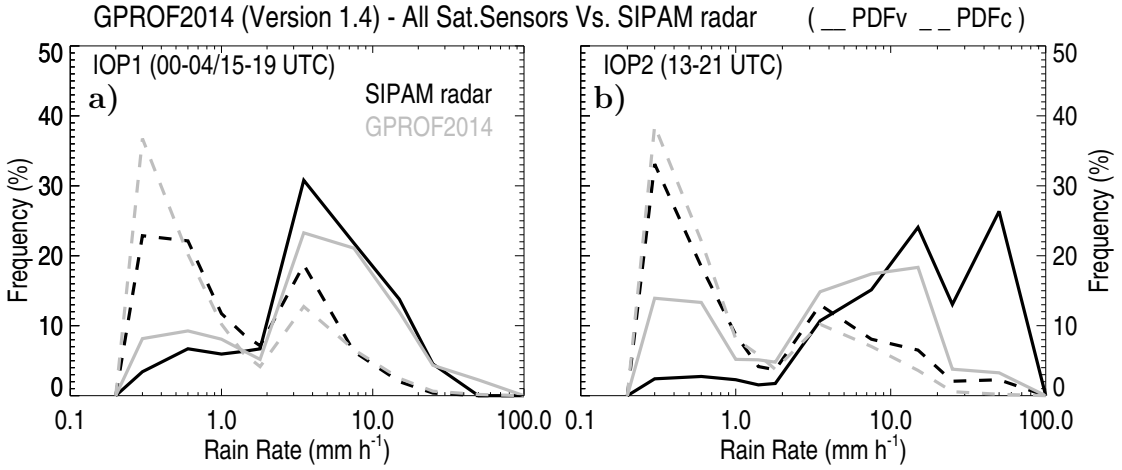

SOURCE: Author's production.

The physical characteristics of the GPROF2014 PMW rainfall retrievals (e.g., sensor-

based spatial resolution, representation of hydrometeors profiles, among others) may be indicated as the main cause of the algorithm limitations. In addition, the surface type factor (i.e., land, ocean, inland water, among others) and their different emissivity signals may also have significant contributions in adopting a particular hydrometeor profile and consequently in the final rainfall retrieval product. Figure 10 shows the GPROF2014 original over land differences, which emphasize the portion of precipitation over the inland water (along the Negro, Solimões and Amazon rivers, near Manaus, Amazonia, Brazil). Figure 4.10 presents differences between each sensor and the S-band SIPAM radar during those times during which IMERG performs poorly. The most prominent GPROF2014 original-overland differences are found during the GPM GMI satellite sensor overpasses. GPROF2014 GMI presents large overestimation (underestimation) of rain rate volume and occurrence greater (less) than 10 mm h^{-1} up to 15%, during IOP1. Large overestimations around 13% in PDFv and ∼15% in PDFc of rain rates between 5 and 10 mm h^{-1} are observed on IOP2. However, an underestimation of light rain rate occurrence frequency is observed by GPROF2014 for the GMI sensor. Evidence of the influence of the Amazon River and the topography in local circulations, cloud cover and, consequently, precipitation in the region, are well reported by observational data, such as radar and rain gauge and also by satellites, e.g., dosSantos et al. (2014), Tanaka et al. (2014), GonÇalves et al. (2015), Machado et al. (2004), Negri et al. (2002). However, such differences in IMERG, for both the wet and dry periods, appear more prominent due to some systematic errors, which can emerge from a non-suitable adjustment linked to the continent-ocean surface type adoption by the GPROF2014 algorithm for GMI sensor.

4.4 Conclusions

In this study, the IMERG (V03D, "final" run) precipitation product is evaluated against the S-band SIPAM radar in the proximity of Manaus city, located in the Brazilian Amazon region. The analysis is performed during two seasons (wet and dry) from March–September 2014. Special attention is given to the March and September months (i.e., IOP1 and IOP2), when the GoAmazon and the CHUVA-ACRIDICON field campaigns took place. To better assess the limitations of IMERG in estimating the diurnal cycle of precipitation, during wet and dry periods, the GPROF2014 PMW rainfall estimates are also analyzed, especially during times when IMERG was not able to correctly quantify and/or detect rainfall.

The main conclusions of this work are:

Figure 4.10 - Differences between the original PDFv (top) and PDFc (bottom) distributions and the over land only GPROF2014 rainfall retrievals over the Manaus region during IOP1 (during 00–04 UTC and 15–19 UTC, left) and IOP2 (during 13–21 UTC, right). Each bar and each line represent the contribution of precipitation over inland water (along the Negro, Solimões and Amazon rivers) for all sensor measurements used in the GPROF2014 algorithm.

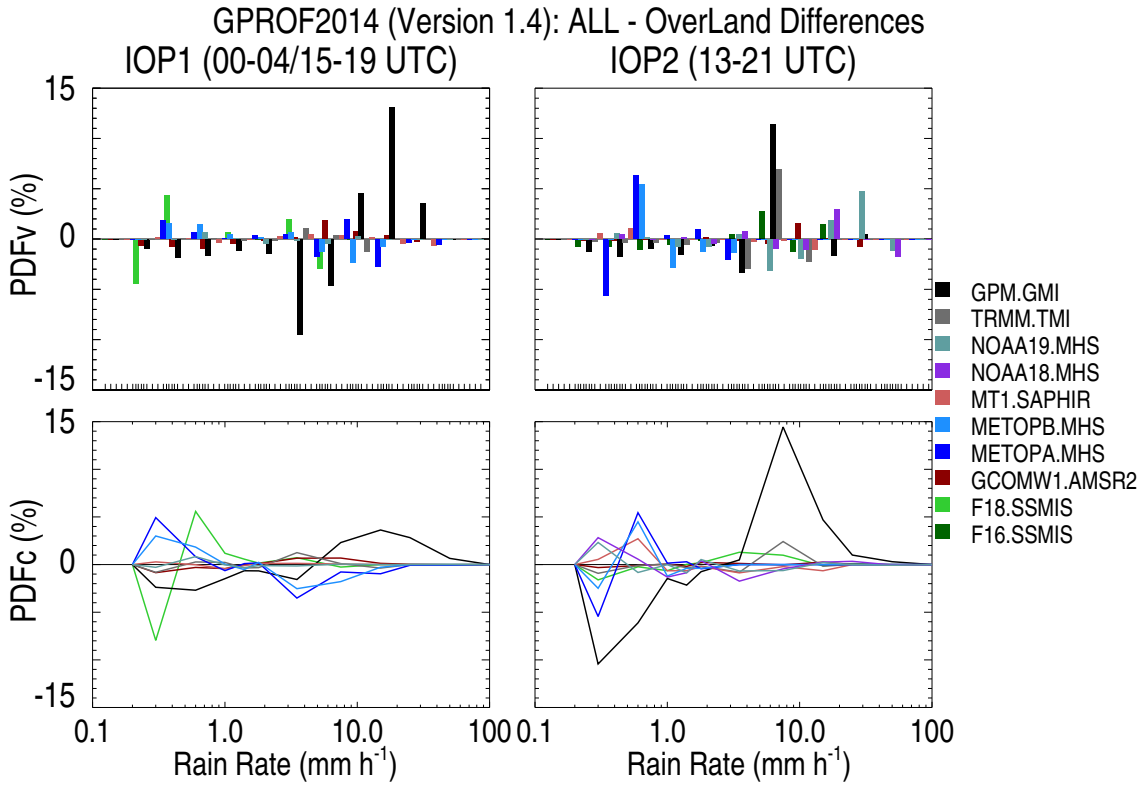

SOURCE: Author's production.

- As an important initial step for further satellite precipitation validation analysis, S-band-SIPAM radar rainfall estimates are validated against another radar-based precipitation (i.e., the X-band dual polarization radar from the CHUVA project). Although a slight overestimation of light rainfall and an underestimation of heavy rainfall are observed in the PDFv and PDFc analysis, SIPAM radar is considered suitable to use as a reference dataset for validating satellite precipitation products.

- S-band SIPAM radar analyses revealed significant wet to dry contrast characteristics over the Manaus region by PDFv and PDFc distributions. During the wetter (drier) period, the volume and occurrence contributions of moderate (heavy) rainfall are clearly identified and strongly modulated by

the diurnal cycle of precipitation.

- Statistical pixel-by-pixel analyses revealed a strong dependence of the IMERG dataset performance on seasonality. The Taylor and Performance diagrams indicate that IMERG performances were directly linked to the monsoonal rainfall pattern over the region. The overestimation (underestimation) of rain volumes is particularly significant for heavy rainfall classes (>10 mm h^{-1}) during IOP1 (IOP2).

- The diurnal cycle analysis during wet and dry periods presented certain times with strong discrepancies between IMERG and the reference. During IOP1, an overestimation between 00:00–04:00 UTC and 15:00–18:00 UTC is observed, due to an overestimation of the occurrence and volume of heavy rainfall. During IOP2, an opposite behavior with strong rainfall volume and occurrence underestimation is found at 13:00–21:00 UTC, mainly due to the non-captured isolated convective rain cells in the afternoon.

- Analysis of the GPROF2014 algorithm rainfall sensor retrievals explains the IMERG's poor performance. GPROF2014 slightly overestimates and strongly underestimates heavy rainfall volume and occurrence, during IOP1 and IOP2, respectively. GPROF2014 for the GMI sensor rainfall retrievals presented the largest impact by inland water surface type, compared to other sensors. Thus, a significant portion of rainfall volumes and occurrences, observed by IMERG, comes from the GPROF2014-GMI rainfall retrievals, most prominent over the inland water surface type, along the Negro, Solimões and Amazon rivers.

This study revealed important information regarding the IMERG and GPROF2014 quality and limitations over the Central Amazon region. This issue was observed along the Negro, Solimões and Amazon rivers, but other regions of the globe and surface types should be deeply investigated. Our findings are critical for the correct and successful applications of GPM rainfall estimates for applications, such as natural disaster monitoring, data assimilation systems, hydrological modeling, climate studies, and for better understanding the physical processes of precipitating systems over the region. These analyses also contribute to improving the GPM algorithm. Future studies should be directed to investigating the characteristics and distributions of uncertainties (systematic and random error components) for both GPROF2014 and IMERG satellite rainfall estimates and exploring other regions in Brazil and beyond.

5 PERFORMANCE OF GPM-LEVEL 2 RAINFALL RETRIEVALS OVER THE BRAZILIAN AMAZON USING TRADITIONAL AND OBJECT-BASED METHODS

5.1 Introduction

This chapter evaluates the performance of GPM-level 2 PMW rainfall retrievals, specifically the GPROF2014 algorithm for TMI and GMI against the more accurate space-based active MW (PR and DPRKu sensors) rainfall retrievals, in reproducing the main characteristics of precipitating systems and its uncertainties over the Brazilian Amazon. The performance evaluations are made via traditional and object-based techniques through Model Evaluation Tools (MET) toolkit.

The main scientific questions that this work seeks to answer are: (1) How is the current performance of GPM's PMW rainfall retrievals (GPROF2014 for TMI and GMI) with regard to satellite-based active MW rainfall retrievals? (2) What are the main physical characteristics of the precipitating systems (e.g. numbers, total area, position distributions, among others) over the Brazilian Amazon through the GPM-level 2 rainfall retrievals?

This chapter is organized as follows. In Section 5.2, I describe the study area and its precipitation regimes and atmospheric conditions. The adopted datasets and the methodology are described in section 5.3. In Section 5.4, results, I initially present the pixel-based evaluations, following the spatial-based verification analysis. In Section 5.5, a summary of the main results is presented.

5.2 Region of study, data, and methodology

This study is focused over an area, of 10 ° x 10 °, in the Brazilian Amazon (55 °W–65 °W and 8 °S–2 °N). Such study area was selected in order to obtain the largest number of coincident TRMM and GPM Core satellite overpasses over the region. This analysis is also made considering its different precipitation regimes along the year, which may impact the performance of GPM Level-2 rainfall retrievals in better detecting and quantifying the precipitating systems over the region. Table 5.1 depicts the numbers of coincident TRMM and GPM satellite overpasses from March to September 2014 over the study area.

This study utilizes four sources of precipitation data from the near–real time GPM constellation of satellites. The data are separated into two main groups: passive and active MW rainfall estimates. The first group are the rainfall rates from the

Table 5.1 - Number of coincident TRMM and GPM satellite overpasses over the study area.

	March	April	May	June	July	August	September
PR-DPR	17	0	8	0	8	4	4
PR-TMI	64	63	65	62	66	63	62
DPR-GMI	23	37	40	37	39	37	38

TRMM and GPM Microwave Imager (TMI and GMI) radiometers in addition to the Goddard PROFiling 2014 (GPROF2014) (Version 2.0) algorithm. The second group consists of the near surface rainfall retrievals from the Precipitation Radar (PR, 2A25 Version 7) and the Dual Precipitation Radar (DPRKu) active microwave sensors on board the TRMM and GPM Core satellites, respectively. A total of 41 coincident overpasses from March to September 2014 are studied. Figure 5.1 shows all the regions considered in the present study and the swaths of the PR and DPRKu active microwave sensors from their correspondent TRMM and GPM satellite overpasses.

The analyses were performed comparing the GPROF2014 algorithm applied to TMI and GMI observations against the PR and DPRKu near surface rainfall products, from their respective TRMM and GPM satellites. Given the different spatial resolutions of the products under study, all the level-2 rainfall retrievals were resampled to similar spatial resolutions. A mean of the pixels inside the regular grid at 0.12 ° x 12 ° resolution were computed.

Two types of analyses for the performance evaluation of GPM-level 2 rainfall estimates from the GPROF2014 against PR and DPRKu are adopted. In the first part, such algorithms are evaluated spatially and temporally using point to point (pixel-based) analysis, considering the use of traditional techniques of verification through categorical events and continuous variables. Such analyses will be conducted by discrete evaluation. Thus, the following continuous verification statistics are investigated: correlation coefficient (COR), mean error (bias), root mean square error (RMSE), and standard deviation (SD). The distribution pattern of rainfall, from light to heavy rain rates, are also assessed through the volumetric (PDFv) and occurrence (PDFc) probability density function analyses (AMITAI et al., 2009; WOLFF; FISHER, 2009; AMITAI et al., 2012; KIRSTETTER et al., 2013; OLIVEIRA et al., 2015; OLIVEIRA et al., 2016).

On the other hand, the categorical statistical scores include: *i*) the probability of de-

Figure 5.1 - Location of the study area. Lines inside each 10x10 degrees grid box (red) represent an example of a single TRMM and GPM satellite overpass over that area. Solid lines represent the swath width from TMI and GMI sensors. The dashed lines correspond to the swath width from the PR and DPRKu sensors.

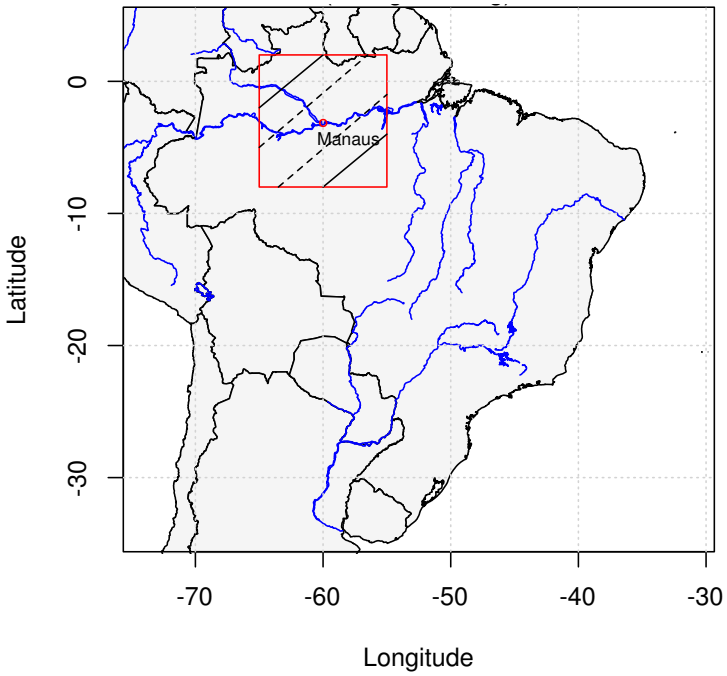

SOURCE: Author's production.

tection (POD), which measures the fraction of precipitation events that are correctly detected by A; *ii*) the false alarm ratio (FAR), which gives the fraction of events that were misinterpreted as events; *iii*) the success ratio (SR), which is the ratio of hits to the total number of estimated events; *iv*) the critical success index (CSI) that measures the fraction of all estimated events that were correctly diagnosed; and *v*) the bias score (BIAS), which gives the ratio of the estimated/observed rain pixels (WILKS, 2006; EBERT, 2007). For both the continuous and categorical analyses, a minimum threshold of 0.2 mm h^{-1} for A-B pairs is considered. Given all these scores, the continuous and categorical analyses were graphically consolidated into the (TAYLOR, 2001) and performance (ROEBBER, 2009) diagrams, respectively.

In the second phase, the evaluation products were made by the spatial verification method through the Method for Object-Based Diagnostic Evaluation (MODE) tool (DAVIS et al., 2006; DAVIS et al., 2009). Through the complete time series under study (from March-September 2014), as well as the selected significant cases, the following

attributes from the MODE method are obtained and evaluated: total number of single objects (matched and unmatched), total number of cluster objects, total area of objects, cluster pair centroid distance (minimum, 1st quartile, median, mean, 3rd quartile, and maximum), cluster pair centroid displacement (minimum, 1st quartile, median, mean, 3rd quartile and maximum), and the symmetric difference. The symmetric difference is the total non-overlap area between the matched objects, shaded in gray (smaller is better). The centroid distance is the difference between the two centroids of the matched objects. The centroid displacement examines the x (nominally east–west) and y (nominally north–south) offsets of the centroids of two matched objects (WOLFF et al., 2014).

However, as a preliminary step, to assure that the satellite-based radar retrievals from PR and DPRKu sensors accurately represent the instantaneous rain pattern, given that these retrievals come from the same measurement principle, it is important to compare the near surface rainfall retrievals from the 2A25-V7 and DPRKu algorithms over the study domains. The comparison are made over the complete Brazilian domain (30 °W–75 °W and 35 °S–5 °N), centered at Manaus city. Figure 5.2 depicts the scatterplot and the corresponding PDFs, both in terms of volumes (PDFv) and occurrences (PDFc) of the near-surface rain variables for TRMM PR (2A25-V7 algorithm) against the GPM DPR (Ku band) over the Brazilian domain. The rainfall retrievals show similar distribution patterns. Despite the relatively low COR (∼0.7), the different classes of rainfall, from light to heavy rainfall, are well represented in terms of volume and occurrence, which shows higher volume contribution of rainfall around 10 mm h^{-1}. The POD and FAR recorded values of ∼0.85 and ∼0.18, suggesting that events were correctly detected in both active-based rainfall retrievals.

5.3 Results

5.3.1 Pixel-based evaluations

Figures 5.3 and 5.4 show the scatter plots (upper panels) and the PDFs of volume and occurrence (in %) (lower panels) of the rain rate (in mm h^{-1}) for the TRMM PR versus GPROF2014 (TMI) and the GPM DPR (Ku band) versus GPROF2014 (GMI), respectively, over the 10 ° x 10 ° Brazilian Amazon area. A summary of statistical indicators, such as COR, bias, RMS, POD, and FAR, are also included in Figures 5.3 and 5.4.

GPROF2014 for both the TMI and GMI sensors presented good agreement in com-

Figure 5.2 - Comparative analysis between TRMM PR and GPM DPR(ku) near surface rainfall retrievals: (a) scatterplot and (b) probability density functions of rainfall volume and occurrences. Note that the rain rate distributions at y- and x-axis are in log scale.

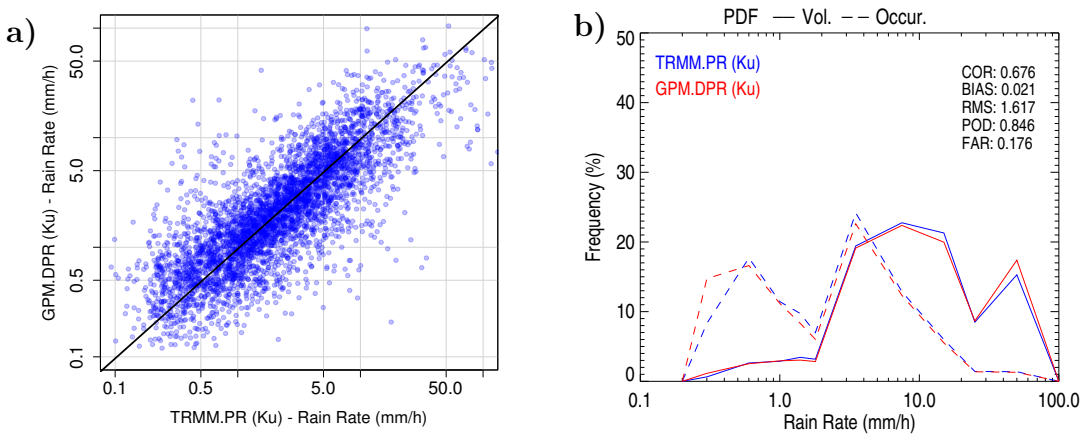

SOURCE: Author's production.

parison with the TRMM PR and GPM DPR rainfall retrievals. An intensity pattern with a prominent underestimation of heavy rainfall (>30 mm h^{-1}) and overestimation of moderate rainfall, around 10 mm h^{-1}, were observed during the study period. An underestimation in the occurrence and volume of light rainfall were observed. Those results are in agreement with those obtained for Southeastern Brazil through GPROF2004 for SSMI/S during the CHUVA-VALE campaign (OLIVEIRA et al., 2015). The authors suggest that the performance is intrinsically linked to the convective-stratiform rainfall occurrences over the study region. On the other hand, over the Manaus region, Oliveira et al. (2016) observed that GPROF2014 (Version 1.4) tends to include non realistic values of rainfall over the river, which in fact are corrected for this version used in this study (Version 2.0), as well observed through the PDFv and PDFc in Figures 5.3 and 5.4.

Figure 5.3 - Monthly (from March-September, 2014) scatterplots (upper panels) and PDFv and PDFc (lower panels) of the rainfall estimates between TRMM PR and GPROF2014 (GMI) rainfall products. Note that the rain rate distributions at y- and x-axis are in log scale.

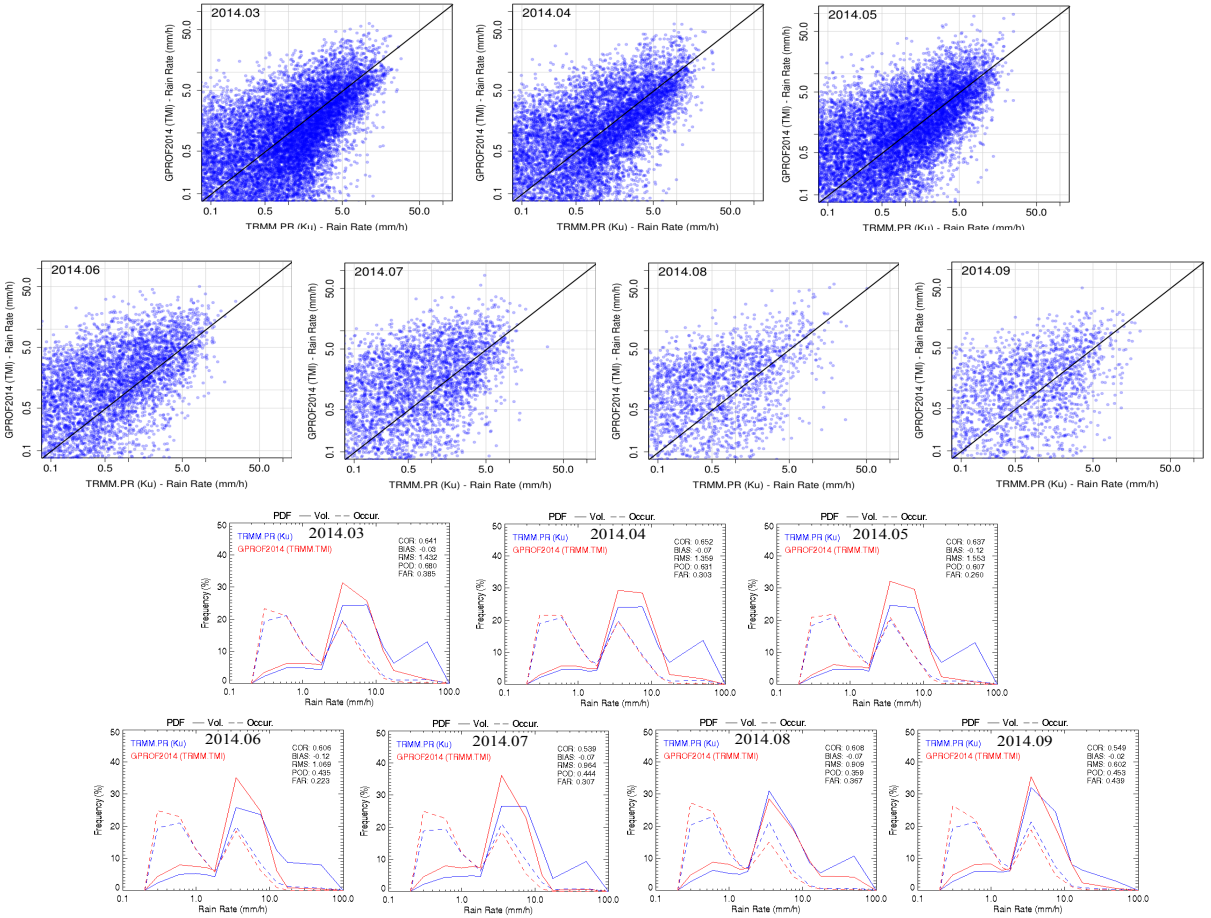

SOURCE: Author's production.

Figure 5.4 - As Fig. 5.3, but for the DPR and GPROF2014(GMI) rainfall retrievals.

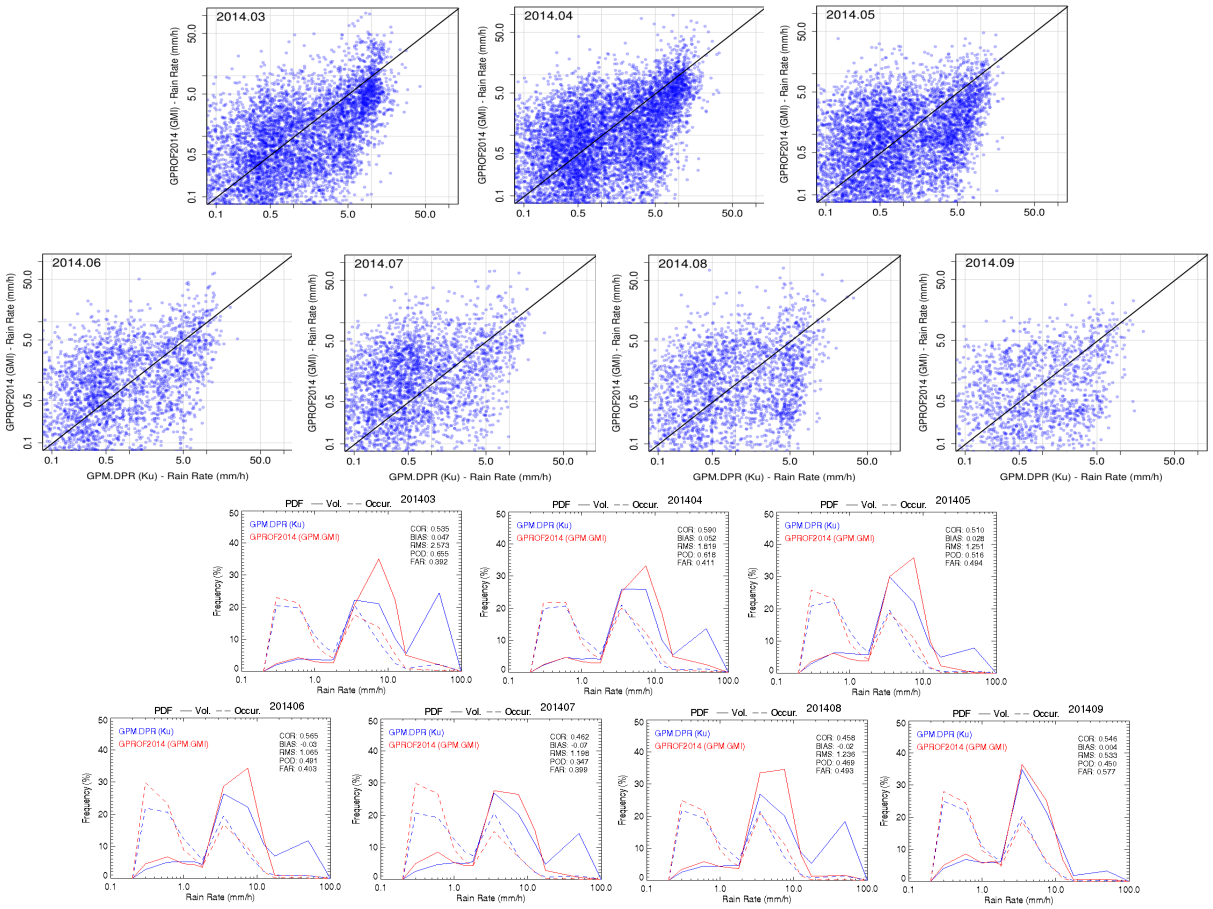

SOURCE: Author's production.

Figure 5.5 depicts the Taylor and Performance diagrams, which summarize, through the continuous and categorical variables, the relation between COR, RMSE, and SD indexes and the categorical scores SR, POD, BIAS, and the CSI simultaneously to show how closely a set of patterns matches observations. GPROF2014 for TMI presented slightly better correlation with TRMM PR than the GPROF2014 for GMI against GPM DPR. However, the COR comparisons for all the months ranged from 0.46 to 0.65. The normalized SD for almost all the cases are encountered between 0.5 and 1.0. The RMSE for the cases are in between 0.7 and 1.0. Such relatively low values of RMSE and normalized SD indicates a slightly underestimation of GPROF2014 for both the TMI and GMI observations (Fig. 5.5a). A better categorical performance was observed during the wetter months (placed in the upper right region in Fig. 5.5b), with accurate rainfall detection, characterized by low confidence intervals, with special attention for April by GPROF2014(TMI) against TRMM PR.

Figure 5.5 - (a) Taylor diagram and (b) performance diagram showing monthly metrics of TRMM PR and GPM DPR (Ku) versus GPROF2014 for TMI and GMI, respectively, from March–September 2014. The circle (rectangle) represents the TRMM PR x GPROF2014(TMI) (GPM DPR x GPROF2014(GMI)) for each month. The location in the performance diagram gives the value of performance statistics (POD, BIAS, SR (1-FAR), and CSI) with cross hairs representing the confidence interval.

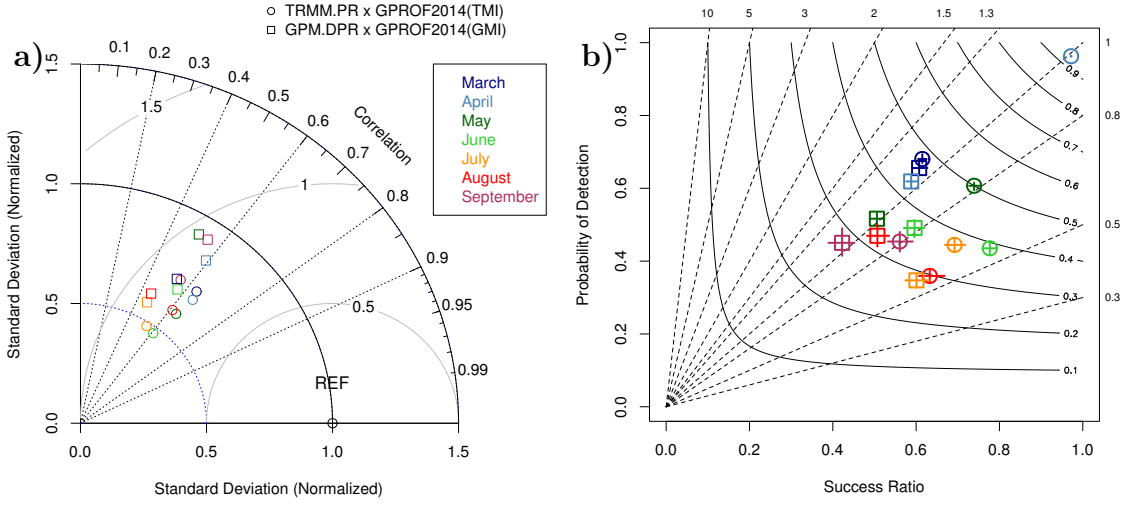

SOURCE: Author's production.

5.3.2 Spatial verification

Beyond the previously assessed pixel-versus-pixel evaluation methods, this section compares, through the MODE object-based toolkit, the performance of both level-2 rainfall retrievals techniques in reproducing the physical characteristics (i.e., number, size) of precipitating systems over the Brazilian Amazon. MODE produced a large number of attributes for single and matched pairs, for this case linking both the rainfall retrieval fields, and these attributes can be used for more detailed comparisons of single storms and/or satellite overpasses. Figure 5.6 provides an illustration of the MODE objects obtained from GPM DPR (Ku band) near surface rainfall retrievals and GPROF2014 (GMI) rainfall retrievals valid at 0553 UTC 12 March 2014, both resampled to similar spatial resolutions (12-km). It is possible to observe that simple precipitation objects are identified and well represented by both the satellite products. However, those precipitation objects differ from each other in different aspects (e.g., centroid distance, area, angle, symmetry, among others), which are investigated here during the seven months.

Given the variety of measures computed by MODE, the accuracy is evaluated when objects are matched between the forecast field (GPROF2014 for TMI and GMI) and observed field (TRMM PR and GPM DPR). The unmatched object count represents misses/false alarms. The differences between the forecast and observed numbers of precipitation objects, area, and location attributes are computed. Table 5.2 depicts the total numbers (counts) and area of precipitation objects (matched and unmatched) from the two pairs of dataset fields under comparison, based on the period from March-September 2014. The total number of TRMM PR-GPROF2014(TMI) objects are greater than those obtained from the GPM DPR-GPROF2014(GMI), which can be explained by its number of overpasses considered. However, the portion of unmatched TRMM PR object are considerable larger than for GPM DPR and their respective fields. On the other hand, the total area of objects from GPM DPR-GPROF2014(GMI) are significantly larger than from TRMM PR-GPROF2014(TMI). The portions of matched/unmatched total area of objects indicate good performance of GPROF2014 for TMI and GMI in representing the total area of objects, although GPROF2014 for GMI presented more misses/false alarms than the GPM DPR. The TRMM PR presented a greater portion of unmatched number and area of objects than all the products under study.

The statistical results (centroid distance and displacement) of the matched objects are analyzed separately for both the comparisons. Tables 5.3 and 5.4 de-

Figure 5.6 - An example illustrating the MODE output objects: (top) GPM DPR (Ku band) near surface rainfall estimates (left) and GPROF2014 (GMI) rainfall retrievals (right) valid at 0553 UTC 12 March 2014; (middle) the identified simple matched objects; and (bottom) the object identification index. Both the rainfall fields are on the 12 km domain. Similar colors between the fields indicate matched objects. The black lines surrounding objects are the convex hulls (clusters). Dashed lines indicate the coincident DPR Ku band and GMI swaths. A summary of the main MODE object results are also shown.

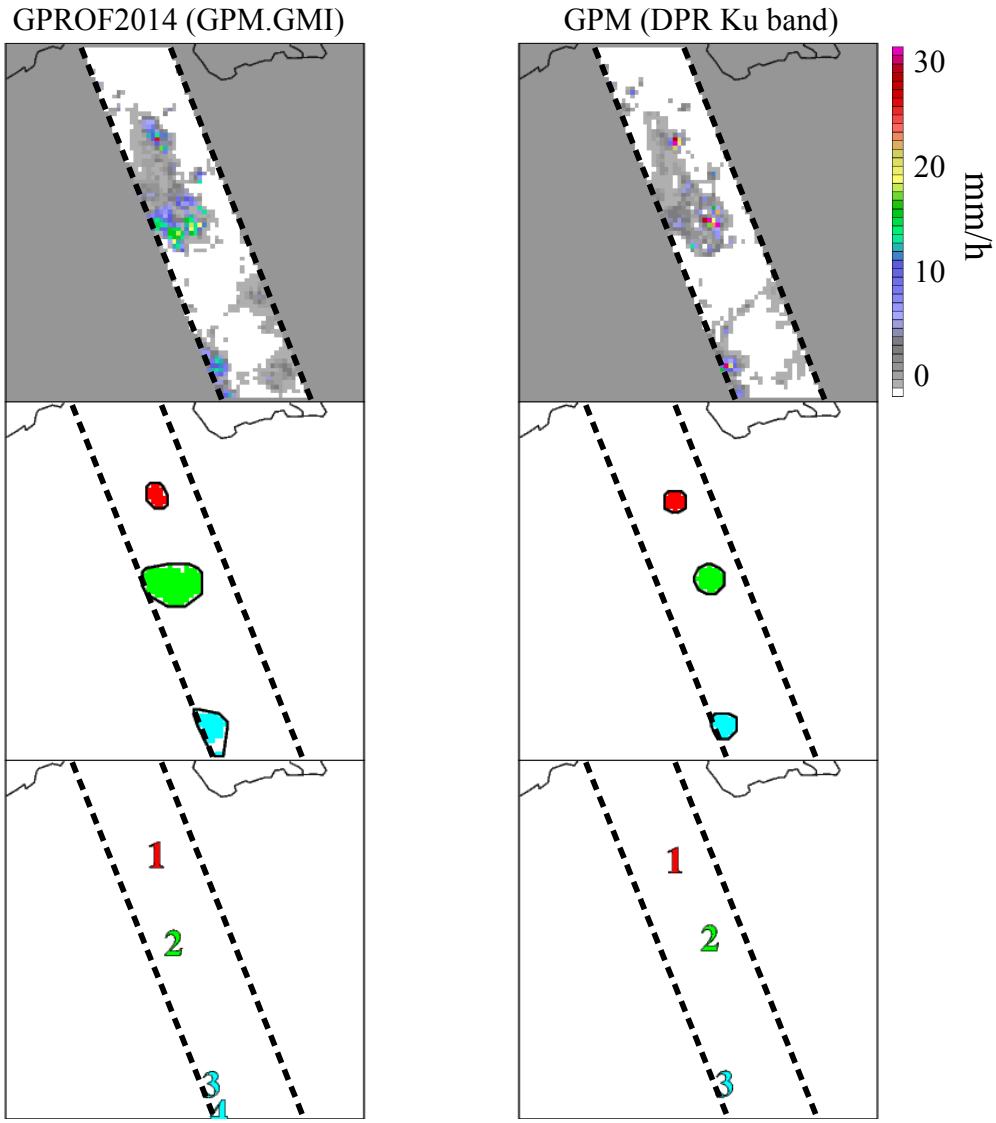

CLUS PAIR	CEN DIST	ANG DIFF	FCST AREA	OBS AREA	INTER AREA	UNION AREA	SYMM DIFF	FCST INT 50	OBS INT 50	FCST INT 90	OBS INT 90	TOT INTR
1	1.69	62.81	21	19	12	28	16	9.04	4.96	13.42	22.09	1.0000
2	5.51	19.38	100	32	22	110	88	9.26	5.12	15.42	22.12	0.9230
3	0.82	18.20	37	26	26	37	11	8.81	7.76	12.38	16.83	0.9858

SOURCE: Author's production.

Table 5.2 - General statistics of the number and area of objects identified by the MODE toolkit for the TRMM PR x GPROF2014(TMI) and GPM DPR x GPROF2014(GMI) precipitation fields, based on the period from March-September 2014.

Sensor	Total No. of Obj.	Matched Unmatched	Total Area of Obj.	Matched Unmatched
PR	330	178 152	4719	3945 774
TMI	176	158 18	3052	2948 104
PR-TMI	506		7771	
DPR	208	144 64	5158	4706 452
GMI	234	168 66	6262	5770 492
DPR-GMI	442		11420	

pict the centroid distance and displacement for the matched cluster objects. Even with the larger number of overpasses over the region (seen in Tab. 5.1), the total number clusters from TRMM PR-GPROF2014(TMI) are quite close to the GPM DPR-GPROF2014(GMI) pairs. The centroid distances (Tab. 5.3) reveal an opposite distribution pattern between those comparisons. For instance, TRMM PR-GPROF2014(TMI) presented higher (lower) values of the median (maximum) than the GPM DPR-GPROF2014(GMI) comparisons. Such behavior indicates that although the centers of mass of the identified objects from GPM DPR are farther apart (maximum), they are frequently closer (median) to those objects from GPROF2014(GMI). Meanwhile, looking at the X (west–east) and Y (north–south) displacements of the centroids (Tab. 5.4), the seven month summary statistics reveal that GPROF2014 (TMI and GMI) tended to have a general easterly and northerly bias in the location of objects in comparison with TRMM PR GPM DPR, explained by their positive median/mean X and Y values.

Table 5.3 - Cluster pair centroid distance for the TRMM PR x GPROF2014(TMI) and GPM DPR x GPROF2014(GMI) precipitation fields computed by the MODE toolkit. The centroid distance is the difference between the two centroids of the matched objects.

Pairs	Clusters	Min.	1st Qu.	Median	Mean	3rd Qu.	Max.
PR-TMI	206	0.000	1.237	2.094	2.942	4.108	11.360
DPR-GMI	232	0.1224	1.1180	1.8740	2.6000	2.9150	12.3900

Table 5.4 - Cluster pair centroid displacement for the TRMM PR x GPROF2014(TMI) and GPM DPR x GPROF2014(GMI) precipitation fields from the MODE toolkit. The centroid displacement examines the X (nominally east–west) and Y (nominally north–south) offsets of the centroids of two matched objects.

Pairs	Offsets	Min.	1st Qu.	Median	Mean	3rd Qu.	Max.
PR-TMI	X	-9.67900	-0.01786	0.83030	0.65080	1.74900	6.97300
	Y	-4.9190	-0.6613	0.3290	0.4712	1.4250	7.5830
DPR-GMI	X	-8.5000	-0.3390	0.3223	0.1768	1.0000	3.9010
	Y	-8.0100	-1.0720	0.5000	0.5117	1.4450	11.9700

Considering the general statistics, previously described for the whole period (from March-September 2014), we now evaluate MODE attributes monthly through the seven month study period, in order to investigate any seasonal dependency of the GPM Level-2 precipitation products on the object identification/characterization. Figure 5.7 shows the monthly time series of the number of total MODE objects computed from both the TRMM PR-GPROF2014(TMI) (Fig. 5.7a) and GPM DPR-GPROF2014(GMI) (Fig. 5.7b) comparisons. Furthermore, in Figure 5.7 we can see the portion of matched and unmatched objects from each precipitation product. A peak number of observed precipitation objects was found during the wet season (from March to May), and a minimum number was found during the dry period (June-September), observed in both of the comparisons. TRMM PR-GPROF2014(TMI) presented a higher occurrence of identified objects than GPM DPR-GPROF2014(GMI). The highest portion of number of precipitation objects is from TRMM PR (solid blue dot/line) (Fig. 5.7a), contrasting with the highest portion from GPROF2014(GMI) (Fig. 5.7b).

On the other hand, the monthly distributions of the number of matched objects (solid light blue line) in both comparisons are quite close and substantially larger than the unmatched number of objects. Such behavior is more prominent in the TRMM PR-GPROF2014(TMI) monthly comparisons. It is worth mentioning that TRMM PR also presented a higher occurrence of monthly misses/false alarms than the other precipitation products, explained by its higher number of unmatched objects. During the dry period the simple small objects (local convection) are not well detected in either comparison.

In order to investigate the simple precipitation objects identified in each field, the monthly time series showing the total area of precipitation objects identified by MODE for TRMM PR x GPROF2014(TMI) (Fig. 5.8a) and GPM DPR x

Figure 5.7 - Monthly time series showing the total numbers (counts) of precipitation objects identified by MODE for (a) TRMM PR x GPROF2014(TMI) and (b) GPM DPR x GPROF2014(GMI).

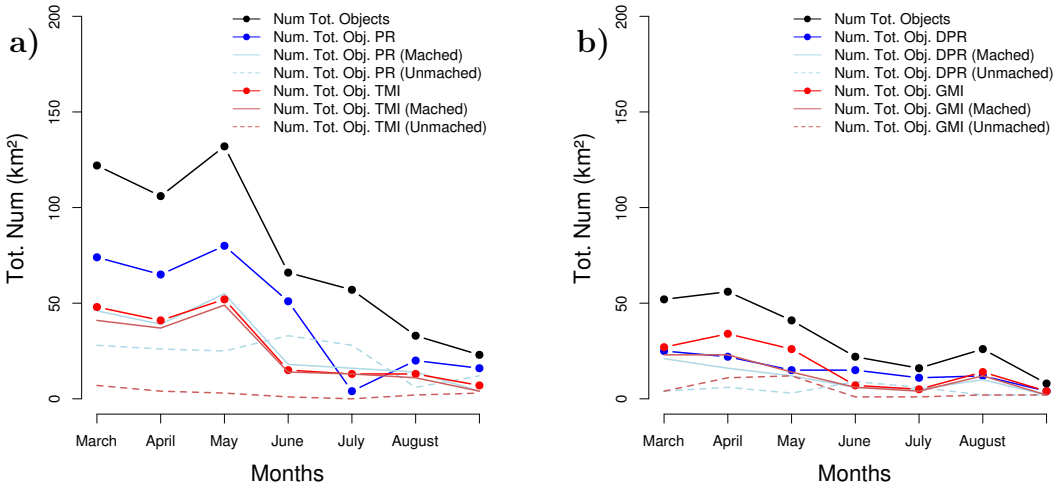

SOURCE: Author's production.

GPROF2014(GMI) (Fig. 5.8b) are assessed. The area of the identified precipitation objects in both comparisons is consistent across valid months, with the largest object areas during the wet season. The portion of matched/unmatched object area reveals a good performance of those precipitation products in estimating the area of the precipitating systems. However, an opposite object area detection pattern between the TRMM PR x GPROF2014(TMI) and GPM DPR x GPROF2014(GMI) comparisons was found. The overall area of the TRMM PR (GPROF2014(GMI)) precipitation objects was significantly larger than those identified in the GPROF2014(TMI) (GPM DPR) fields, regardless of the month examined. For instance, the portions of matched object areas from TRMM PR (GPROF2014(TMI)) in March and April are about 1192 and 946 km^2 (1006 and 860 km^2). For the GPM DPR and GPROF2014(GMI) the portion of matched object areas for the same months are 913 and 747 km^2 and 1104 and 1052 km^2, respectively.

The larger area values of observed precipitation objects during the wet season is related to the large scale climatological characteristics, with the action/interaction of distinct precipitating systems over the study region (e.g., squall lines, Intertropical Convergence Zone (ITCZ), among others). On the other hand, the lower values during the dry season may be attributed to the local factors and the occurrence of small and individual precipitating cells (and the nature of convective initiation)

around that period.

Figure 5.8 - Monthly time series showing the total area (in km ^{2}) of precipitation objects identified by MODE for (a) TRMM PR x GPROF2014(TMI) and (b) GPM DPR x GPROF2014(GMI).

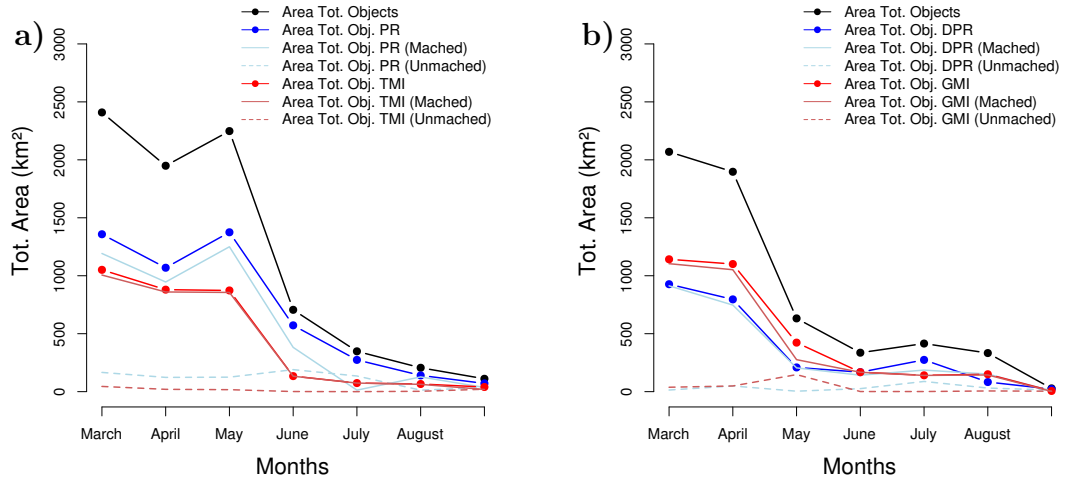

SOURCE: Author's production.

Figure 5.9 shows the monthly time series plot of the median centroid distances (Fig. 5.9a) and displacements (Fig. 5.9b) for all the GPROF2014 (TMI and GMI) objects compared to their matching observed TRMM PR and GPM DPR objects aggregated from March-September 2014 The centroid distance reveals an opposite monthly distribution between the comparisons. For example, the maximum median values of the centroid distance in TRMM PR x GPROF2014(TMI) comparisons was found in June 2014. In this month, GPM DPR x GPROF2014(GMI) presented the minimum median distance between the matched precipitation objects, either due to the impact of the object area size or location. However, during that period, for both comparisons, the X and Y displacements of the centroids reveal that GPROF2014 (TMI-GMI) tended to have a general easterly bias in the location of objects during almost all the months under study, except during September for GPROF2014 (GMI), which presented a westerly bias. For the Y displacements of the centroids, a seasonal dependency was found. During the wet (dry) period, a northerly (southerly) bias was noted in both comparisons, also except for GPROF2014 (GMI) in September. Although the active-based microwave retrievals seem to be more accurate than the passive microwave rainfall retrievals, which in some cases take into account those

Figure 5.9 - Monthly time series plot of the median centroid distances (black dot/line) and displacements (in the X (solid) and Y (dash)) for all the GPROF2014 (TMI and GMI) objects compared to their matching observed TRMM PR and GPM DPR objects aggregated from March to September, 2014. A positive (negative) value in the X direction (CENTX) indicates an easterly (westerly) bias and a positive (negative) value in the Y direction (CENTY) indicates a northerly (southerly) bias.

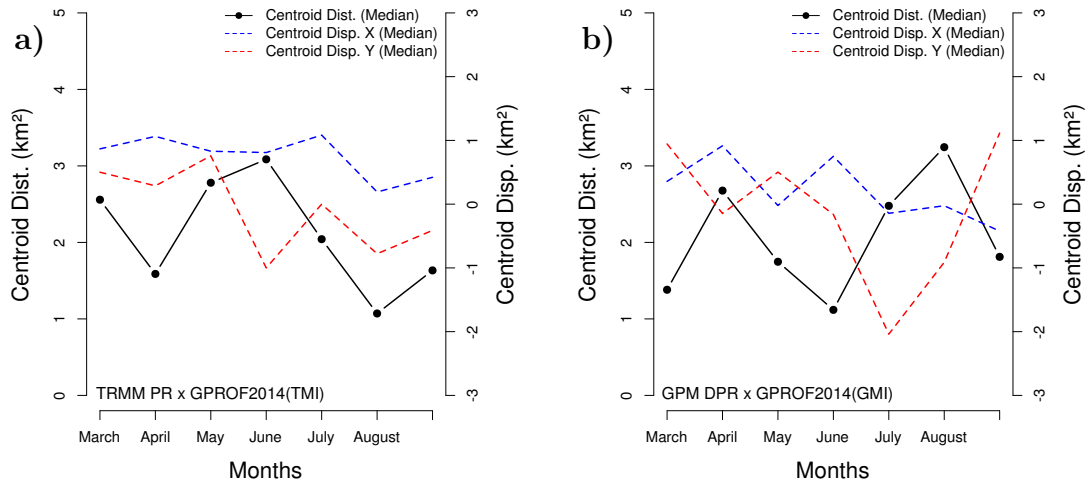

SOURCE: Author's production.

retrievals (i.e., GPROF2014 rainfall estimate approach), such information could normally vary given that those rainfall products are based on distinct approaches and the nature of precipitation is treated differently physically. Furthermore, the satellite overpasses under study do not necessarily capture the same object or stage of the life cycle of precipitating systems. Nevertheless, another point to be considered, which can be acquired from this section, is that the precipitation related to the low cloud top brightness temperatures (i.e., retrieved from TMI and GMI besides the GPROF2014 algorithm), may not precipitate at the surface, as well as that obtained from the active microwave rainfall retrievals (i.e., the near surface rain rate variable from the TRMM PR and GPM DPR). On the other hand, the identification of rainfall in the surface (object) observed by active microwave and not by the passive microwave rainfall retrievals may be associated with the presence of the bright band of stratiform precipitating systems and/or to the occurrence of warm rain (defined as liquid precipitation at the surface originating from pure liquid water clouds).

5.3.3 Case study: Investigation of possible sources of GPM rainfall object identification uncertainties

To investigate the observed differences in object characterization (e.g., object area) between the PMW and active MW rainfall retrievals, I examine the same single case study mentioned before (seen in Figure 5.6). The individual GPM overpass enables the physical examination of the performance of DPRKu against GPROF2014 for GMI rainfall retrievals in characterizing the object structures (spatial and vertical distributions). Figure 5.10 depicts the case study with emphasis on the identified object N.º 2 through both the rainfall retrievals. The object N.º 2 is also highlighted by the Contoured Frequency by Altitude Diagram (CFAD) (YUTER; HOUZEJR., 1995), computed by the DPRKu zFactorCorrected variable and constructed over the total object area obtained from both the DPRKu and GPROF2014(GMI) rainfall fields. The CFADs utilize all grid points and all available vertical levels inside the object N.º 2 and enables the investigation of the precipitating system under question, discriminating the convective and stratiform clouds by their vertical structures and also the height of freezing level (presence of bright band). Analyzing the CFAD for the N.º 2 precipitating system (total area object), in a gross sense, there is a mixed characteristic of convective and stratiform precipitation profiles. The height of freezing level was observed below 5 km, with maximum reflectivity values around 47 dBZ. Although the vertical profiles are all most typically stratiform (high contribution of 20-30 dBZ at surface), a large concentration of high values of reflectivity (up to 50 dBZ) was observed. A notable concentration peak is also observed between 8 and 9 km, which suggests a possible influence of ice scattering on cloud top.

To better understand the behaviors seen in object N.º 2 by CFAD from DPRKu zFactorCorrected, displayed in Figure 5.10, we now adopt the matched and unmatched object area criteria, in order to separately analyze the possible influence of the vertical profile structure on the rainfall object identification. The matched portion assumes that both the DPRKu and GPROF2014(GMI) correctly agree in identifying the object and the coincident overlapped object area is then analyzed. The unmatched portion is the opposite consideration; it takes into account the object area observed by GPROF2014(GMI) and not observed by DPRKu. Figure 5.11 depicts the bi-dimensional histogram (CFAD) of DPRKu zFactorCorrected for the matched and unmatched object area profiles. It is clearly evident that the agreement between DPRKu and GPROF2014(GMI) retrievals in object area identification (matched profiles) presented good performance in the convective precipitation situation (Fig. 5.11a). On the other hand, under the stratiform situation (unmatched

Figure 5.10 - Case study, seen as an example in Fig. 5.6, from a single GPM overpass over the central Amazon region: a) precipitation and object fields by GPMKu and GPROF2014(GMI) and b) the N.º 2 object area bi-dimensional histogram (CFAD), computed from DPRKu (zFactorCorrected variable)

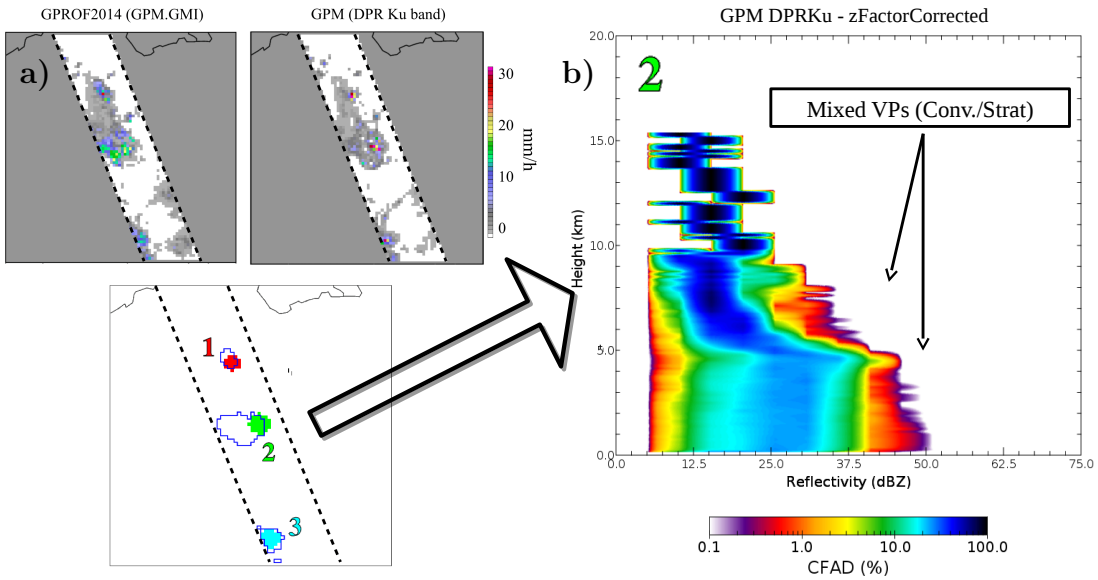

SOURCE: Author's production.

profiles), GPROF2014(GMI) tends to identify a larger object area than the DPRKu (poor performance), possibly due the presence of the bright band (Fig. 5.11b).

Figure 5.12 illustrates, through the five most significant vertical profiles inside of each unmatched and matched object area, the notable influence of the bright band on the performance of the GPROF2014(GMI) rainfall retrievals. The reflectivity increases downward to a maximum at the freezing level in both the convective and stratiform profiles (around 40 dBZ near 5 km). However, below the freezing level, the reflectivity decreases slightly and then remains constant down to the surface in stratiform unmatched object area profiles, with values around 32 dBZ near the surface. An opposite behavior in observed convective area profiles is seen. The reflectivity values significantly increase below the bright band, up to near 55 dBZ near surface. These differences in vertical profiles suggest that the PMW rainfall retrievals by GPROF2014 for GMI tend to overestimate the precipitation near the surface due the presence of the bright band.

Figure 5.11 - Bi-dimensional histogram (CFAD) of DPRKu zFactorCorrected for the N.º 2 object areas: a) matched (convective profiles) and b) unmatched (stratiform profiles).

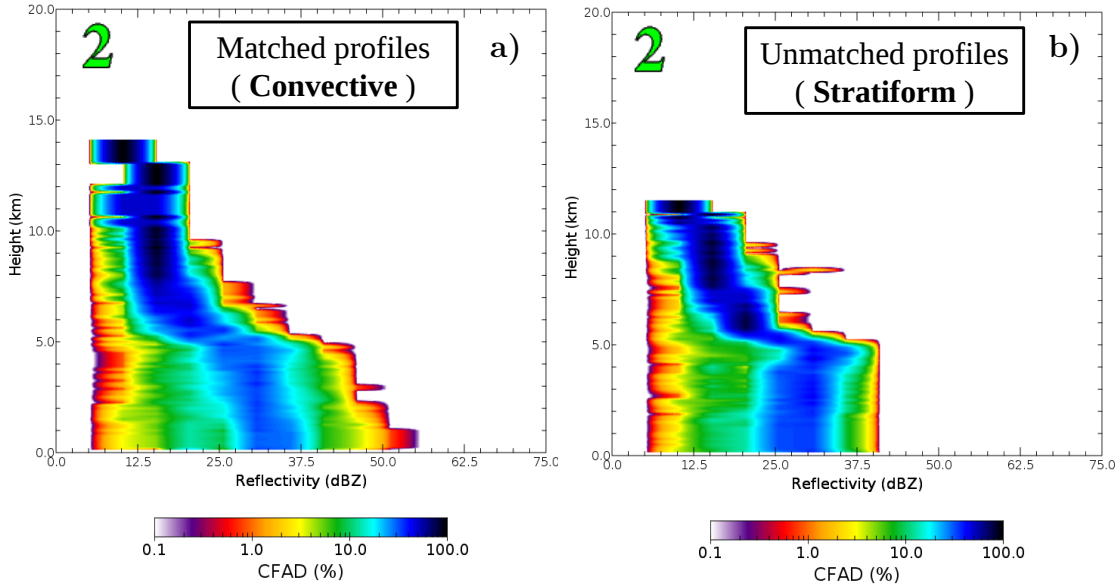

SOURCE: Author's production.

5.4 Summary and conclusions

This study evaluates the performance of GPM-level 2 PMW rainfall retrievals, specifically the GPROF2014 algorithm for TMI and GMI against the active MW (TRMM PR and GPM DPRKu sensors) rainfall retrievals, in reproducing the main characteristics of precipitating systems and its uncertainties over an area of 10 ° x 10 ° in the Brazilian Amazon. The performance evaluation is performed via traditional, pixel-by-pixel, and object-based (spatial) techniques through the Model Evaluation Tools (MET) toolkit.

Despite the underestimation of volume and occurrence of heavy rainfall, a good agreement of GPROF2014 for TMI and GMI versus TRMM PR and GPM DPR (Ku band) rainfall retrievals, respectively, was noted. The most evident good performance was found through continuous and categorical analysis, which suggested a seasonal dependency of GPROF2014 (TMI and GMI) in better quantifying high amounts of precipitation over the region. The wet period presented a better correlation than the dry period, slightly more notable in the TRMM PR x GPROF2014 (TMI) comparisons.

Figure 5.12 - Five most representative matched and unmatched vertical profiles from DPRKu zFactorCorrected.

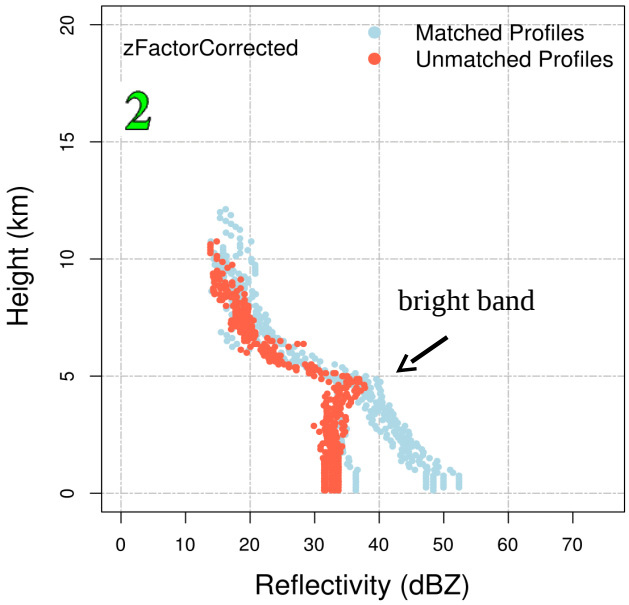

SOURCE: Author's production.

.

The total number and area of TRMM PR-GPROF2014(TMI) objects are greater than those obtained from the GPM DPR-GPROF2014(GMI), which can be explained by the number of overpasses considered. However, TRMM PR presented a large contribution of unmatched objects. Such behavior is repeated during the seven months under study. The wet (dry) season received a large (small) portion of matched object numbers and areas. The median distances and displacements of the matched centroids reveal a general easterly bias in the location of objects during almost all the months under study. During the wet (dry) period, a northerly (southerly) bias was observed. However, an opposite behavior between both comparisons was found in terms of centroid distance, although the mean values are quite similar during the seven months.

The structure of vertical profiles, as well the height of freezing level of precipitating systems, was the main source of uncertainty of GPROF2014 for GMI, related to the object area identification and its physical features. GPROF2014(GMI) tends to overestimate the precipitation near the surface due the presence of the bright band of precipitating systems.

Future studies should be designed to investigate: i) the characteristic distributions of other MODE variables, including other spatial techniques, such as the fractions skill score (FSS) neighborhood method; ii) other sensors (i.e., conical and cross-track scans) applied to the GPROF2014 algorithm; iii) exploring other regions in Brazil, with different precipitating regimes, for a longer period; and iv) the relation between the GPM MODE attributes and the precipitation type (i.e., convective and stratiform) and/or the life cycle of convective systems (initiation, maturation, and dissipation phases), i.e., provided by Forecast and Tracking the Evolution of Cloud Clusters (ForTraCC) toolkit.

6 ERROR MODELING APPLIED TO GPM-LEVEL 3 RAINFALL ESTIMATES OVER THE CENTRAL AMAZON REGION: CHARACTERISTICS AND VALIDATION

6.1 Introduction

This chapter aims to assess the characteristics and uncertainty distribution of GPM-Level 3 rainfall estimates (IMERG) via error modeling over the central Amazon region. The analysis considers the S-band SIPAM radar as a reference. The error modeling evaluations consider the PUSH framework, originally proposed by Maggioni et al. (2014). In this study, PUSH is well calibrated and validated for the study region and takes into account some local factors, as well as seasonality and surface types (i.e., land and river).

This work seeks to answer the follow scientific questions: (1) What are the characteristics and uncertainty distribution of GPM satellite rainfall estimates over the Brazilian Amazon via error modeling? (2) How can those uncertainties can be minimized for correct applications?

This chapter is organized as follows. In section 6.2, initially, the study area and the precipitation regime observed by both the IMERG and SIPAM data sources, previously investigated by Oliveira et al. (2016), are described. In the same section, the dataset and methodology are also described. The results, regarding the model characterization and calibration and its performance over the study region, are presented in section 6.3. In Section 6.4, a summary of the main results and conclusions are presented.

6.2 Study area, data and methodology

As a continuation of the Oliveira et al. (2016) study, this work focuses on an area in the middle of the Amazon basin, around the city of Manaus in the state of Amazonas, Brazil. The area covers a circle of 110 km in radius centered at 3.15 °S and 59.99 °W, where the operational S-band weather radar from the Amazon Protection National System (SIPAM) is located (seen in Figure 4.1).

The performance of IMERG in representing the characteristics and the diurnal cycle of precipitation over the study region is well presented by Oliveira et al. (2016). During the wet (dry) period, the volume and occurrence contributions of moderate (heavy) rainfall are clearly identified and strongly modulated by the diurnal cycle of precipitation. A strong dependence of the IMERG dataset performance on season-

ality is observed. Such performance is also prominent over the inland water surface type (along the Negro, Solimões, and Amazon rivers). Such behavior is related to the non-suitable adjustment linked to the continent-ocean surface type adopted by the GPROF2014 algorithm (i.e., GMI retrievals).

The precipitation data used for this study, taking into account the methodology here after described, consists of:

i one rain gauge located at Manaus city (at 3.1 °S and 60.0 °W) from National Institute of Meteorology (INMET). The INMET rain gauge is an automatic station, which provides hourly records. However, this study uses a period of 30 years of daily accumulations (mm day $^{-1}$);

ii the S-band SIPAM radar rainfall estimates, processed by Texas A & M University. The rainfall estimates are obtained through the CAPPI product at the 2.5 km vertical level. The spatial (horizontal) and temporal resolutions of the radar rainfall estimates are 2 km and at every 12 minutes. However, the radar rainfall retrievals are integrated to 30 minutes, to match the same temporal resolution of the satellite estimates;

iii the Integrated Multi-Satellite Retrievals for GPM (IMERG) - GPM Level-3 rainfall estimates ("Final" run version). The Level-3 IMERG Final Run (research) product is a quasi-global (60 °N–S) 0.1 ° x 0.1 ° and 30 min dataset, which is available from 1998 to the present in its final version (HUFFMAN et al., 2014; HUFFMAN et al., 2015).

A better description of the S-band SIPAM radar and IMERG rainfall retrievals and its performance over the study region can be found in Oliveira et al. (2016) (see chapter 4 for more details).

Thus, based on the currently available data, previously described, the sample period adopted in this study ranges from 12 March 2014 to 17 August 2015 (17 months of half-hourly resolution coincident radar-satellite dataset).

The methodological approach considered in this study for uncertainty characterization, via error modeling, consists of the adoption of the PUSH model, recently developed by Maggioni et al. (2014). PUSH is a framework to estimate errors associated with satellite rainfall retrievals at each grid point and time step, given a certain reference. In addition, based on an estimate of the probability density function (PDF) of the actual precipitation, PUSH evaluates several components of the

satellite precipitation error, including: *i*) missed precipitation events (the satellite records a zero, but the reference detects precipitation); *ii*) false alarms (the satellite incorrectly detects precipitation, as the reference observes no rain); and *iii*) hit biases (both satellite and reference detect precipitation, but they disagree on the amount).

The uncertainty of IMERG rainfall estimates over the central Amazon region arises based on the surface type and also the precipitation regime under study (OLIVEIRA et al., 2016). Such characteristics lead to understand and seek how to minimize the impact of these criteria on the performance of satellite retrievals. The surface type factor consists of an assumption of a land cover map that distinguish the surface types (in this case, over the central Amazon region, land and inland water). The land-river and the S-band SIPAM radar limitation masks are combined with each other and resampled to a 0.1° x 0.1° grid (Figure 6.1). On the other hand, the seasonality factor (precipitation regimes), has be investigated for the Brazilian Amazon through distinct approaches, e.g., Liebmann e Marengo (2001), Machado et al. (2004), Satyamurty et al. (2010), among others. However, although the Ama-

Figure 6.1 - S-band SIPAM radar limitation mask and land-river mask combinations.

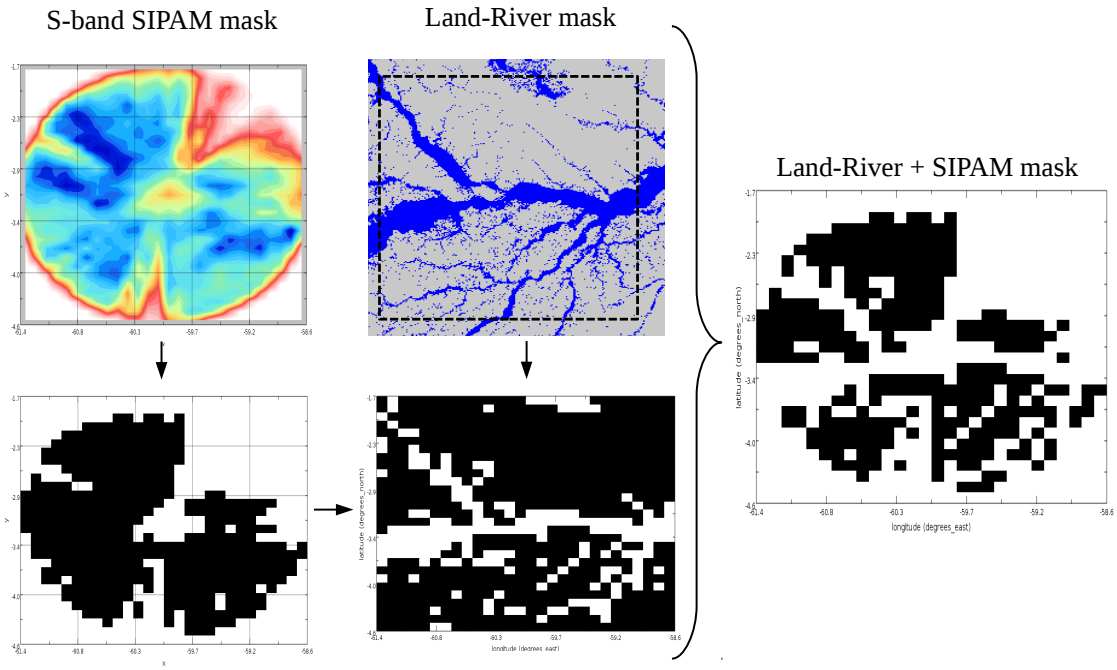

SOURCE: Author's production.

Table 6.1 - Periods used for PUSH calibration and validation for both the wet and dry seasons through the IMERG satellite rainfall estimates and S-band SIPAM radar retrievals as a reference.

	Calibration	Time steps	Validation	Time steps
Dry	2014.06.15 - 2014.12.21	8043	2015.05.24 - 2015.08.17	3416
Wet	2014.12.22 - 2015.05.23	6641	2014.03.12 - 2014.06.14	3865

zon region presents a very well defined and regionalized dry and wet season pattern (SANTOS et al., 2015), such behaviors may vary depending on the year under investigation and the interaction of certain remote and large-scale phenomena or their joint acting (LIEBMANN; MARENGO, 2001; VILLAR et al., 2009). Considering this, in view of the importance of a better definition of the rainy and dry seasons for different purposes (e.g., climatic, hydrological, agricultural, among others), Liebmann e Marengo (2001) developed an objective method of onset and demise identification of the rainy season, later used and adapted by Bombardi e Carvalho (2009) and Coelho et al. (2016), and currently operational at the Center for Weather and Climate Studies (CPTEC) (http://clima1.cptec.inpe.br/). In summary, according to Liebmann e Marengo (2001), such methodology takes into account the relation between the mean precipitation for the pentad (mm day $^{-1}$) and the climatological annual mean daily precipitation (mm day $^{-1}$) to define the onset and demise of the rainy season.

Thus, the errors associated with the satellite rainfall estimation by IMERG product, for each grid point and time step, are characterized via the PUSH error model framework (MAGGIONI et al., 2014). Such uncertainties (error estimates) and its found parameters will be discriminated by surface type and according to the season (dry and wet). The analyses will consider different precipitation thresholds, which provide the assessment the distribution of error in their distinct rain categories/classes (from light to heavy rainfall events). Initially, the Liebmann e Marengo (2001) criteria is used to identify the onset and demise of the rainy and dry seasons in the dataset period. The approach is applied to a single rain gauge station, located within the radar coverage area (at Manaus city). Therefore, based on the 17 months of IMERG and radar data (coincident time steps), four distinct periods were considered. The time series for calibration and validation (independent period) were selected for both the wet and dry seasons, and are listed in Table 6.1. For instance, corroborating with Table 6.1, Figure 6.2 illustrates this initial step for the wet and dry definitions.

Given the IMERG satellite observation x and S-band SIPAM radar precipitation

Figure 6.2 - Precipitation regime over Manaus city (INMET station) and study periods for PUSH evaluations: calibration and validation for wet (blue) and dry (red) periods. Shaded area represents the rainy season based on the Climatological Normal (1961-1990), in black dot/line. The defined periods for PUSH are based on the Liebmann e Marengo (2001) criteria, which takes into account the actual observations (gray line/dot).

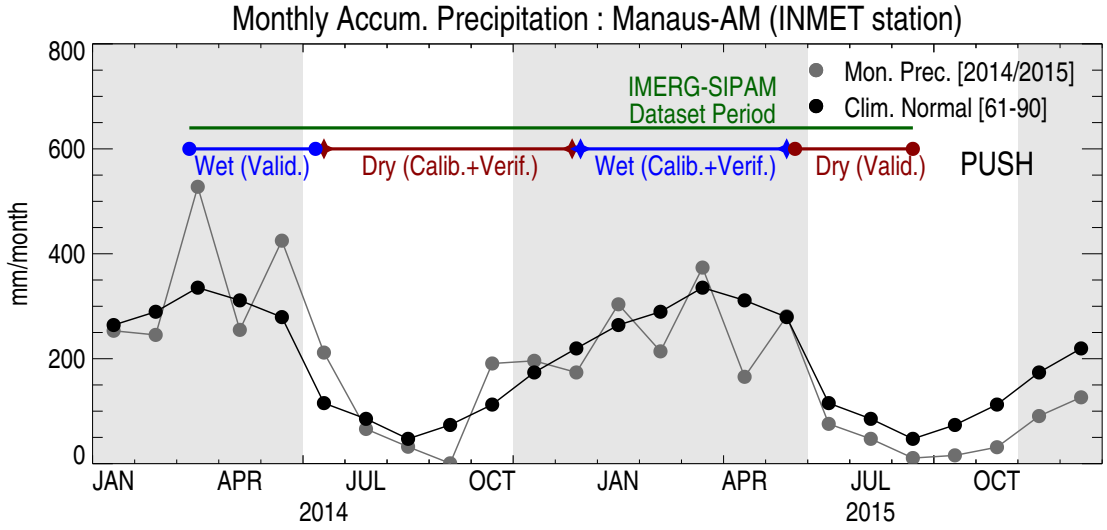

SOURCE: Author's production.

retrievals as a reference (or "truth") y, the framework provides an estimate of the PDF of the actual precipitation y at 30 minute time scale and 0.1 ° spatial resolution. The satellite error can then be computed as either the difference or the ratio between the satellite x and the expected value of the estimated precipitation distribution. The PDF of y is modeled differently in each of the following four cases, based on the minimum threshold of 0.2 mm h^{-1}: *i*) correct no-precipitation detection (case 00); *ii*) missed precipitation (case 01); *iii*) false alarm (case 10); and *iv*) hit (case 11) (MAGGIONI et al., 2014). Thus, PUSH parameters were first calibrated for both the dry and wet seasons. Once calibration is completed, the goodness of fit of the model is validated considering an independent period.

6.3 Results and discussion

The PUSH model is calibrated for three separate conditions (over land-river, over river only and over land only), during the dry and wet seasons over the central Amazon region. Based on the respective periods (seen in Table 6.1) of IMERG precipitation estimates and S-band SIPAM radar rainfall retrievals (as reference),

the framework is applied to estimate the errors in IMERG and, in an independent period, the model is then validated.

6.3.1 Model characterization and calibration

Figures 6.3 and 6.4 depict the probabilities of correct no-precipitation detection (P_{00}) and missed precipitation (P_{01}=1-P_{00}), for the over land-river, over river only and over land only surface type conditions, during the dry and wet seasons, respectively, considering the 0.2 mm h $^{-1}$ threshold. Such probabilities allow the giving of a general estimate of the false alarm (P_{10}) and hit (P_{11}) cases for each condition (season and surface type). Overall, during the calibration period, IMERG precipitation and the radar rainfall estimates both measured no-precipitation (RR $<$ 0.2 mm h $^{-1}$) greater than 91% of the grids/half hours, except for the dry season over river only (90%). The exponential curve shows less fit over river only, especially during the dry season, which suggests the lower ability of IMERG in detecting local rain cells along the river. During the wet season, although the values appear more scattered over river only, no significant differences were found in its probabilities. Such behavior indicates the influence of large scale rainfall amounts during the wet season, well defined by both precipitation products.

Figure 6.5 shows the case 0, when the estimated PDF of the missed precipitation amount y_{01} is modeled using a Gamma distribution (see Maggioni et al. (2014)). The S-band SIPAM radar precipitation probability density histograms for the calibration period for IMERG estimates lower than the 0.2 mm h $^{-1}$ threshold are presented. The corresponding modeled distributions are also shown, and relatively close in reproducing the reference precipitation distributions both in terms of shape and magnitude for both the dry and wet periods and over the three surface types. However, a slight overestimation of the error distribution at low values of satellite precipitation are observed. The model parameters (shape a_{01} and scale b_{01}) obtained during the dry and wet calibration periods are shown in Table 6.2, and will be applied to their respective validation periods.

Figure 6.6 shows cases in which the satellite estimates are larger than the threshold (i.e., case 1) during all the calibration period. The PDFs are shown for the IMERG satellite rain rates: 2.5 and 10 mm h $^{-1}$. It can be noted how the model is able to reproduce the observed error histograms for all precipitation ranges, in terms of shape and magnitude, also contrasting both the dry and wet seasons and surface types. In general, although the estimated density function adequately models the observed distributions for all the criteria studied, with low density differences, a

Figure 6.3 - Probability of correct no-precipitation detection (P_{00}) / false alarm (P_{10}) (left panels) and probability of missed precipitation (P_{01}) / hit (P_{11}) (right panels) for a 0.2 mm h^{-1} threshold over (a-b) land-river, (c-d) over river only, and (e-f) over land only, during the dry season.

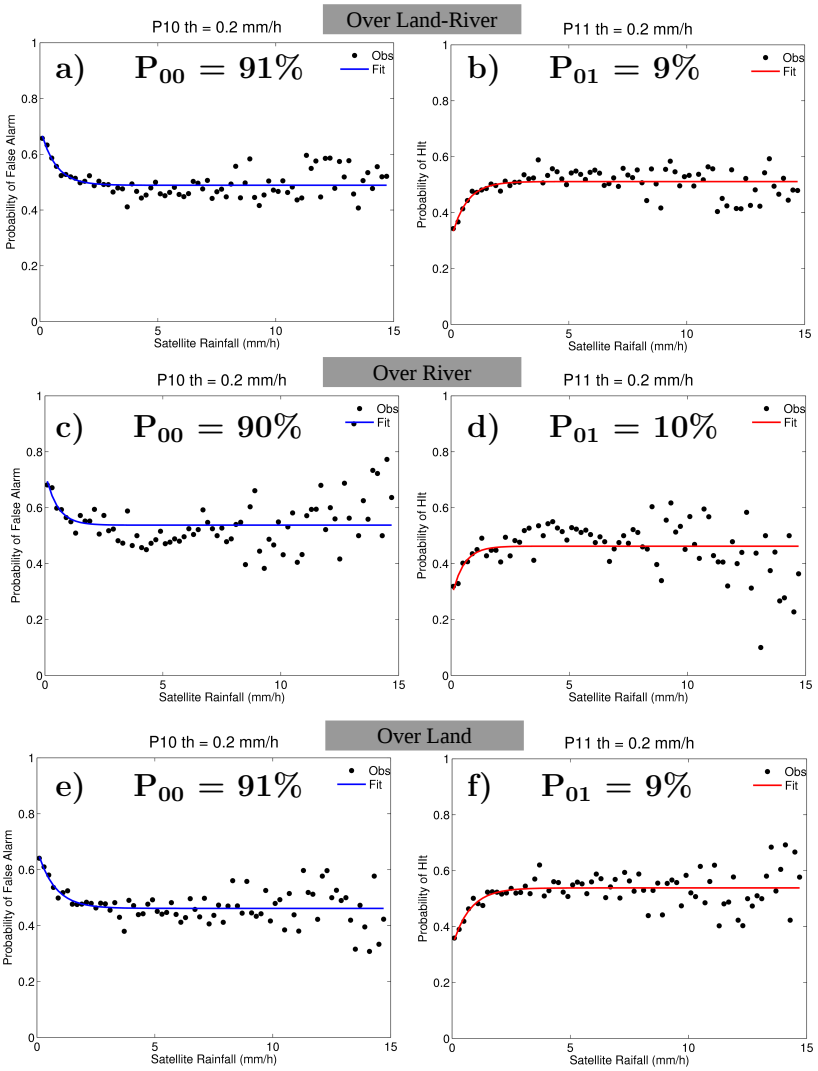

SOURCE: Author's production.

slightly overestimation (∼0.6), especially for light (observed) precipitation amounts, are noted. Thus, the estimated distributions are very close and adjusted to the observed values during the calibration period, suggesting future applications for an independent period in terms of validation.

Figure 6.4 - As in Fig. 6.2, but during the wet season.

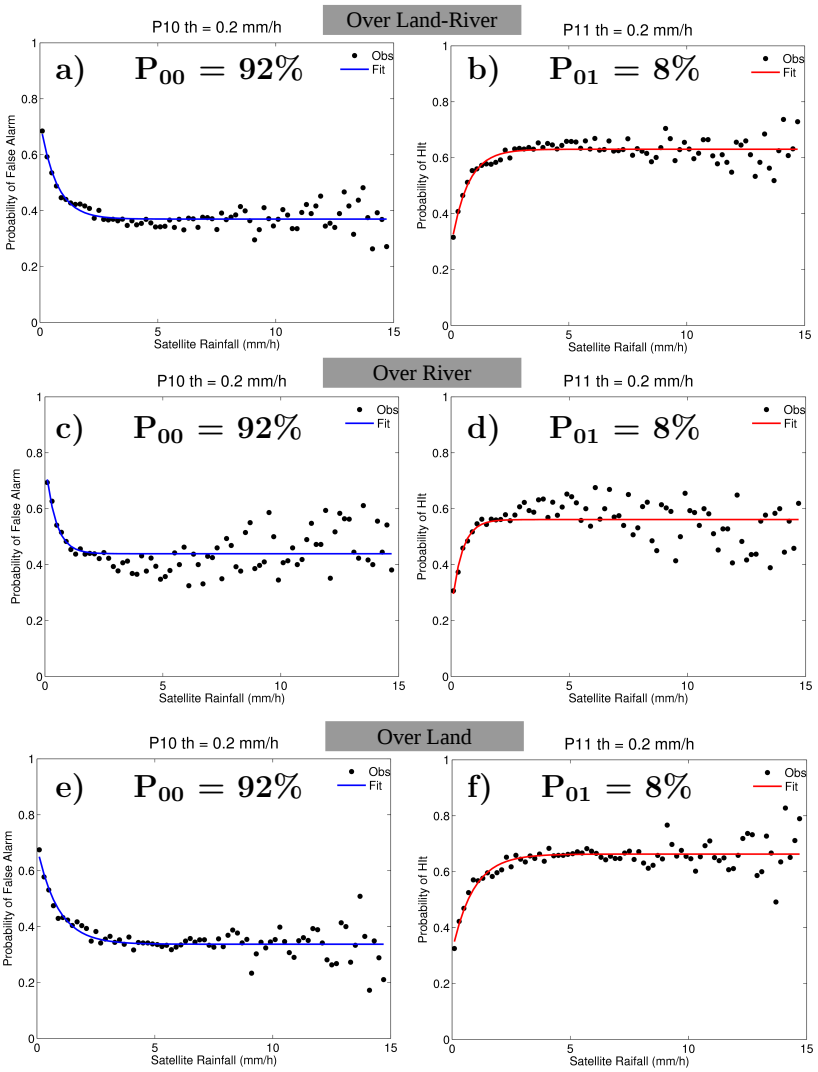

SOURCE: Author's production.

6.3.2 Model performance

Based on the model parameters, previously obtained during the calibration period, such results are now applied for the independent dry and wet periods, in order to validate the model. A first step to evaluate the performance of the PUSH model is to compare the estimated PDF with the reference precipitation distribution for case 0 and case 1. As well as during the calibration period (seen in Figure 6.5), during the validation period (Figure 6.7), a similar estimated distribution pattern in reproducing the reference precipitation distributions, both in terms of shape and magnitude,

Figure 6.5 - Histogram of the correct no-precipitation detection error (case 0) and missed precipitation distribution (case 01) for a 0.2 mm h^{-1} threshold over (a-b) land-river, (c-d) over river only, and (e-f) over land only, during the dry (left panels) and wet (right panels) seasons.

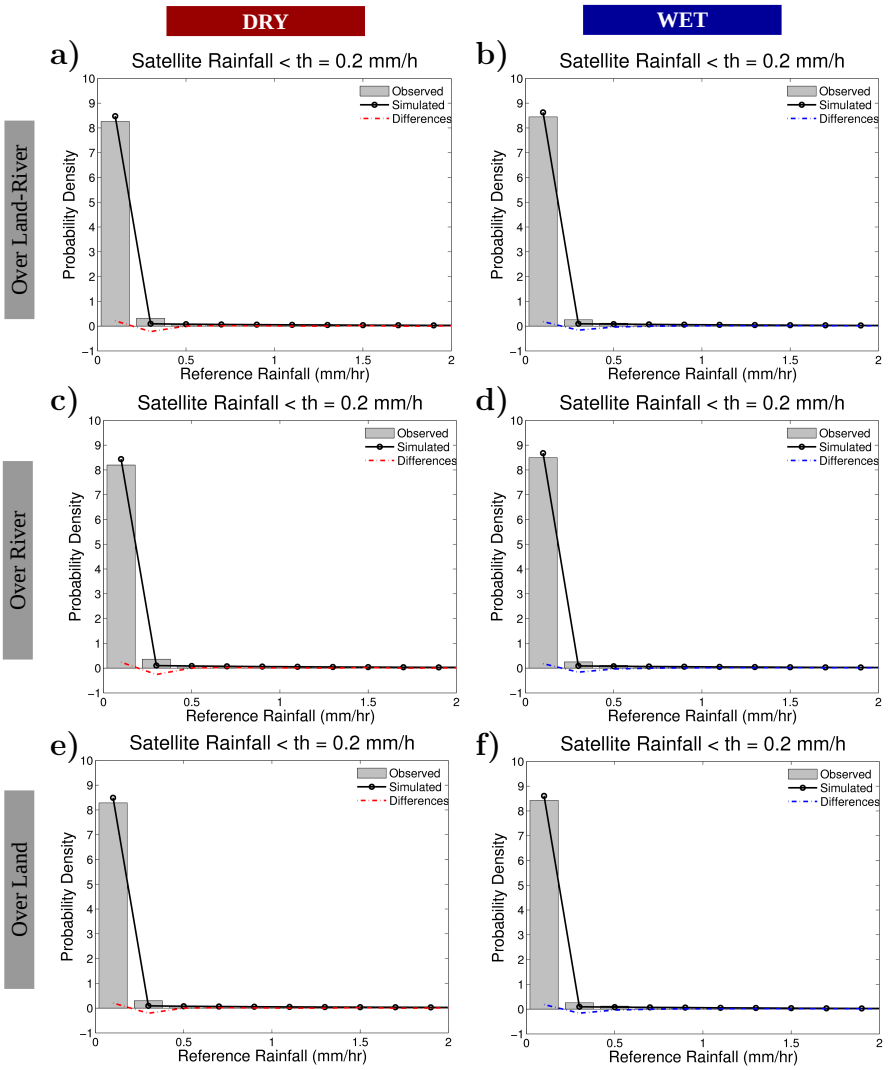

SOURCE: Author's production.

is observed. The differences between estimated and observed precipitation PDFs, which are normalized by the reference probability density, presented low positive (negative) values around 0.2 for the first (second) class of observed precipitation (between 0 and 0.2 mm h^{-1}).

On the other hand, several satellite thresholds (from 1 to 15 mm h^{-1}) are compared to the observed precipitation distribution (i.e., case 1), for the validation period

Figure 6.6 - PDF from observations (histograms) and simulated by the error model (black lines) and its differences (estimated minus observed probability densities) for the (a) dry (left panels, in red) and (b) wet (right panels, in blue) calibration periods and over land-river (upper panels), over river only (middle panels), and over land only (bottom panels). Examples for threshold values of satellite rain rates of 2.5 and 10.0 mm h $^{-1}$.

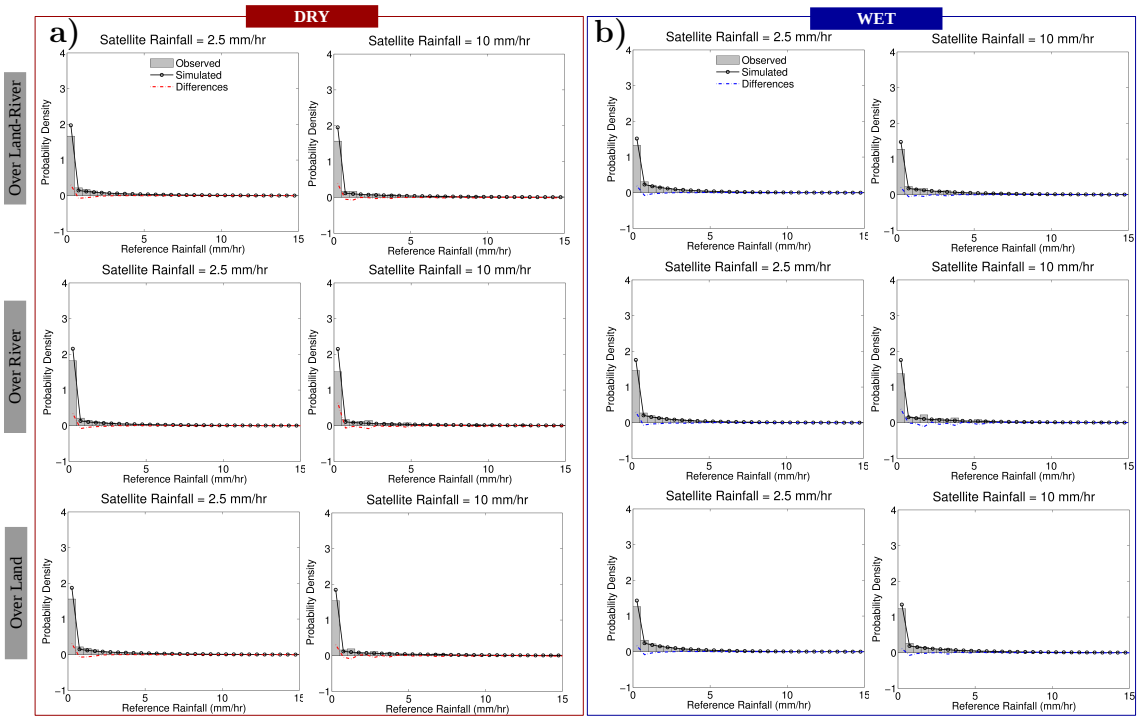

SOURCE: Author's production.

(Figure 6.8). The dry-wet performance contrasts are clearly observed, indicating great differences, especially for observed light precipitation distributions. In the dry season, negative differences (between 0.4 and 0.6) are observed for satellite precipitation raging from 1 to 4 mm h $^{-1}$, and positive difference values are about 0.5, most visible for the over land only surface type. An opposite behavior, with a large overestimation of the error distributions, for all satellite precipitation classes, is observed during the wet period. In addition, Figure 6.8 also shows a more prominent low performance over river only, which underestimated (overestimated) probability densities by about 0.6 for almost all the satellite thresholds for the 0.5 mm h $^{-1}$ reference rainfall, during the dry (wet) season.

In order to understand model performance over the distinct surface types, we now individually examine through case studies the error spatial distributions during the

Table 6.2 - PUSH model parameters (shape a_{01} and scale b_{01}), obtained during the dry and wet calibration periods over the three surface type conditions, to be applied to their corresponding validation periods.

	Parameter	Over Land-River	Over River	Over Land
Dry	a_{01}	0.8635	0.8534	0.8696
	b_{01}	1.8909	1.7755	1.9341
Wet	a_{01}	1.0054	0.9823	1.0144
	b_{01}	1.3568	1.4091	1.3374

Figure 6.7 - As in Fig.6.4, but for the dry (left panels) and wet (right panels) validation period.

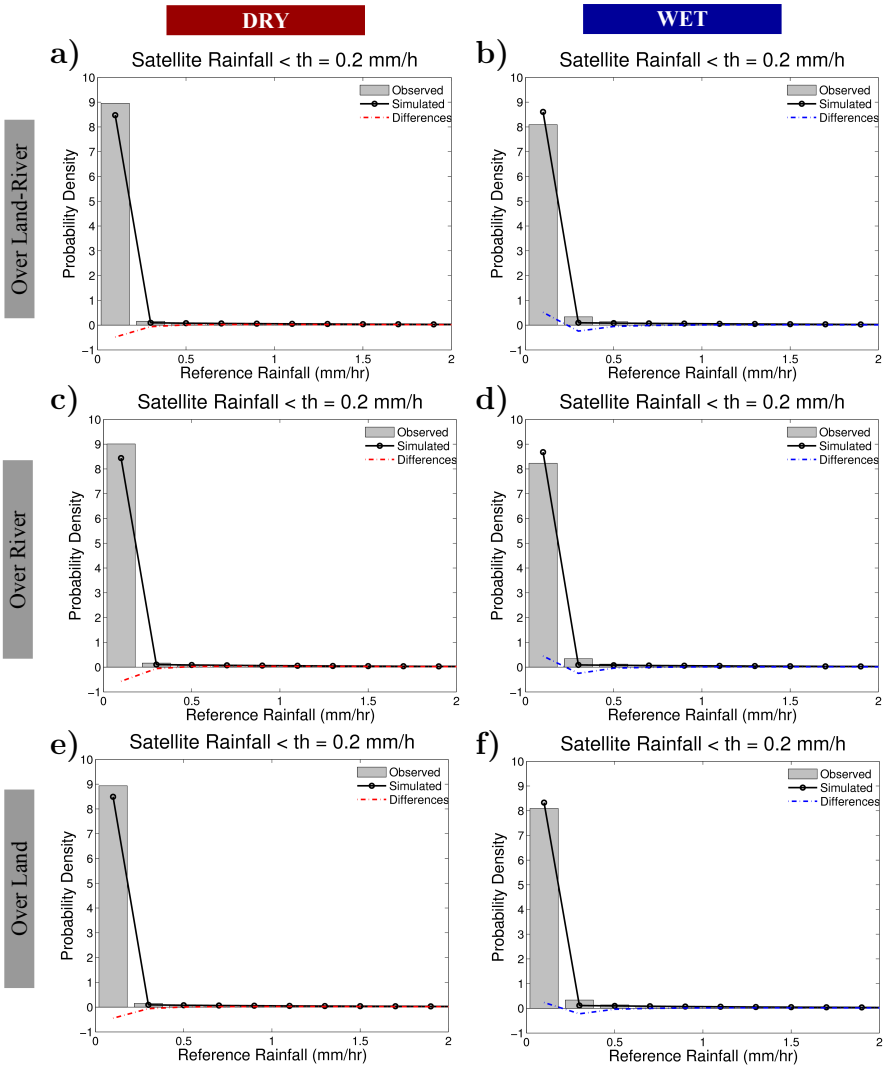

SOURCE: Author's production.

Figure 6.8 - PDF differences (estimated minus observed probability densities) for the (a) dry (left panels, in red) and (b) wet (right panels, in blue) validation periods and over land-river (upper panels), over river only (middle panels) and over land only (bottom panels), for threshold values of satellite rain rates from 1.0 to 15.0 mm h $^{-1}$.

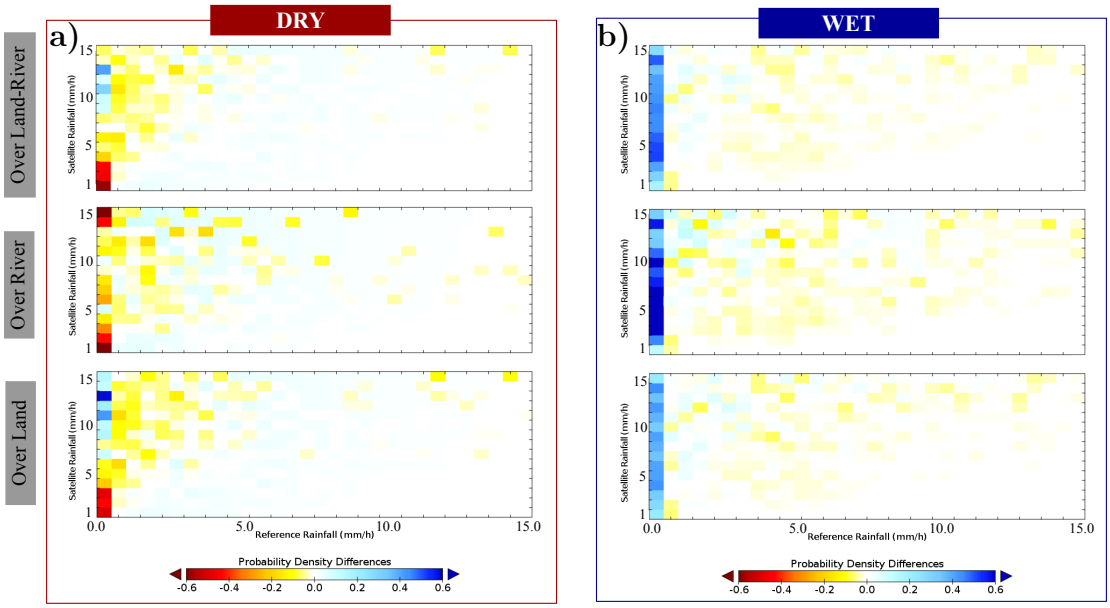

SOURCE: Author's production.

dry and wet periods. Figures 6.9 and 6.10 summarize the results of the validation tests for two precipitation events, during the dry (06:30-06:59 UTC on 28 May 2015) and wet (04:00-04:29 UTC on 12 March 2014) seasons, respectively. The observed error (left panels), computed as the difference between IMERG and S-band SIPAM radar; the estimated error (middle panels), computed as the difference between the S-band SIPAM radar and the mean of the modeled distribution; and the scatterplots of estimated versus observed errors (right panels), which also show their correlation coefficients, are shown for each surface type condition.

The PUSH error model adequately reproduced the spatial intensity patterns of the error in both precipitation events. Despite the poor performance in representing the error from light precipitation, the error model clearly underestimates (∼-0.5 mm h $^{-1}$) those classes of precipitation for both the dry and wet seasons. The estimated error also tends to overestimate the greatly underestimated observed errors, which explain the poor ability in representing the satellite underestimations. On the other hand, the model shows good performance in estimating the error for large amounts,

when the satellite greatly overestimates the precipitation. The scatterplots confirm the good agreement between observed and estimated errors, with some overestimation of the error at low values of satellite rain rates. The correlation coefficient presented values around 0.93 and 0.96, slightly varying depending on the surface type conditions and seasons. However, no remarkable difference in the model performance were found based on those criteria, since the model was calibrated separately.

To better illustrate the error estimated via the PUSH model against the observed error (IMERG-S-band SIPAM radar differences), previously exemplified in Figures 6.9 and 6.10, Figure 6.11 demonstrates the long term ability of PUSH to reproduce the error in terms of intensity and spatial distribution. The standard deviation (SD) of both the observed and estimated errors and their correlation coefficient (COR) are assessed for both the validation dry and wet periods. In order to evaluate the error distributions, the over river and over land errors are evaluated into a single observed/estimated error map. It is clearly evident, for both periods, that the modeled error produced lower SD values than the observed differences, indicating less error variability. However, the spatial distribution pattern of the errors were quite similar to each other, independent of the period, with higher values along the river, most evident during the wet season. The wet period is also characterized by higher SD than the dry period, when IMERG substantially overestimates the precipitation against the S-band SIPAM radar. The maximum SD values for the observed (modeled) error are about 2.2 mm h^{-1} (2.0 mm h^{-1}) for the dry season and 3.0 mm h^{-1} and 2.5 mm h^{-1} for the wet season. The spatial distributions of temporal COR presented great results, with most of the values around 0.8 and 1, for both the dry and wet periods, which implies in a good error estimation performance. However, a large part of these results were concentrated along the river, more prominent during the wet season. These results suggest that the PUSH error model could efficiently capture the systematic error along the Negro, Solimões, and Amazon rivers, clearly evident during the wet season as well as reported by Oliveira et al. (2016).

Finally, based on the error previously estimated via the PUSH model, I now apply such estimated errors to the original IMERG product to verify the model performance for the different conditions (surface type and seasons). The analysis is performed through continuous and categorical scores. Figure 6.12 depicts: the Taylor (Fig. 6.12a) diagram, which summarize how closely a set of patterns matches observations, using COR, RMSE, and SD indexes; and the Performance (Fig. 6.12b) diagram, which utilizes the geometric relationship between SR, POD, BIAS, and the CSI to display all four metrics simultaneously. A seasonal dependence, which is

Figure 6.9 - Comparisons of observed and estimated errors during a single time step (06:30-06:59 UTC on 28 May 2015) over land-river (upper panels), over river only (middle panels) and over land only (lower panels), during the dry season (validation period). The corresponding observed error is defined as the difference between the IMERG satellite retrieval and the S-band SIPAM radar observation. The estimated error is defined as difference between the satellite and the estimated reference precipitation (not shown). The scatterplots show the estimated error vs. the observed error.

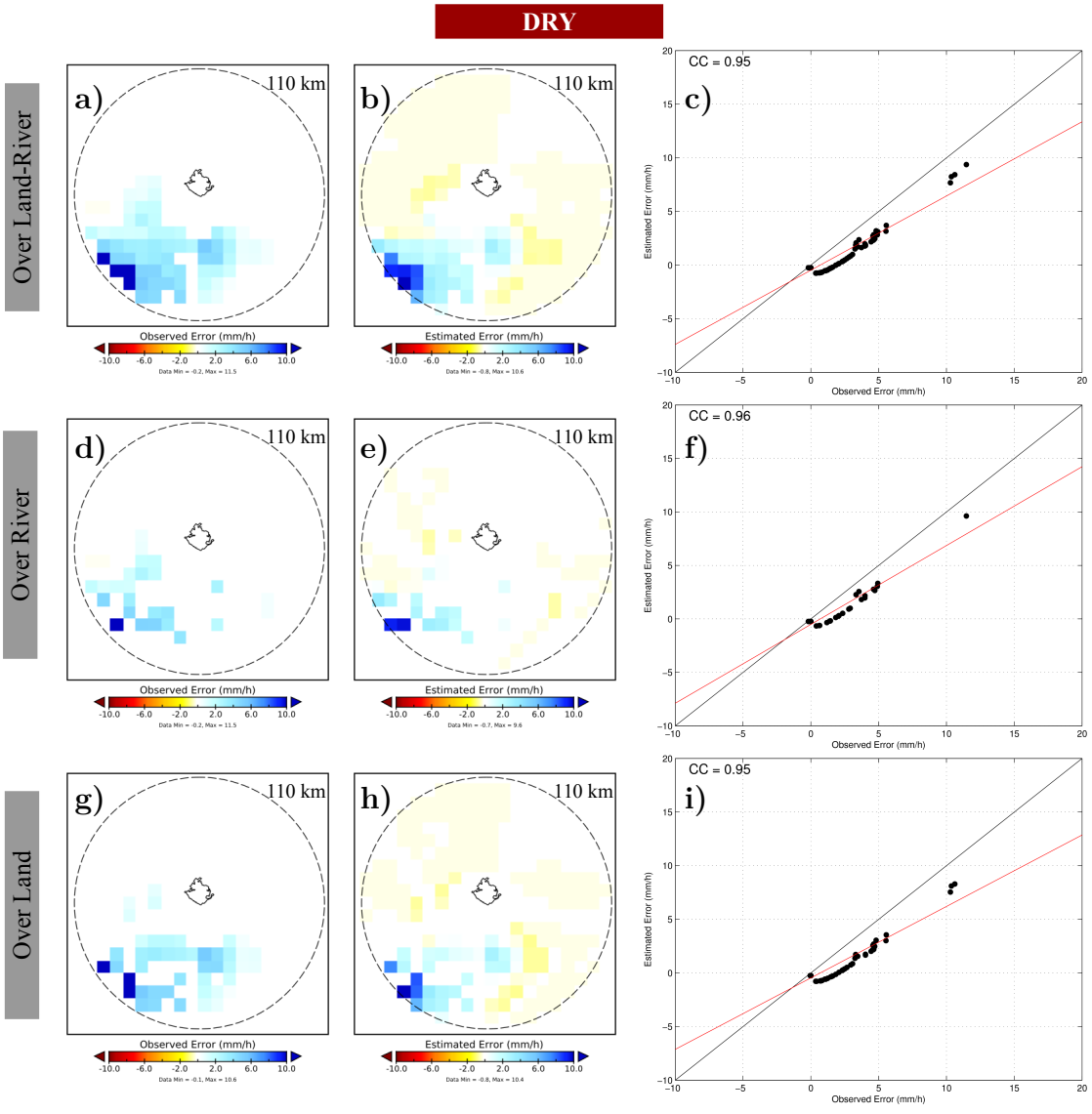

SOURCE: Author's production.

strongly linked to the precipitation regime in the region, is also observed in both the Taylor and Performance diagrams, as well noted by Oliveira et al. (2016). The drier period presents a clear under-performance in comparison with the wetter period,

Figure 6.10 - As in Fig. 6.8, but for the wet validation period (04:00-04:29 UTC on 12 March 2014).

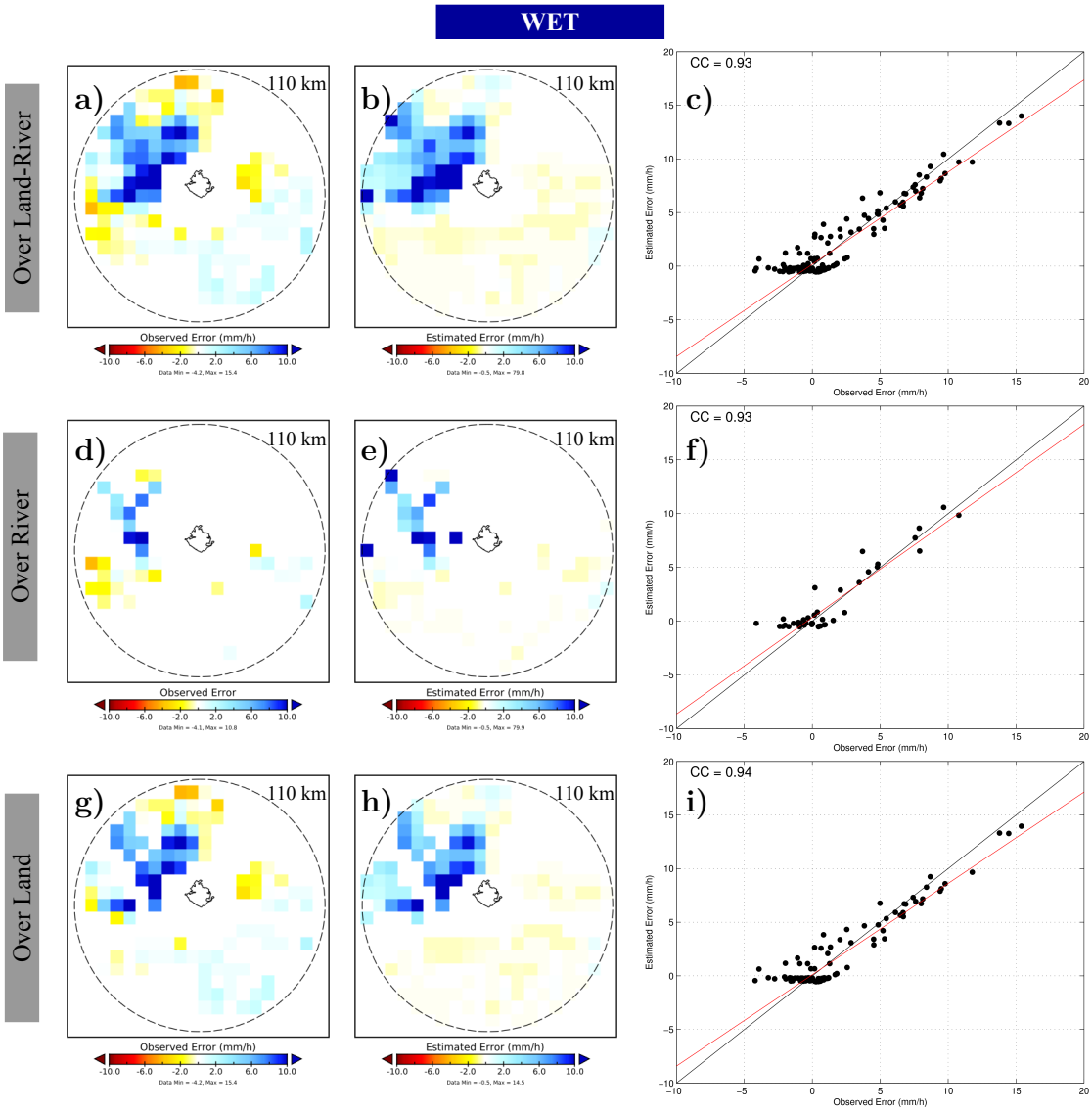

SOURCE: Author's production.

especially noted through the categorical evaluations (Fig. 6.12b).

The modeled IMERG presents a slight better performance than the original IMERG. The improvement was most evidently observed in the Taylor diagram, through the continuous scores. The COR for all the conditions increased from ∼0.1 to 0.2 for the dry period and ∼0.3 to 0.4 for the wet period. The most notable behavior was observed in the normalized SD and RMSE scores, of which the original IMERG presented higher values than the modeled IMERG. Such results indicate that the

Figure 6.11 - Spatial distributions of the standard deviation of (a-d) observed and (b-e) estimated errors and their (c-f) correlation coefficients over the dry (upper panels) and wet (lower panels) seasons (validation period).

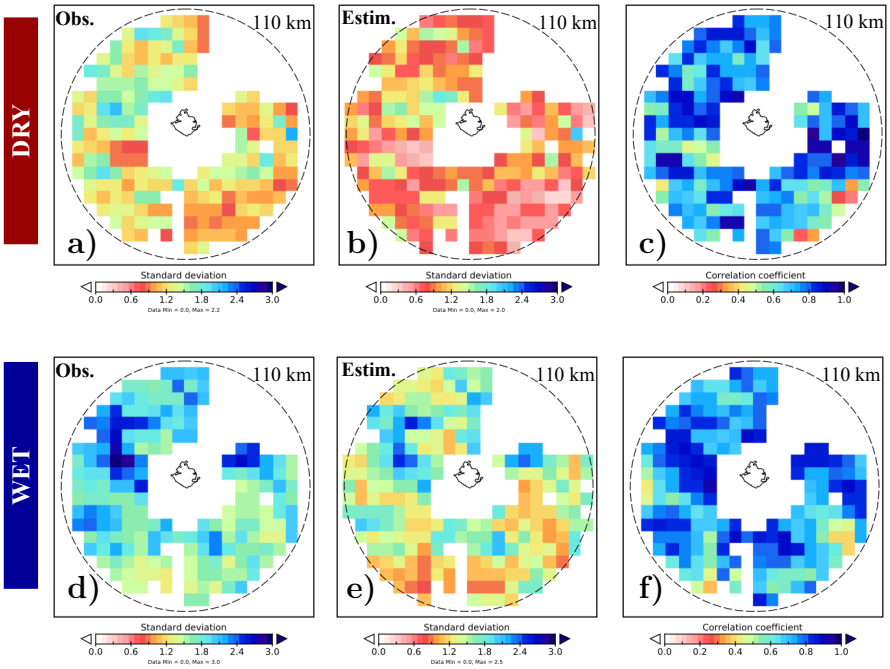

SOURCE: Author's production.

rainfall estimates from the modeled IMERG were closer to the S-band radar rainfall estimates (reference). On the other hand, despite the sight improvements in the continuous view, no significant improvements in the categorical analysis were observed, which suggests that the ability to detect local characteristics, especially during the dry season (i.e., local convection) are more dependent/linked to the physical approaches.

6.4 Summary and conclusions

In this study, the characteristics and uncertainty distribution of GPM-Level 3 rainfall estimates (IMERG V03D, "final" run) are assessed, via error modeling over the central Amazon region. The S-band SIPAM radar are used as a reference. The analysis is performed contrasting the dry and wet seasons, based on a period of 17 months, from March 2014 to August 2015. The error modeling evaluation considers the PUSH framework, originally proposed by Maggioni et al. (2014). PUSH is calibrated and validated for the study region, taking into account the local factors, as

Figure 6.12 - (a) Taylor diagram and (b) performance diagram showing dry and wet metrics of the IMERG original rainfall estimates versus IMERG modeled via the PUSH model, for different surface types over the Manaus region and for the validation period.

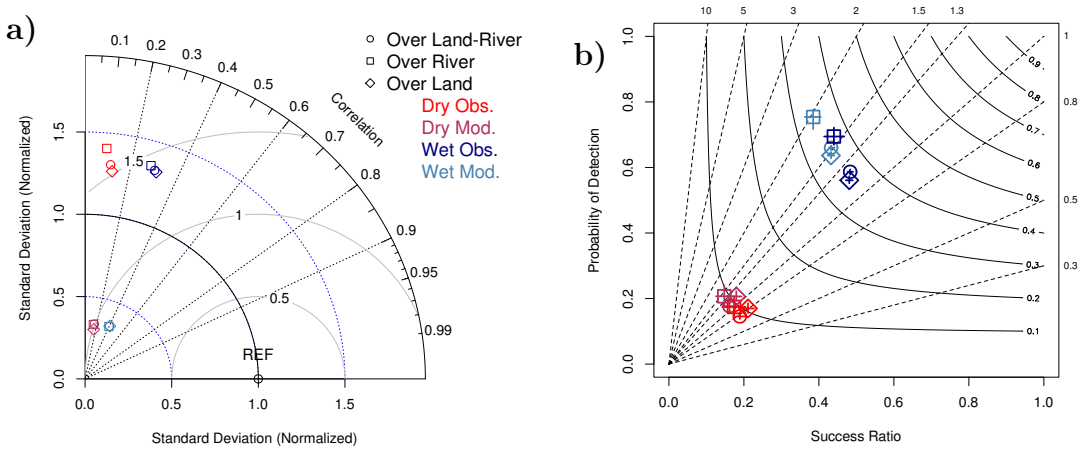

SOURCE: Author's production.

well as seasonality and surface types (i.e., land and river).

The analyses demonstrated that the PUSH model was suitable for characterizing the error from the IMERG algorithm when applied to S-band SIPAM radar estimates. During the calibration period PUSH presented promissory results for estimating the error for moderate to heavy rainfall thresholds. PUSH could capture the general distribution pattern of precipitation for both the seasons and surface types under study. However, the model exhibited very limited characterization of the light precipitation error distributions. For the case 0, PUSH slightly overestimated the threshold lower than 0.2 mm h^{-1} during both the dry and seasons. The overestimation of light rain rates was also observed for the case 1, although not significant for all the conditions under investigation.

During the validation (independent) period, PUSH could efficiently predict the error distribution, as well as for the case studies during the dry and wet periods. However, an underestimation (overestimation) of light satellite rain rates was observed during the dry (wet) period. Such behavior was clearly observed in case 0 (threshold lower than 0.2mm h^{-1}) and for case 1, especially over the river.

In general, the modeled error presented quite similar to the observed error in terms of spatial and intensity distributions. Although the estimated errors had a lower stan-

dard deviation than the observed error, they exhibited good correlations with each other, especially in capturing the systematic error along the Negro, Solimões, and Amazon rivers, especially during the wet season, previously reported by Oliveira et al. (2016). Lastly, the modeled IMERG was compared to the original IMERG during the independent period and a slight improvement was observed. The improvement was more evident through the continuous than the categorical analysis. In addition, future studies should be focused on investigating the random and systematic error components and the performance of the modeled IMERG in the diurnal cycle of rainfall distributions, also exploring other regions in Brazil and beyond.

7 MAIN CONCLUSIONS AND FUTURE WORK

7.1 Conclusions

In the first section of the dissertation, published in Oliveira et al. (2015), the analyses demonstrated that the GPROF passive microwave (SSMI/S) rainfall retrieval algorithm showed similar rainfall behavior patterns through the comparison with different datasets as reference, in this case, for the X-band CHUVA radar and 2A25-V7. GPROF presented overestimated frequency values, mainly for moderate rainfall (between 2 and 10 mm h^{-1}) and an underestimation of light (weaker than 1 mm h^{-1}) and heavy (heavier than 15 mm h^{-1}) rain intensities, although not very pronounced when compared to the 2A25-V7 rain reference. It was found that GPROF underestimated mainly the intensity of heavy rains and overestimated the intensities of light and moderate rains, considering both 2A25-V7 and X-band CHUVA radar data references. However, GPROF is slightly better correlated when compared with 2A25-V7 for an extended region than with the X-band CHUVA radar, which may be due to the greater coverage area, with more rain no-rain situations in each case. On the other hand, for this reason, the GPROF POD and FAR from the X-band CHUVA radar comparison show better results than the GPROF versus 2A25-V7 comparison. The GPROF algorithm failed to detect some precipitation areas weaker than 2 mm h^{-1}, mainly by comparing with 2A25-V7 over the extended region. In most cases the precipitation was associated with warm rain and stratiform clouds, classified by 2A25-V7. Two groups of performance in the Taylor diagram were found: the first (good performance) with low RMSE ($\sim$0.75), high COR ($\sim$0.7) and normalized STD close to 1 and the second (poor performance) with high RMSE ($\sim$1.5), low COR ($\sim$0.4) and high values of STD (normalized). The cases with good performance also showed better POD and FAR results than the cases with poor performance.

Since fewer channels contribute to rainfall retrieval over land (e.g., the 85.5 and 91.6 GHz scattering channels), more careful analysis is needed for these cases, considering with more detail the surface types and their characteristics (e.g., emissivity), in order to minimize error sources of the rainfall retrieved by a passive microwave technique.

In the second section of the dissertation, through the published Oliveira et al. (2016) article, as an important initial step for further satellite precipitation validation analysis, S-band-SIPAM radar rainfall estimates were validated against another radar-based precipitation product (i.e., from the X-band dual polarization radar from the CHUVA project). Although a slight overestimation of light rainfall and an underestimation of heavy rainfall were observed in the PDFv and PDFc analyses, SIPAM

radar was considered suitable to use as a reference dataset for validating satellite precipitation products. S-band SIPAM radar analyses revealed significant wet to dry contrast characteristics over the Manaus region through the PDFv and PDFc distributions. During the wetter (drier) period, the volume and occurrence contributions of moderate (heavy) rainfall were clearly identified and strongly modulated by the diurnal cycle of precipitation. Statistical pixel-by-pixel analyses revealed a strong dependence of the IMERG dataset performance on seasonality. The continuous and categorical evaluations indicated that the IMERG performance was directly linked to the monsoonal rainfall pattern over the region. The overestimation (underestimation) of rain volumes was particularly significant for heavy rainfall classes (>10 mm h^{-1}) during IOP1 (IOP2). The diurnal cycle analysis during wet and dry periods presented certain times with strong discrepancies between IMERG and the reference. During IOP1, an overestimation between 00:00–04:00 UTC and 15:00–18:00 UTC was observed, due to an overestimation of the occurrence and volume of heavy rainfall. During IOP2, an opposite behavior with strong rainfall volume and occurrence underestimation was found from 13:00–21:00 UTC, mainly due to the non-captured isolated convective rain cells in the afternoon. Analysis of the GPROF2014 algorithm rainfall sensor retrievals explained the IMERG's poor performance. GPROF2014 slightly overestimated and strongly underestimated heavy rainfall volume and occurrence, during IOP1 and IOP2, respectively. GPROF2014 for the GMI sensor rainfall retrievals presented the largest impact by inland water surface type, compared to other sensors. Thus, a significant portion of rainfall volumes and occurrences, observed by IMERG, came from the GPROF2014-GMI rainfall retrievals, most prominent over the inland water surface type, along the Negro, Solimões and Amazon rivers.

This study revealed important information regarding the IMERG and GPROF2014 quality and limitations over the Central Amazon region. This issue was observed along the Negro, Solimões and Amazon rivers, but other regions of the globe and surface types should be deeply investigated. Our findings are critical for the correct and successful applications of GPM rainfall estimates for applications, such as natural disaster monitoring, data assimilation systems, hydrological modeling, climate studies and for better understanding the physical processes of precipitating systems over the region. These analyses also contribute to improving the GPM algorithm.

In the third section of the dissertation, to be submitted, despite the underestimation of volume and occurrence of heavy rainfall, good agreement of GPROF2014 for TMI and GMI versus TRMM PR and GPM DPR (Ku band) rainfall retrievals,

respectively, was noted. The most evident good performance suggests a seasonal dependency of GPROF2014 (TMI and GMI) in better quantifying in particular the high amounts of precipitation over the region of study. The wet period presented better correlations than the dry period, slightly more notable in the TRMM PR x GPROF2014 (TMI) comparisons. The total number and area of TRMM PR-GPROF2014(TMI) objects were greater than those obtained from the GPM DPR-GPROF2014(GMI) algorithm, which could be explained by its number of overpasses considered. However, TRMM PR presented a greater contribution of unmatched objects. Such behavior was repeated along the seven months under study. The wet (dry) season received a large (small) portion of matched object numbers and areas. The median distances and displacements of the matched centroids revealed a general easterly bias in the location of objects during almost all the months under study. During the wet (dry) period, a northerly (southerly) bias was observed. However, an opposite behavior between both comparisons was found in terms of centroid distance, although the mean values were quite similar along the seven months. The performance of object area identification and its physical features were extremely linked to the vertical profile structures. GPROF2014(GMI) tended to overestimate the precipitation near the surface due the presence of the bright band in precipitating systems.

Finally, in the fourth section of the dissertation, the analyses demonstrated that the PUSH model was suitable for characterizing the error from the IMERG algorithm when applied to S-band SIPAM radar estimates. During the calibration period, PUSH presented promising results for estimating the error for moderate to heavy rainfall thresholds. PUSH could capture the general distribution pattern of precipitation for both seasons and the surface types under study. However, the model exhibited very limited ability to characterize light precipitation error distributions. For case 0, PUSH slightly overestimated the threshold lower than 0.2 mm h^{-1}, during both the dry and wet seasons. The overestimation of light rain rates was also observed for case 1, although this overestimation was not significant for all the conditions under investigation. PUSH could efficiently predict the error distribution during the validation (independent) period, as well as for the study cases during the dry and wet periods. However, an underestimation (overestimation) of light satellite rain rates was observed during the dry (wet) period. Such behavior was clearly observed in case 0 (threshold lower than 0.2mm h^{-1}) and for case 1, especially over the river.

In general, the modeled error was quite similar to the observed error in terms of

spatial and intensity distributions. Although the estimated error showed a lower standard deviation than the observed error, they exhibited good correlations to each other, especially in capturing the systematic error along the Negro, Solimões and Amazon rivers, especially during the wet season, previously reported by Oliveira et al. (2016). Lastly, the IMERG modeled was compared to the original IMERG during the independent period and a sight improvement was observed. The improvement was more evident in the continuous than the categorical analysis.

7.2 Future work

The results obtained in this study suggest a list of points/recommendations for further research:

- investigate the characteristic distributions of other MODE variables, including other spatial techniques, such as the fractions skill score (FSS) neighborhood method;
- include other sensors (i.e., conical and cross-track scans) applied to the GPROF2014 algorithm;
- explore other regions in Brazil, with different precipitation regimes, for a longer period; and
- examine the relation between the GPM MODE attributes and the precipitation type (i.e., convective and stratiform) and/or the life cycle of convective systems (initiation, maturation and dissipation phases), i.e., provided by Forecast and Tracking the Evolution of Cloud Clusters (ForTraCC) toolkit.

In addition, more studies need to be conducted to improve and assess PUSH applied to distinct datasets and for different regions. Future studies should be focused on:

- investigating the characteristics and distribution of random and systematic error components;
- evaluating the performance of modeled IMERG on the diurnal cycle of rainfall distributions, also exploring other regions in Brazil and beyond.

REFERENCES

AGHAKOUCHAK, A.; MEHRAN, A. Extended contingency table: Performance metrics for satellite observations and climate model simulations. **Water Resources Research**, v. 49, n. 10, p. 7144–7149, 2013. ISSN 1944-7973. Disponível em: <http://dx.doi.org/10.1002/wrcr.20498>. 12

AGHAKOUCHAK, A.; MEHRAN, A.; NOROUZI, H.; BEHRANGI, A. Systematic and random error components in satellite precipitation data sets. **Geophysical Research Letters**, v. 39, n. 9, 2012. ISSN 1944-8007. L09406. Disponível em: <http://dx.doi.org/10.1029/2012GL051592>. 16

ALCÂNTARA, C. R.; DIAS, M. A. S.; SOUZA, E. P.; COHEN, J. C. Verification of the role of the low level jets in amazon squall lines. **Atmospheric Research**, v. 100, n. 1, p. 36–44, 2011. ISSN 0169-8095. 42

AMITAI, E.; LLORT, X.; SEMPERE-TORRES, D. Comparison of TRMM radar rainfall estimates with NOAA next-generation QPE. **Journal of the Meteorological Society of Japan. Ser. II**, v. 87A, p. 109–118, 2009. 12, 13, 48, 49, 66

AMITAI, E.; PETERSEN, W.; LLORT, X.; VASILOFF, S. Multiplatform comparisons of rain intensity for extreme precipitation events. **IEEE Transactions on Geoscience and Remote Sensing**, v. 50, n. 3, p. 675–686, March 2012. ISSN 0196-2892. 15, 49, 66

ANGELIS, C.; MCGREGOR, G.; KIDD, C. Diurnal cycle of rainfall over the brazilian amazon. **Clim. Res.**, v. 26, p. 139–149, 2004. Disponível em: <http://www.int-res.com/abstracts/cr/v26/n2/p139-149/>. 42, 56

AONASHI, K.; AWAKA, J.; HIROSE, M.; KOZU, T.; KUBOTA, T.; LIU, G.; SHIGE, S.; KIDA, S.; SETO, S.; TAKAHASHI, N.; TAKAYABU, Y. GSMaP passive microwave precipitation retrieval algorithm: Algorithm description and validation. **J. Meteor. Soc. Japan**, v. 87A, p. 119–136, 2009. 2

AWAKA, J.; IGUCHI, T.; KUMAGAI, H.; OKAMOTO, K. Rain type classification algorithm for trmm precipitation radar. In: **Proceedings...** Singapore: IEEE, 1997. v. 4, p. 1633–1635. 37

BARNES, L. **Mesoscale objective analysis using weighted time-series observations**. Norman, OK, 1973. 60 p. NOAA Tech. Memo. ERL NSSL-62. 28

BARRETT, E.; KNIVETON, D. Over land precipitation. In: CHOUDHURY, B.; KERR, Y.; NJOKU, E.; PAMPALONI, P. (Ed.). **Passive microwave remote sensing of land-atmosphere interactions**. Utrecht: VSP, 1995. p. 571–598. 8

BOMBARDI, R. J.; CARVALHO, L. M. V. IPCC global coupled model simulations of the South America monsoon system. **Clim. Dyn.**, v. 33, p. 893–916, 2009. 88

BRAGA, R. C.; VILA, D. A. Investigating the ice water path in convective cloud life cycles to improve passive microwave rainfall retrievals. **Journal of Hydrometeorology**, v. 15, n. 4, p. 1486–1497, 2014. Disponível em: <http://dx.doi.org/10.1175/JHM-D-13-0206.1>. 22

BRINGI, V.; CHANDRASEKAR, V. **Polarimetric Doppler Weather Radar: Principles and Applications**. Cambridge, UK: Cambridge University Press, 2001. 664 p. ISBN 0521019559. 52

BRINGI, V.; THURAI, M.; HANNESEN, R. **GEMATRONIK. Dual-Polarization Weather Radar Handbook**. Neuss, Germany, 2007. 163 p. 2nd ed. Disponível em: <http://pmm.nasa.gov/sites/default/files/document_files/IMERG_doc.pdf>. 22, 23, 43

CASATI, B.; WILSON, L. J.; STEPHENSON, D. B.; NURMI, P.; GHELLI, A.; POCERNICH, M.; DAMRATH, U.; EBERT, E. E.; BROWN, B. G.; MASON, S. Forecast verification: current status and future directions. **Meteorological Applications**, John Wiley & Sons, Ltd., v. 15, n. 1, p. 3–18, 2008. ISSN 1469-8080. Disponível em: <http://dx.doi.org/10.1002/met.52>. 15

CASELLA, D.; DIETRICH, S.; PAOLA, F. D.; FORMENTON, M.; MUGNAI, A.; PORCÚ, F.; SANÓ, P. PM-GCD – a combined IR-MW satellite technique for frequent retrieval of heavy precipitation. **Nat. Hazards Earth Syst. Sci.**, v. 12, p. 231–240, 2012. 1

CAVALCANTI, I.; KOUSKY, V. Climatology of south american cold fronts. In: **Proceedings...** Wellington, New Zealand: AMS, 2003. 20

CHANDRASEKAR, V.; BRINGI, V.; RUTLEDGE, S.; HOU, A.; SMITH, E.; SKOFRONICK, J.; GAIL GORGUCCI, E.; PETERSEN, W. Potential role of dual-polarization radar in the validation of satellite precipitation measurements: rationale and opportunities. **Bull. Am. Meteorol. Soc.**, v. 89, p. 1127–1145, 2008. 2

CHUVA. **Cloudprocesses of tHe main precipitation systems in Brazil: A contribUtion to cloud resolVing modeling and to the GlobAl Precipitation Measurement**. 2017. http://chuvaproject.ctec.inpe.br/. Accessed on 10 March 2017. 11

CIMINI, D.; ROMANO, F.; RICCIARDELLI, E.; PAOLA, F. D.; VIGGIANO, M.; MARZANO, F.; COLAIUDA, V.; PICCIOTTI, E.; VULPIANI, G.; CUOMO, V. Validation of satellite OPEMW precipitation product with ground-based weather radar and rain gauge networks. **Atmos. Meas. Tech.**, v. 6, p. 3181–3196, 2013. 2, 29, 50

COELHO, C. A. S.; CARDOSO, D. H. F.; FIRPO, M. A. F. Precipitation diagnostics of an exceptionally dry event in São Paulo, Brazil. **Theor. Appl. Climatol.**, v. 125, n. 3, p. 769–784, 2016. 88

COHEN, J.; DIAS, M. da S.; NOBRE, C. Environmental conditions associated with amazonian squall lines: A case study. **Mon. Weather Rev.**, v. 123, p. 3163–3174, 1995. 42, 54

DAVIS, C.; BROWN, B.; BULLOCK, R. Object-based verification of precipitation forecasts. part i: Methodology and application to mesoscale rain areas. **Monthly Weather Review**, v. 134, n. 7, p. 1772–1784, 2006. 16, 67

DAVIS, C. A.; BROWN, B. G.; BULLOCK, R.; HALLEY-GOTWAY, J. The method for object-based diagnostic evaluation (MODE) applied to numerical forecasts from the 2005 nssl/spc spring program. **Weather and Forecasting**, v. 24, n. 5, p. 1252–1267, 2009. 16, 67

Di Paola, F.; CASELLA, D.; DIETRICH, S.; MUGNAI, A.; RICCIARDELLI, E.; ROMANO, F.; SANÓ, P. Combined MW-IR precipitation evolving technique (PET) of convective rain fields. **Nat. Hazards Earth Syst. Sci.**, v. 12, p. 3557–3570, 2012. 1

DOSSANTOS, M. J.; DIAS, M. A. F. S.; FREITAS, E. D. Influence of local circulations on wind, moisture, and precipitation close to Manaus city, Amazon Region, Brazil. **Journal of Geophysical Research: Atmospheres**, v. 119, n. 23, p. 13,233–13,249, 2014. ISSN 2169-8996. 2014JD021969. Disponível em: <http://dx.doi.org/10.1002/2014JD021969>. 42, 61

EBERT, E.; JANOWIAK, J. E.; KIDD, C. Comparison of near-real-time precipitation estimates from satellite observations and numerical models. **Bull. Amer. Meteor. Soc.**, v. 88, p. 47–64, 2007. 16

EBERT, E. E. Methods for verifying satellite precipitation estimates. In: LEVIZZANI, V.; BAUER, P.; TURK, F. J. (Ed.). **Measuring precipitation from space, EURAINSAT and the future**. Dordrecht, the Netherlands: Springer, 2007. p. 345–356. 1, 2, 8, 13, 29, 50, 67

FERRARO, R. R.; WENG, F.; GRODY, N. C.; ZHAO, L.; MENG, H.; KONGOLI, C.; PELLEGRINO, P.; QIU, S.; DEAN, C. Noaa operational hydrological products derived from the advanced microwave sounding unit. **IEEE Transactions on Geoscience and Remote Sensing**, v. 43, n. 5, p. 1036–1049, May 2005. ISSN 0196-2892. 8

GILLELAND, E.; AHIJEVYCH, D.; BROWN, B. G.; CASATI, B.; EBERT, E. E. Intercomparison of spatial forecast verification methods. **Weather and Forecasting**, v. 24, n. 5, p. 1416–1430, 2009. 16

GOAMAZON. **Observations and Modeling of the Green Ocean Amazon**. 2017. http://campaign.arm.gov/goamazon2014/. Accessed on 10 March 2017. 11

GONÇALVES, W. A.; MACHADO, L. A. T.; KIRSTETTER, P.-E. Influence of biomass aerosol on precipitation over the central Amazon: an observational study. **Atmospheric Chemistry and Physics**, v. 15, n. 12, p. 6789–6800, 2015. Disponível em: <http://www.atmos-chem-phys.net/15/6789/2015/>. 42, 55, 61

GORGUCCI, E.; CHANDRASEKAR, V.; BALDINI, L. Correction of x-band radar observation for propagation effects based on the self-consistency principle. **J. Atmos. Ocean. Technol.**, v. 23, p. 1668–1681, 2002. 22

GPM. **GPM Data Access**. 2016. http://pmm.nasa.gov/data-access/downloads/gpm. Accessed on 10 March 2016. 45

GUO, H.; CHEN, S.; BAO, A.; HU, J.; GEBREGIORGIS, A. S.; XUE, X.; ZHANG, X. Inter-comparison of high-resolution satellite precipitation products over central asia. **Remote Sensing**, v. 7, n. 6, p. 7181–7211, 2015. ISSN 2072-4292. Disponível em: <http://www.mdpi.com/2072-4292/7/6/7181>. 12

HERDIES, D. L.; SILVA, A. da; DIAS, M. A. S.; FERREIRA, R. N. Moisture budget of the bimodal pattern of the summer circulation over South America. **J. Geophys. Res.**, v. 107, n. 8075, 2002. 20

HITSCHFELD, W.; BORDAN, J. Errors inherent in the radar measurement of rainfall at attenuating wavelengths. **J. Meteorol.**, v. 11, p. 508–514, 1954. 23

HONG, Y.; HSU, K.-l.; MORADKHANI, H.; SOROOSHIAN, S. Uncertainty quantification of satellite precipitation estimation and monte carlo assessment of the error propagation into hydrologic response. **Water Resources Research**, v. 42, n. 8, p. n/a–n/a, 2006. ISSN 1944-7973. W08421. Disponível em: <http://dx.doi.org/10.1029/2005WR004398>. 2, 16

HONG, Y.; HSU, K.-L.; SOROOSHIAN, S.; GAO, X. Precipitation estimation from remotely sensed imagery using an artificial neural network cloud classification system. **Journal of Applied Meteorology**, v. 43, n. 12, p. 1834–1853, 2004. 10, 12, 13, 47

HOSSAIN, F.; ANAGNOSTOU, E. N. A two-dimensional satellite rainfall error model. **IEEE Trans. Geosci. Remote Sens.**, v. 44, p. 1511–1522, 2006. 16

HOU, A. Y.; KAKAR, R. K.; NEECK, S.; AZARBARZIN, A. A.; KUMMEROW, C. D.; KOJIMA, M.; OKI, R.; NAKAMURA, K.; IGUCHI, T. The Global Precipitatio Measuring Mission. **Bull. Amer. Meteor. Soc.**, v. 95, p. 701–722, 2014. 1, 7

HUFFMAN, G.; ADLER, R.; BOLVIN, D.; NELKIN, E. The trmm multi-satellite precipitation analysis (tmpa). In: **Proceedings...** Berlin, Germany: AMS, 2010. p. 3–22. 10, 47

HUFFMAN, G.; BOLVIN, D. **TRMM and Other Data Precipitation Data Set Documentation**. Neuss, Germany, 2015. Accessed on 1 April 2016. Disponível em: <http://pmm.nasa.gov/sites/default/files/document_files/3B42_3B43_doc_V7.pdf>. 47

HUFFMAN, G.; BOLVIN, D.; BRAITHWAITE, D.; HSU, K.; JOYCE, R.; XIE, P. **GPM Integrated Multi-Satellite Retrievals for GPM (IMERG) Algorithm Theoretical Basis Document (ATBD) Version 4.4**. Greenbelt, MD, 2014. 30 p. Accessed on 1 April 2016. Disponível em: <http://pmm.nasa.gov/sites/default/files/document_files/IMERG_ATBD_V4.4.pdf>. 10, 47, 86

HUFFMAN, G.; BOLVIN, D.; NELKIN, E. **Integrated Multi-satellitE Retrievals for GPM (IMERG) Technical Documentation**. Greenbelt, MD, 2015. Accessed on 1 April 2016. Disponível em: <http://pmm.nasa.gov/sites/default/files/document_files/IMERG_doc.pdf>. 47, 86

HUFFMAN, G. J.; BOLVIN, D. T.; NELKIN, E. J.; WOLFF, D. B.; ADLER, R. F.; GU, G.; HONG, Y.; BOWMAN, K. P.; STOCKER, E. F. The TRMM

multisatellite precipitation analysis (TMPA): Quasi-global, multiyear, combined-sensor precipitation estimates at fine scales. **Journal of Hydrometeorology**, v. 8, n. 1, p. 38–55, 2007. Disponível em: <http://dx.doi.org/10.1175/JHM560.1>. 10, 47

IGUCHI, T.; KOZU, T.; KWIATKOWSKI, J.; MENEGHINI, R.; AWAKA, J.; OKAMOTO, K. Uncertainties in the rain profiling algorithm for the TRMM precipitation radar. **Journal of the Meteorological Society of Japan. Ser. II**, v. 87A, p. 1–30, 2009. 15, 27

IGUCHI, T.; KOZU, T.; MENEGHINI, R.; AWAKA, J.; OKAMOTO, K. Rain-profiling algorithm for the TRMM precipitation radar. **Journal of Applied Meteorology**, v. 39, n. 12, p. 2038–2052, 2000. 7, 24, 27

IGUCHI, T.; OKI, R.; SMITH, E. A.; FURUHAMA, Y. Global precipitation measurement program and the development of dual-frequency precipitation radar. **J. Commun. Res. Lab.**, v. 49, p. 37–45, 2002. 7

IPWG. **International Precipitation Working Group**. 2017. http://www.isac.cnr.it/~ipwg/. Accessed on 10 March 2017. 1

JOYCE, R. J.; JANOWIAK, J. E.; ARKIN, P. A.; XIE, P. CMORPH: A method that produces global precipitation estimates from passive microwave and infrared data at high spatial and temporal resolution. **Journal of Hydrometeorology**, v. 5, n. 3, p. 487–503, 2004. 10, 47

JOYCE, R. J.; XIE, P. Kalman filter–based cmorph. **Journal of Hydrometeorology**, v. 12, n. 6, p. 1547–1563, 2011. 10, 12, 13, 47

KIDD, C. On rainfall retrieval using polarization-corrected temperatures. **Int. J. Remote Sens.**, v. 19, p. 981–996, 1998. 8

KIDD, C.; LEVIZZANI, V. Status of satellite precipitation retrievals. **Hydrol. Earth Syst. Sci.**, v. 15, p. 1109–1116, 2011. 2

KIDD, C.; MATSUI, T.; CHERN, J.; MOHR, K.; KUMMEROW, C.; RANDEL, D. Global precipitation estimates from cross-track passive microwave observations using a physically based retrieval scheme. **Journal of Hydrometeorology**, v. 17, n. 1, p. 383–400, 2016. Disponível em: <http://dx.doi.org/10.1175/JHM-D-15-0051.1>. 10, 45

KIRSTETTER, P.-E.; HONG, Y.; GOURLEY, J. J.; SCHWALLER, M.; PETERSEN, W.; ZHANG, J. Comparison of TRMM 2a25 products, version 6 and version 7, with NOAA/NSSL ground radar–based national mosaic QPE. **Journal of Hydrometeorology**, v. 14, n. 2, p. 661–669, 2013. Disponível em: <http://dx.doi.org/10.1175/JHM-D-12-030.1>. 15, 27, 49, 66

KOCH, S. E.; DESJARDINS, M.; KOCIN, P. J. An interactive barnes objective map analysis scheme for use with satellite and conventional data. **Journal of Climate and Applied Meteorology**, v. 22, n. 9, p. 1487–1503, 1983. 28

KUBOTA, T.; SHIGE, S.; HASHIZUME, H.; AONASHI, K.; TAKAHASHI, N.; SETO, S.; HIROSE, M.; TAKAYABU, Y.; NAKAGAWA, K.; IWANAMI, K.; USHIO, T.; KACHI, M.; OKAMOTO, K. Global precipitation map using satellite-borne microwave radiometers by the gsmap project: Production and validation. **IEEE Trans. Geosci. Remote Sens.**, v. 45, p. 2259–2275, 2007. 10

KUCERA, P.; EBERT, E.; TURK, F.; LEVIZZANI, V.; KIRSCHBAUM, D.; TAPIADOR, F.; LOEW, A.; BORSCHE, M. PRECIPITATION FROM SPACE – advancing, earth system science. **Bull. Am. Meteorol. Soc.**, v. 94, p. 365–375, 2013. 2

KUMMEROW, C. On the accuracy of the eddington approximation for radiative transfer in the microwave frequencies. **Journal of Geophysical Research: Atmospheres**, v. 98, n. D2, p. 2757–2765, 1993. ISSN 2156-2202. Disponível em: <http://dx.doi.org/10.1029/92JD02472>. 9

KUMMEROW, C.; BARNES, W.; KOZU, T.; SHIUE, J.; SIMPSON, J. The Tropical Rainfall Measuring Mission (TRMM) sensor package. **J. Atmos. Ocean. Technol.**, v. 15, p. 809–817, 1998. 1, 7, 24

KUMMEROW, C.; HONG, Y.; OLSON, W.; YANG, S.; ADLER, R.; MC-COLLUM, J.; FERRARO, R.; PETTY, G.; SHIN, D.-B.; WILHEIT, T. The evolution of the goddard profiling algorithm (GPROF) for rainfall estimation from passive microwave sensors. **J. Appl. Meteorol.**, v. 40, p. 1801–1820, 2001. 9, 21, 44

KUMMEROW, C.; OLSON, W.; GIGLIO, L. A simplified scheme for obtaining precipitation and vertical hydrometeor profiles from passive microwave sensors. **IEEE Trans. Geosci. Remote Sens.**, v. 34, p. 1213–1232, 1996. 9, 21, 44

KUMMEROW, C. D.; RANDEL, D. L.; KULIE, M.; WANG, N.-Y.; FERRARO, R.; MUNCHAK, S. J.; PETKOVIC, V. The evolution of the goddard profiling

algorithm to a fully parametric scheme. **Journal of Atmospheric and Oceanic Technology**, v. 32, n. 12, p. 2265–2280, 2015. Disponível em: <http://dx.doi.org/10.1175/JTECH-D-15-0039.1>. 10, 45

LEVIZZANI, V.; BAUER, P.; TURK, F. J. **Measuring precipitation from space – EURAINSAT and the future**. Dordrecht, the Netherlands: Springer, 2007. 748 p. ISBN 978-1-4020-5834-9. 1, 2, 10

LIAO, L.; MENEGHINI, R.; IGUCHI, T. Comparisons of rain rate and reflectivity factor derived from the TRMM precipitation radar and the WSR-88D over the melbourne, florida, site. **J. Atmos. Ocean. Technol.**, v. 18, p. 1959–1974, 2001. 2

LIEBMANN, B.; MARENGO, J. Interannual variability of the rainy season and rainfall in the Brazilian Amazon Basin. **J. Clim.**, v. 14, p. 4308–4318, 2001. xviii, 87, 88, 89

MACHADO, L.; DIAS, M. S.; MORALES, C.; FISCH, G.; VILA, D.; ALBRECHT, R.; GOODMAN, S.; CALHEIROS, A.; BISCARO, T.; KUMMEROW, C.; COHEN, J.; FITZJARRALD, D.; NASCIMENTO, E.; SAKAMOTO, M.; CUNNINGHAM, C.; CHABOUREAU, J.; PETERSEN, W.; ADAMS, D.; BALDINI, L.; ANGELIS, C.; SAPUCCI, L.; SALIO, P.; BARBOSA, H.; LANDULFO, E.; SOUZA, R.; BLAKESLEE, R.; BAILEY, J.; FREITAS, S.; LIMA, W.; TOKAY, A. The CHUVA Project – how does convection vary across Brazil? **Bull. Am. Meteorol. Soc.**, v. 95, p. 1–10, 2014. 2, 11

MACHADO, L.; LAURENT, H.; DESSAY, N.; MIRANDA, I. Seasonal and diurnal variability of convection over the Amazonia: A comparison of different vegetation types and large scale forcing. **Theor. Appl. Climatol.**, v. 78, p. 61–77, 2004. 42, 54, 56, 61, 87

MAGGIONI, V.; SAPIANO, M.; ADLER, R.; TIAN, Y.; HUFFMAN, G. An error model for uncertainty quantification in high-time-resolution precipitation products. **J. Hydrometeorol.**, v. 15, p. 1274–1292, 2014. 3, 16, 17, 85, 86, 88, 89, 90, 100

MARSHALL, J. S.; PALMER, W. M. K. The distribution of raindrops with size. **Journal of Meteorology**, v. 5, n. 4, p. 165–166, 1948. 22

MARTIN, S. T.; ARTAXO, P.; MACHADO, L. A. T.; MANZI, A. O.; SOUZA, R. A. F.; SCHUMACHER, C.; WANG, J.; ANDREAE, M. O.; BARBOSA, H. M. J.; FAN, J.; FISCH, G.; GOLDSTEIN, A. H.; GUENTHER, A.; JIMENEZ, J. L.; PÖSCHL, U.; DIAS, M. A. S.; SMITH, J. N.; WENDISCH, M. Introduction:

Observations and modeling of the Green Ocean Amazon (GoAmazon2014/5). **Atmospheric Chemistry and Physics**, v. 16, n. 8, p. 4785–4797, 2016. Disponível em: <http://www.atmos-chem-phys.net/16/4785/2016/>. 11, 42

MENEGHINI, R.; IGUCHI, T.; KOZU, T.; LIAO, L.; OKAMOTO, K.; JONES, J. A.; KWIATKOWSKI, J. Use of the surface reference technique for path attenuation estimates from the TRMM precipitation radar. **Journal of Applied Meteorology**, v. 39, n. 12, p. 2053–2070, 2000. 27

MICHAELIDES, S.; LEVIZZANI, V.; ANAGNOSTOU, E.; BAUER, P.; KASPARIS, T.; LANE, J. Precipitation: Measurement, remote sensing, climatology and modeling. **Atmos. Res.**, v. 94, p. 512–533, 2009. 2, 10

MOHR, K. I.; ZIPSER, E. J. Mesoscale convective systems defined by their 85-ghz ice scattering signature: Size and intensity comparison over tropical oceans and continents. **Monthly Weather Review**, v. 124, n. 11, p. 2417–2437, 1996. 37

MORALES, C.; BISCARO, T.; CARVALHO, I.; NEVES, J.; ANSELMO, E.; ALBRECHT, R.; MACHADO, L. Characterizing the different tropical rainfall regimes in Brazil: A contribution of CHUVA project. In: **Proceedings...** Breckenridge, CO, EUA: AMS, 2013. (8B.5). 2, 30

MUGNAI, A.; CASELLA, D.; CATTANI, E.; DIETRICH, S.; LAVIOLA, S.; LEVIZZANI, V.; PANEGROSSI, G.; PETRACCA, M.; SANÓ, P.; PAOLA, F. D.; BIRON, D.; LEONIBUS L. AD MELFI, D. R. P. D.; VOCINO, A.; ZAULI, F.; PAGLIARA, P.; PUCA, S.; RINOLLO, A.; MILANI, L.; PORCÚ, F.; GATTARI, F. Precipitation products from the hydrology SAF. **Nat. Hazards Earth Syst. Sci.**, v. 13, p. 1959–1981, 2013a. 1

MUGNAI, A.; SMITH, E.; TRIPOLI, G.; BIZZARRI, B.; CASELLA, D.; DIETRICH, S.; PAOLA F.AND PANEGROSSI, G. D.; SANò, P. CDRD and PNPR satellite passive microwave precipitation retrieval algorithms: EuroTRMM/EURAINSAT origins and H-SAF operations. **Nat. Hazards Earth Syst. Sci.**, v. 13, p. 887–912, 2013b. 2

NASA, P. **Global Precipitation Measurement (GPM) mission**. 2017. http://pmm.nasa.gov/GPM. Accessed on 10 March 2017. 7

NASCIMENTO, M. G. do; HERDIES, D. L.; SOUZA, D. O. de. The South American water balance: The influence of low-level jets. **Journal of Climate**, v. 29, n. 4, p. 1429–1449, 2016. Disponível em: <http://dx.doi.org/10.1175/JCLI-D-15-0065.1>. 20

NEGRI, A. J.; XU, L.; ADLER, R. F. A TRMM-calibrated infrared rainfall algorithm applied over Brazil. **Journal of Geophysical Research: Atmospheres**, v. 107, n. D20, p. LBA 15–1–LBA 15–15, 2002. ISSN 2156-2202. Disponível em: <http://dx.doi.org/10.1029/2000JD000265>. 61

OLIVEIRA, R.; MAGGIONI, V.; VILA, D.; MORALES, C. Characteristics and diurnal cycle of GPM rainfall estimates over the central Amazon region. **Remote Sensing**, v. 8, n. 7-544, 2016. ISSN 2072-4292. Disponível em: <http://www.mdpi.com/2072-4292/8/7/544>. 15, 66, 69, 85, 86, 87, 97, 98, 102, 103, 106, 129

OLIVEIRA, R. A.; BRAGA, R. C.; VILA, D. A.; MORALES, C. A. Evaluation of GPROF-SSMI/S rainfall estimates over land during the brazilian CHUVA-VALE campaign. **Atmospheric Research**, v. 163, p. 102 – 116, 2015. ISSN 0169-8095. 6th Workshop of the International Precipitation Working Group. Disponível em: <http://www.sciencedirect.com/science/article/pii/S0169809514004116>. 15, 43, 49, 66, 69, 103, 127

OLSON, W.; YANG, S.; STOUT, J.; GRECU, M. The goddard profiling algorithm (gprof): Description and current applications. In: LEVIZZANI, V.; BAUER, P.; TURK, F. J. (Ed.). **Measuring precipitation from space, EURAINSAT and the future**. Dordrecht, the Netherlands: Springer, 2007. p. 772. 9

OLSON, W. S.; KUMMEROW, C. D.; HONG, Y.; TAO, W.-K. Atmospheric latent heating distributions in the tropics derived from satellite passive microwave radiometer measurements. **J. Appl. Meteor.**, v. 38, p. 633–664, 1999. 9

PARK, S.; MAKI, M.; IWANAMI, K.; BRINGI, V. Correction of radar reflectivity and differential reflectivity for rain attenuation and estimation of rainfall at x-band wavelength. In: **Proceedings...** Melbourne, Australia: AMS, 2004. 22, 43

PETKOVIĆ, V.; KUMMEROW, C. D. Performance of the GPM passive microwave retrieval in the balkan flood event of 2014. **Journal of Hydrometeorology**, v. 16, n. 6, p. 2501–2518, 2015. 12, 15

PRAKASH, S.; MITRA, A. K.; AGHAKOUCHAK, A.; LIU, Z.; NOROUZI, H.; PAI, D. A preliminary assessment of GPM-based multi-satellite precipitation estimates over a monsoon dominated region. **Journal of Hydrology**, p. –, 2016. ISSN 0022-1694. Disponível em: <http://www.sciencedirect.com/science/article/pii/S0022169416000470>. 12, 15

PRAKASH, S.; MITRA, A. K.; PAI, D.; AGHAKOUCHAK, A. From TRMM to GPM: How well can heavy rainfall be detected from space? **Advances in Water Resources**, v. 88, p. 1 – 7, 2016. ISSN 0309-1708. 12

PUCA, S.; PORCU, F.; RINOLLO, A.; VULPIANI, G.; BAGUIS, P.; BALABANOVA, S.; CAMPIONE, E.; ERTÜRK, A.; GABELLANI, S.; IWANSKI, R.; JURASEK, M.; KANÁK, J.; KERÉNYI, J.; KOSHINCHANOV, G.; KOZINAROVA, G.; KRAHE, P.; LAPETA, B.; LÁBÓ, E.; MILANI, L.; OKON, L.; ÖZTOPAL, A.; PAGLIARA, P.; PIGNONE, F.; RACHIMOW, C.; REBORA, N.; ROULIN, E.; SÖNMEZ, I.; TONIAZZO, A.; BIRON, D.; CASELLA, D.; CATTANI, E.; DIETRICH, S.; PAOLA, F. D.; LAVIOLA, S.; LEVIZZANI, V.; MELFI, D.; MUGNAI, A.; PANEGROSSI, G.; PETRACCA, M.; SANÓ, P.; ZAULI, F.; ROSCI, P.; LEONIBUS, L. D.; AGOSTA, E.; GATTARI, F. The validation service of the hydrological SAF geostationary and polar satellite precipitation products. **Natural Hazards and Earth System Sciences**, v. 14, n. 4, p. 871–889, 2014. Disponível em: <http://www.nat-hazards-earth-syst-sci.net/14/871/2014/>. 2

RAIA, A.; CAVALCANTI, I. F. A. The life cycle of the South American monsoon system. **Journal of Climate**, v. 21, n. 23, p. 6227–6246, 2008. Disponível em: <http://dx.doi.org/10.1175/2008JCLI2249.1>. 42, 54

RASMUSSEN, K. L.; CHOI, S. L.; ZULUAGA, M. D.; HOUZE, R. A. TRMM precipitation bias in extreme storms in South America. **Geophysical Research Letters**, v. 40, n. 13, p. 3457–3461, 2013. ISSN 1944-8007. Disponível em: <http://dx.doi.org/10.1002/grl.50651>. 15

ROEBBER, P. J. Visualizing multiple measures of forecast quality. **Weather and Forecasting**, v. 24, n. 2, p. 601–608, 2009. Disponível em: <http://dx.doi.org/10.1175/2008WAF2222159.1>. 13, 50, 67

ROZANTE, J. R.; MOREIRA, D. S.; GONCALVES, L. G. G. de; VILA, D. A. Combining TRMM and surface observations of precipitation: Technique and validation over South America. **Weather and Forecasting**, v. 25, n. 3, p. 885–894, 2010. 28

SANTOS, E. B.; LUCIO, P. S.; SILVA, C. M. S. e. Precipitation regionalization of the Brazilian Amazon. **Atmospheric Science Letters**, v. 16, n. 3, p. 185–192, 2015. ISSN 1530-261X. Disponível em: <http://dx.doi.org/10.1002/asl2.535>. 88

SAPIANO, M.; ARKIN, P. An intercomparison and validation of high-resolution satellite precipitation estimates with 3-hourly gauge data. **J. Hydrometeorol.**, v. 10, p. 149–166, 2009. 1, 12, 13, 29, 50

SATYAMURTY, P.; CASTRO, A. A. de; TOTA, J.; GULARTE, L. E. S.; MANZI, A. O. Rainfall trends in the Brazilian Amazon basin in the past eight decades. **Theor. Appl. Climatol.**, v. 99, p. 139–148, 2010. 87

SATYAMURTY, P.; JR, S. B. D. S.; TEIXEIRA, M. D. S.; SILVA, L. E. M. G. D. Regional circulation differences between a rainy episode and a nonrainy episode in eastern são paulo state in march 2006. **Revista Brasileira de Meteorologia**, scielo, v. 23, p. 404 – 416, 12 2008. ISSN 0102-7786. 20

SCHNEEBELI, M.; SAKURAGI, J.; BISCARO, T.; ANGELIS, C. F.; COSTA, I. Carvalho da; MORALES, C.; BALDINI, L.; MACHADO, L. A. T. Polarimetric x-band weather radar measurements in the tropics: radome and rain attenuation correction. **Atmospheric Measurement Techniques**, v. 5, n. 9, p. 2183–2199, 2012. Disponível em: <http://www.atmos-meas-tech.net/5/2183/2012/>. 22

SCHUMACHER, C.; JR., R. A. H. Comparison of radar data from the TRMM satellite and kwajalein oceanic validation site. **Journal of Applied Meteorology**, v. 39, n. 12, p. 2151–2164, 2000. 44

_____. The TRMM precipitation radar's view of shallow, isolated rain. **Journal of Applied Meteorology**, v. 42, n. 10, p. 1519–1524, 2003. 37

SETO, S.; IGUCHI, T.; UTSUMI, N.; KIGUCHI, M.; OKI, T. Evaluation of extreme rain estimates in the TRMM/PR standard product version 7 using high-temporal-resolution rain gauge datasets over Japan. **SOLA**, v. 9, p. 98–101, 2013. 15

SILBERSTEIN, D. S.; WOLFF, D. B.; MARKS, D. A.; ATLAS, D.; PIPPITT, J. L. Ground clutter as a monitor of radar stability at kwajalein, RMI. **Journal of Atmospheric and Oceanic Technology**, v. 25, n. 11, p. 2037–2045, 2008. 44

SOUZA, D. O. de; ALVALÁ, R. C. dos S. Observational evidence of the urban heat island of Manaus city, Brazil. **Meteorological Applications**, John Wiley & Sons, Ltd, v. 21, n. 2, p. 186–193, 2014. ISSN 1469-8080. Disponível em: <http://dx.doi.org/10.1002/met.1340>. 42

SPENCER, R. W. A satellite passive 37-ghz scattering-based method for measuring oceanic rain rates. **J. Appl. Meteorol.**, v. 25, p. 754–766, 1986. 8

SPENCER, R. W.; GOODMAN, H. M.; HOOD, R. E. Precipitation retrieval over land and ocean with the SSM/I: Identification and characteristics of the scattering signal. **J. Atmos. Ocean. Technol.**, v. 6, p. 254–273, 1989. 8

TANAKA, L. M. d. S.; SATYAMURTY, P.; MACHADO, L. A. T. Diurnal variation of precipitation in central Amazon Basin. **International Journal of Climatology**, John Wiley & Sons, Ltd, v. 34, n. 13, p. 3574–3584, 2014. ISSN 1097-0088. Disponível em: <http://dx.doi.org/10.1002/joc.3929>. 42, 56, 61

TANG, G.; MA, Y.; LONG, D.; ZHONG, L.; HONG, Y. Evaluation of GPM day-1 IMERG and TMPA version-7 legacy products over Mainland China at multiple spatiotemporal scales. **Journal of Hydrology**, v. 533, p. 152 – 167, 2016. ISSN 0022-1694. Disponível em: <http://www.sciencedirect.com/science/article/pii/S0022169415009476>. 12, 15, 57

TANG, L.; TIAN, Y.; YAN, F.; HABIB, E. An improved procedure for the validation of satellite-based precipitation estimates. **Atmospheric Research**, v. 163, p. 61 – 73, 2015. ISSN 0169-8095. 6th Workshop of the International Precipitation Working Group. 2, 12, 16, 17

TAPIADOR, F.; TURK, F.; PETERSEN, W.; HOU, A.; GARCíA-ORTEGA, E.; MACHADO, L.; ANGELIS, C.; SALIO, P.; KIDD, C.; HUFFMAN, J.; CASTRO, M. de. Global precipitation measurement, methods, datasets and applications. **Atmos. Res.**, v. 104, p. 70–97, 2011. 2

TAYLOR, K. E. Summarizing multiple aspects of model performance in a single diagram. **Journal of Geophysical Research: Atmospheres**, v. 106, n. D7, p. 7183–7192, 2001. ISSN 2156-2202. Disponível em: <http://dx.doi.org/10.1029/2000JD900719>. 13, 28, 50, 67

TESTUD, J.; BOUAR, E. L.; OBLIGIS, E.; ALI-MEHENNI, M. The rain profiling algorithm applied to polarimetric weather radar. **Journal of Atmospheric and Oceanic Technology**, v. 17, n. 3, p. 332–356, 2000. 23

TIAN, Y.; HUFFMAN, G. J.; ADLER, R. F.; TANG, L.; SAPIANO, M.; MAGGIONI, V.; WU, H. Modeling errors in daily precipitation measurements: Additive or multiplicative? **Geophysical Research Letters**, v. 40, n. 10, p. 2060–2065, 2013. ISSN 1944-8007. Disponível em: <http://dx.doi.org/10.1002/grl.50320>. 2, 3, 16

TIAN, Y.; PETERS-LIDARD, C.; EYLANDER, J.; JOYCE, R.; HUFFMAN, G.; ADLER, R.; HSU, K.; TURK, F.; GARCIA, M.; J., Z. Component analysis of errors in satellite-based precipitation estimates. **J. Geophys. Res.**, v. 114, p. D24101, 2009. 16, 17

TOTA, J.; FISCH, G.; FUENTES, J.; OLIVEIRA, P.; GARSTANG, M.; HEITZ, R.; SIGLER, J. Análise da variabilidade diária da precipitação em área de pastagem para a época chuvosa de 1999—projeto TRMM/LBA. **Acta Amazôn.**, v. 30, p. 629–639, 2000. 56

TURK F.J., A. P. E. E. S. M. Evaluating high-resolution precipitation products. **Bull. Amer. Meteor. Soc.**, v. 89, p. 1911–1916, 2008. 1

VERA, C.; HIGGINS, W.; AMADOR, J.; AMBRIZZI, T.; GARREAUD, R.; GOCHIS, D.; GUTZLER, D.; LETTENMAIER, D.; MARENGO, J.; MECHOSO, C. R.; NOGUES-PAEGLE, J.; DIAS, P. L. S.; ZHANG, C. Toward a unified view of the American monsoon systems. **Journal of Climate**, v. 19, n. 20, p. 4977–5000, 2006. 42

VILA, D.; FERRARO, R.; SEMUNEGUS, H. Improved global rainfall retrieval using the special sensor microwave imager (SSM/I). **Journal of Applied Meteorology and Climatology**, v. 49, n. 5, p. 1032–1043, 2010. 9

VILA, D.; GONCALVES, L. de; TOLL, D.; ROZANTE, J. Statistical evaluation of combined daily gauge observations and rainfall satellite estimates over continental South America. **J. Hydrometeorol.**, v. 10, p. 533–543, 2009. 2

VILA, D.; HERNANDEZ, C.; FERRARO, R.; SEMUNEGUS, H. The performance of hydrological monthly products using SSM/I–SSMI/S sensors. **J. Hydrometeorol.**, v. 14, p. 266–274, 2013. 9, 21, 44

VILLAR, J. C. E.; RONCHAIL, J.; GUYOT, J. L.; COCHONNEAU, G.; NAZIANO, F.; LAVADO, W.; OLIVEIRA, E. D.; POMBOSA, R.; VAUCHEL, P. Spatio-temporal rainfall variability in the Amazon basin countries (Brazil, Peru, Bolivia, Colombia, and Ecuador). **International Journal of Climatology**, John Wiley & Sons, Ltd., v. 29, n. 11, p. 1574–1594, 2009. ISSN 1097-0088. Disponível em: <http://dx.doi.org/10.1002/joc.1791>. 88

VILLARINI, G.; KRAJEWSKI, W. F.; CIACH, G. J.; ZIMMERMAN, D. L. Product-error-driven generator of probable rainfall conditioned on wsr-88d precipitation estimates. **Water Resources Research**, v. 45, n. 1, 2009. ISSN

1944-7973. W01404. Disponível em: <http://dx.doi.org/10.1029/2008WR006946>. 16

WILKS, D. **Statistical methods in the atmospheric sciences. An introduction**. San Diego, CA: Academic Press, 2006. 627 p. 2nd edn. ISBN 9780127519661. 13, 29, 50, 67

WOLFF, D. B.; FISHER, B. L. Assessing the relative performance of microwave-based satellite rain-rate retrievals using TRMM ground validation data. **Journal of Applied Meteorology and Climatology**, v. 48, n. 6, p. 1069–1099, 2009. Disponível em: <http://dx.doi.org/10.1175/2008JAMC2127.1>. 15, 49, 66

WOLFF, J. K.; HARROLD, M.; FOWLER, T.; GOTWAY, J. H.; NANCE, L.; BROWN, B. G. Beyond the basics: Evaluating model-based precipitation forecasts using traditional, spatial, and object-based methods. **Weather and Forecasting**, v. 29, n. 6, p. 1451–1472, 2014. 68

YUTER, S. E.; HOUZEJR., R. A. Three-dimensional kinematic and microphysical evolution of florida cumulonimbus. part ii: Frequency distributions of vertical velocity, reflectivity, and differential reflectivity. **Mon. Wea. Rev.**, v. 123, p. 1941–1963, 1995. 80

ZHOU, J.; LAU, K.-M. Does a monsoon climate exist over South America? **Journal of Climate**, v. 11, n. 5, p. 1020–1040, 1998. 42

APPENDIX A - GPROF2014 UPDATES AND IMPROVEMENTS

This appendix shows the over Land x River rainfall representation improvement of GPROF2014 algorithm from the updated version (from V1.4 to 2.0) over the Brazilian Amazon.

A.1 GPROF2014 algorithm updates and improvements over the Brazilian Amazon

Figure A.1 - An overview of the GPROF2014 V2.0 (GPM.GMI V04A) rainfall estimates over the Brazilian Amazon

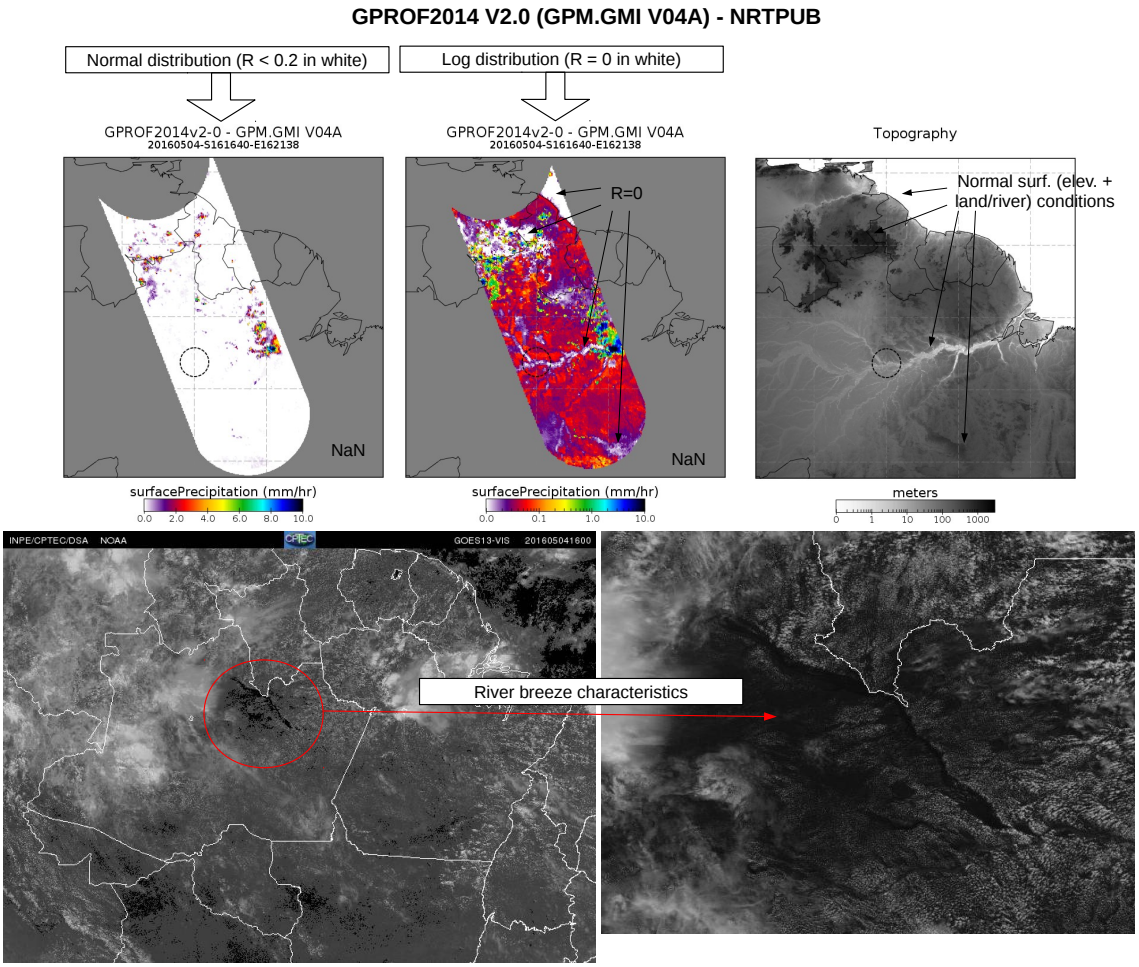

The GPROF2014 V2.0 for GPM.GMI Near Real Time (NRT) seems to be corrected in relation to the non-realistic rainfall fields along the Amazonas/Solimoes/Rio Negro river. However the occurrence of light rain (less than 0.2) is high over land, that may be related to the use of DPR Ku instead of DPR Ka+ku. According to the GPM Team, the DPR Ku product is more reliable than the DPR Ka+Ku combination. "...Ku product was validating significantly better than the other GPM products..."

SOURCE: Author's production.

Figure A.2 - An example of the GPROF2014(V1-4) GMI (V03B) (left) vs. GPROF2014(V2-0) GMI (V04A) (right) over the Brazilian Amazon Grid box of 10deg x 10deg centered in Manaus AM.

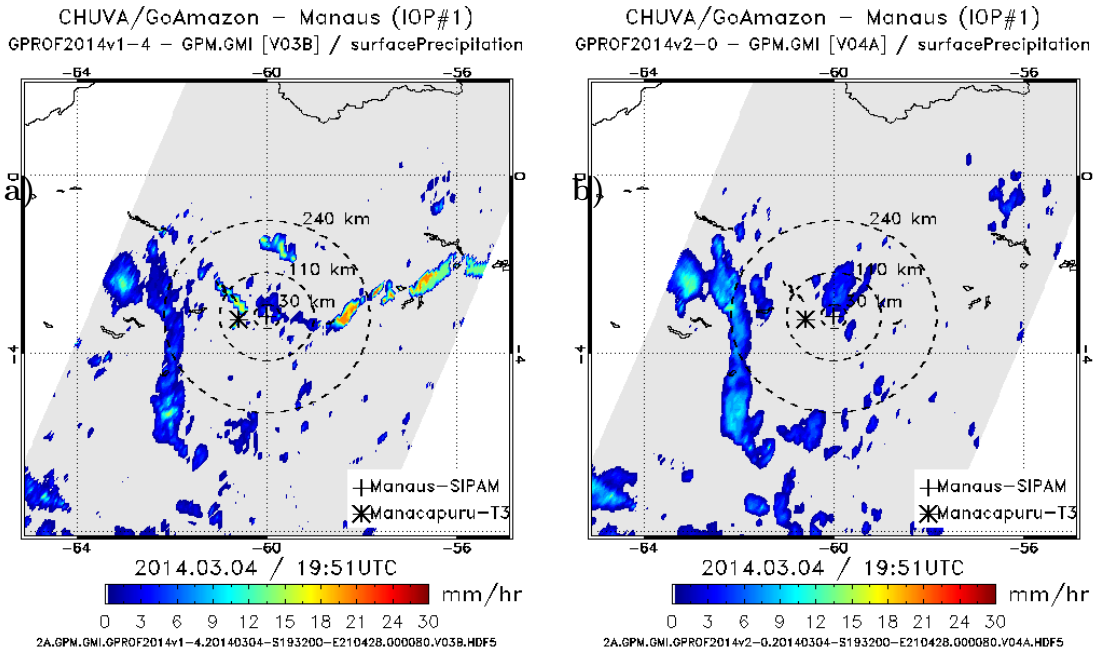

SOURCE: Author's production.

Through Figure A.3, the occurrence of light precipitation (here under the 0.1 mm h^{-1} threshold) is higher in the new version (V2-0/V04D) than in the old version (V1-4/V03B) of GPROF2014, over both surface types. However, if we look at rainfall above the 0.2 mm h^{-1} threshold (Fig. A.4), the precipitation field now looks more realistic. But of course, now the rainfall uncertainties are not well evident along the river and over the continent, and the uncertainty investigation via error modeling can clarify and explain the results related to meteorological conditions. For example: Are the satellite errors more evident during the rainfall peak? Which period? Figure A.5 shows another evidence of the improvement of GPROF2014 for GPM.GMI over the Amazon (Rio Negro, Solimões and Amazonas rivers).

Figure A.3 - a) Unconditional PDFv and PDFc comparisons of the GPROF2014(V1-4) GMI (V03B) vs. GPROF2014(V2-0) GMI (V04A), over the Brazilian Amazon Grid box of 10deg x 10deg centered in Manaus AM.

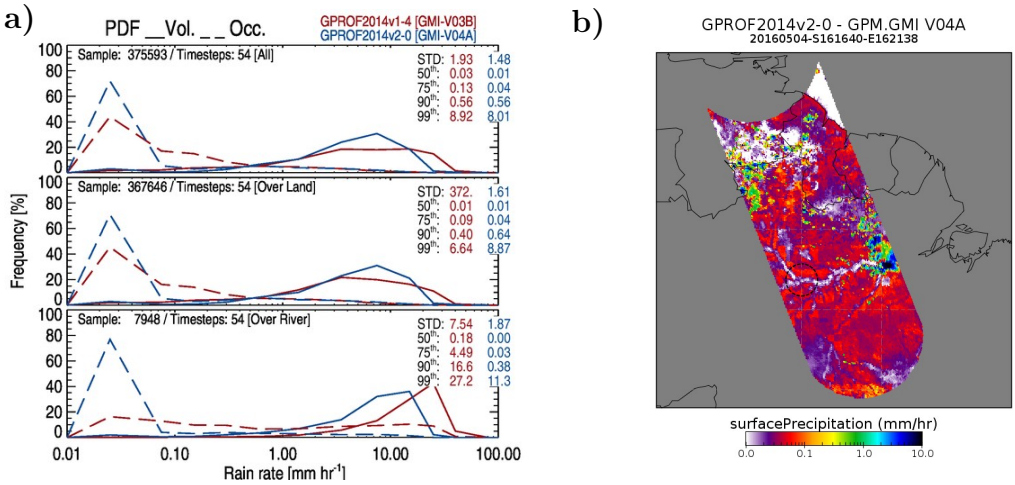

SOURCE: Author's production.

Figure A.4 - As in Fig. A.3, but for the $\geq$0.2 mm h $^{-1}$ threshold.

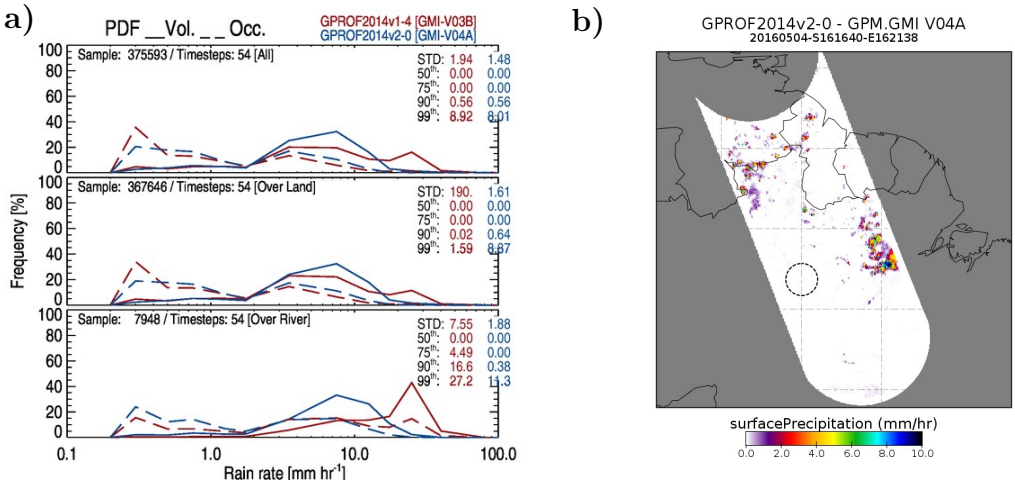

SOURCE: Author's production.

Figure A.5 - An overview of the GPROF2014 V2.0 (GPM.GMI V04A) rainfall estimates over the Brazilian Amazon

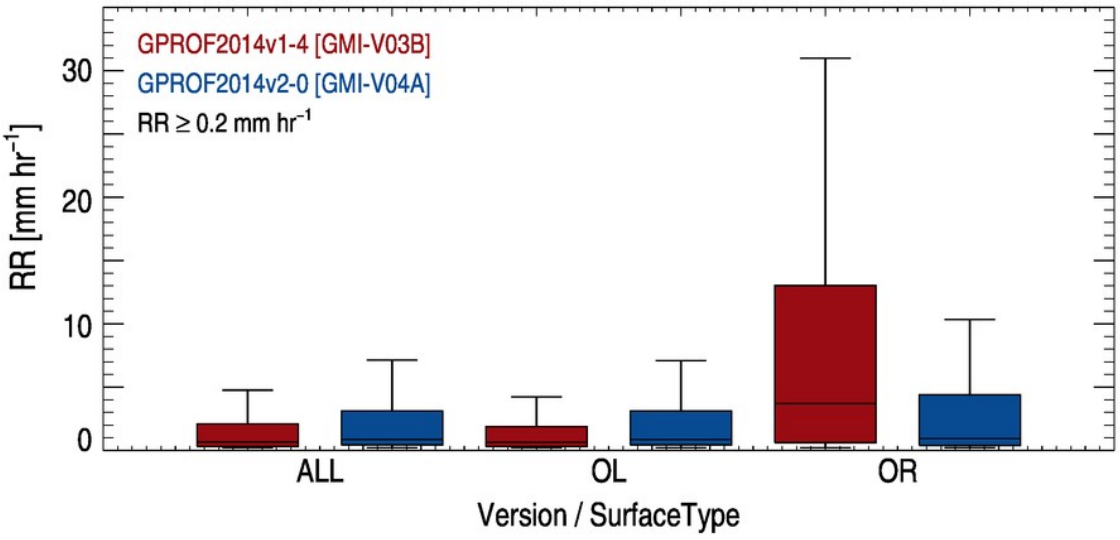

SOURCE: Author's production.

ANNEX A - MANUSCRIPT PUBLISHED IN *ATMOSPHERIC RESEARCH* MAGAZINE

Figure A.1 - First page of the manuscript published in *Atmospheric Research* Journal, Special Issue *6th Workshop of the International Precipitation Working Group*.

Atmospheric Research 163 (2015) 102–116

Contents lists available at ScienceDirect

Atmospheric Research

journal homepage: www.elsevier.com/locate/atmos

Evaluation of GPROF-SSMI/S rainfall estimates over land during the Brazilian CHUVA-VALE campaign

Rômulo A.J. Oliveira [a,*], Ramon C. Braga [a], Daniel A. Vila [a], Carlos A. Morales [b]

[a] Centro de Previsão de Tempo e Estudos Climáticos (CPTEC), Instituto Nacional de Pesquisas Espaciais (INPE), São Paulo, Brazil
[b] Departamento de Ciências Atmosféricas (DCA). Instituto de Astronomia, Geofísica e Ciências Atmosféricas (IAG), Universidade de São Paulo (USP), São Paulo, Brazil

ARTICLE INFO

Article history:
Received 1 May 2014
Received in revised form 13 November 2014
Accepted 14 November 2014
Available online 21 November 2014

Keywords:
Satellite rainfall estimation
Validation
GPROF
SSMI/S
TRMM
CHUVA Project

ABSTRACT

One of the major goals of the CHUVA project (Cloud processes of tHe main precipitation systems in Brazil: A contribUtion to cloud resolVing modeling and to the GPM [GlobAl Precipitation Measurement]) is to collect information about the cloud processes of the main precipitating systems over Brazil in order to evaluate and improve the quality of satellite-based precipitation estimates. Thus, this paper evaluates the performance of the Goddard Profiling Algorithm (GPROF) version 2004 for the Special Sensor Microwave Imager/Sounder (SSMIS) sensor, carried onboard the Defense Meteorological Satellite Program (DMSP) F16, F17 and F18 satellites, for instantaneous rain rates over land by comparing with other remote sensing based estimates such as X-band dual polarization rainfall retrievals from the CHUVA Project (named here X-band CHUVA radar) and TRMM (Tropical Rainfall Measurement Mission) Precipitation Radar – version 7 (PR-V7) precipitation estimates (named here the 2A25_V7 product) for the CHUVA-VALE campaign. The analyses were performed on an area within a radius of 60 km from the X-band CHUVA radar, located at São José dos Campos, SP – Brazil (centered at 23.2°S and 45.95°W) and another delimited by 41°W–51°W and 18°S–28°S (10° x 10° box). GPROF showed an overestimate of light/moderate rain rate intensities, while underestimating the rainfall rates above 10 mm h^{-1}, considering the X-band CHUVA radar as reference. The same behavior was observed when compared with the 2A25_V7 database. Through a PDF analysis, GPROF was found to overestimate the frequencies of moderate rain rates (between 2 and 10 mm h^{-1}, above 15%), and underestimate the frequencies of light and high rain rates (<2 mm h^{-1} and >10 mm h^{-1}, respectively) when compared to both the X-band CHUVA radar and 2A25_V7 reference databases. The results for the studied region suggest that GPROF has a relatively good agreement (spatial distribution and accumulated rainfall), especially for convective rain cases, due the significant presence of ice scattering. However, the intensity of light/moderate rains is overestimated.

1. Introduction

The forecast and quantification of rain with the highest possible accuracy, especially for severe weather situations, over various temporal and spatial scales, are extremely important to society because they are directly linked to the economy through agriculture, natural resources, transportation, and the prediction and detection of natural disaster occurrences. Alternatively, satellite rainfall estimation (microwave, infrared, hybrid, etc.) has been widely used in Brazil for various purposes, e.g. for monitoring natural disasters, hydrologic purposes and climatic applications. However, such algorithms require validation studies using observational rainfall data, preferably at high spatial-temporal resolution.

In this context, the international collaboration called the Program to Evaluate High Resolution Precipitation Products (PEHRPP), established within the International Precipitation Working Group (IPWG; see http://www.isac.cnr.it/~ipwg/), was a collaborative effort to evaluate, intercompare and validate the several high-resolution precipitation algorithms currently available and operational (e.g., Ebert et al., 2007; Turk et al., 2008; Sapiano and Arkin, 2009; Di Paola et al., 2012; Casella et al., 2012; Mugnai et al., 2013a). Most studies have focused on the evaluation of the performance of certain products of satellite precipitation estimates, in general based on infrared (IR) or microwave observations and their combinations (Mugnai et al., 2013b). Typically the comparisons are made using rain gauges (e.g., Vila et al., 2009; Puca et al., 2014). However, studies using other data sources have been widely used, e.g., active microwaves (Aonashi et al. 2009), dual polarization weather radars (e.g., Liao et al., 2001; Chandrasekar et al., 2008; Cimini et al., 2013), disdrometers (Morales et al., 2013), among others. Extensive information on actual, ongoing and future activities/plans regarding precipitation measurement (observational, modeling and from satellites) and its performance and applications are given by Michaelides

* Corresponding author at: National Institute for Space Research (INPE), Center for Weather Forecast and Climate Studies (CPTEC), Rodovia Presidente Dutra, km 40, Cachoeira Paulista/SP – 12630-000, Brazil. Tel.: +55 12 31869523; fax: +55 12 31869291.
E-mail address: romulo.augusto@cptec.inpe.br (R.A.J. Oliveira).

http://dx.doi.org/10.1016/j.atmosres.2014.11.010
0169-8095/

SOURCE: Oliveira et al. (2015).

ANNEX B - MANUSCRIPT PUBLISHED IN *REMOTE SENSING* MAGAZINE

Figure B.1 - First page of the manuscript published in *Remote Sensing* Journal, Special Issue *Uncertainties in Remote Sensing*.

Article

Characteristics and Diurnal Cycle of GPM Rainfall Estimates over the Central Amazon Region

Rômulo Oliveira [1,2,*], Viviana Maggioni [2], Daniel Vila [1] and Carlos Morales [3]

[1] Centro de Previsão de Tempo e Estudos Climáticos (CPTEC), Instituto Nacional de Pesquisas Espaciais (INPE), São Jos é dos Campos, SP 12227-010, Brazil; daniel.vila@cptec.inpe.br
[2] Department of Civil, Environmental, and Infrastructure Engineering, George Mason University (GMU), Fairfax, VA 22030, USA; vmaggion@gmu.edu
[3] Departamento de Ciências Atmosféricas (DCA), Instituto de Astronomia, Geofísica e Ciências Atmosféricas (IAG), Universidade de São Paulo (USP), São Paulo, SP 05508-900, Brazil; carlos.morales@iag.usp.br
* Correspondence: romulo.augusto@cptec.inpe.br; Tel.: +55-12-3208-6821

Academic Editors: Yudong Tian, Ken Harrison, Alfredo R. Huete and Prasad S. Thenkabail
Received: 1 April 2016; Accepted: 7 June 2016; Published: 25 June 2016

Abstract: Studies that investigate and evaluate the quality, limitations and uncertainties of satellite rainfall estimates are fundamental to assure the correct and successful use of these products in applications, such as climate studies, hydrological modeling and natural hazard monitoring. Over regions of the globe that lack in situ observations, such studies are only possible through intensive field measurement campaigns, which provide a range of high quality ground measurements, e.g., CHUVA (Cloud processes of tHe main precipitation systems in Brazil: A contribUtion to cloud resolVing modeling and to the GlobAl Precipitation Measurement) and GoAmazon (Observations and Modeling of the Green Ocean Amazon) over the Brazilian Amazon during 2014/2015. This study aims to assess the characteristics of Global Precipitation Measurement (GPM) satellite-based precipitation estimates in representing the diurnal cycle over the Brazilian Amazon. The Integrated Multi-satellitE Retrievals for Global Precipitation Measurement (IMERG) and the Goddard Profiling Algorithm—Version 2014 (GPROF2014) algorithms are evaluated against ground-based radar observations. Specifically, the S-band weather radar from the Amazon Protection National System (SIPAM), is first validated against the X-band CHUVA radar and then used as a reference to evaluate GPM precipitation. Results showed satisfactory agreement between S-band SIPAM radar and both IMERG and GPROF2014 algorithms. However, during the wet season, IMERG, which uses the GPROF2014 rainfall retrieval from the GPM Microwave Imager (GMI) sensor, significantly overestimates the frequency of heavy rainfall volumes around 00:00–04:00 UTC and 15:00–18:00 UTC. This overestimation is particularly evident over the Negro, Solimões and Amazon rivers due to the poorly-calibrated algorithm over water surfaces. On the other hand, during the dry season, the IMERG product underestimates mean precipitation in comparison to the S-band SIPAM radar, mainly due to the fact that isolated convective rain cells in the afternoon are not detected by the satellite precipitation algorithm.

Keywords: satellite rainfall estimates; radar rainfall estimates; GPM; IMERG; GPROF; uncertainty quantification; GoAmazon

1. Introduction

Satellite rainfall estimates have been widely used for various purposes (e.g., real-time weather monitoring and forecasting, hydrological modeling and climate studies, among others). The quality of satellite rainfall products has improved significantly in recent decades, especially with the advent

SOURCE: Oliveira et al. (2016).

PUBLICAÇÕES TÉCNICO-CIENTÍFICAS EDITADAS PELO INPE

Teses e Dissertações (TDI)

Teses e Dissertações apresentadas nos Cursos de Pós-Graduação do INPE.

Notas Técnico-Científicas (NTC)

Incluem resultados preliminares de pesquisa, descrição de equipamentos, descrição e ou documentação de programas de computador, descrição de sistemas e experimentos, apresentação de testes, dados, atlas, e documentação de projetos de engenharia.

Propostas e Relatórios de Projetos (PRP)

São propostas de projetos técnico-científicos e relatórios de acompanhamento de projetos, atividades e convênios.

Publicações Seriadas

São os seriados técnico-científicos: boletins, periódicos, anuários e anais de eventos (simpósios e congressos). Constam destas publicações o Internacional Standard Serial Number (ISSN), que é um código único e definitivo para identificação de títulos de seriados.

Pré-publicações (PRE)

Todos os artigos publicados em periódicos, anais e como capítulos de livros.

Manuais Técnicos (MAN)

São publicações de caráter técnico que incluem normas, procedimentos, instruções e orientações.

Relatórios de Pesquisa (RPQ)

Reportam resultados ou progressos de pesquisas tanto de natureza técnica quanto científica, cujo nível seja compatível com o de uma publicação em periódico nacional ou internacional.

Publicações Didáticas (PUD)

Incluem apostilas, notas de aula e manuais didáticos.

Programas de Computador (PDC)

São a seqüência de instruções ou códigos, expressos em uma linguagem de programação compilada ou interpretada, a ser executada por um computador para alcançar um determinado objetivo. Aceitam-se tanto programas fonte quanto os executáveis.